

Department of Physics
University of Fribourg (Switzerland)

Investigation of surface nanostructures with grazing angle x-ray fluorescence techniques

THESIS

presented to the Faculty of Science of the University of Fribourg (Switzerland)
in consideration for the award of the academic grade of *Doctor rerum naturalium*

by

Stanisław H. Nowak

from
Kielce, Poland

Accepted by the Faculty of Science of the University of Fribourg (Switzerland) upon the recommendation of:

Prof. Dr. Philipp Aebi, University of Fribourg (President of the jury)
Prof. Dr. Jean-Claude Dousse, University of Fribourg (Thesis Supervisor)
Dr. hab. Joanna Hoszowska, University of Fribourg (Expert)
Prof. Dr. Marek Pajek, Jan Kochanowski University (External expert)

Fribourg, 6th December 2012.

Thesis supervisor

A handwritten signature in blue ink, appearing to read 'JC Dousse', with a long horizontal flourish extending to the right.

Prof. Dr. Jean-Claude Dousse

Dean

A handwritten signature in blue ink, appearing to read 'R Ingold', with a stylized, looped structure.

Prof. Dr. Rolf Ingold

*To Piotr Kosztolowicz, to
whom I owe my fascination
with science*

Contents

Contents	5
Summary	9
Résumé	11
I Introduction	13
I-1 Total reflection of x-rays	15
I-2 X-ray fluorescence techniques related to the total reflection of x-rays	16
I-2.1 Total reflection x-ray fluorescence	16
I-2.2 Grazing incidence x-ray fluorescence	17
I-2.3 Grazing emission x-ray fluorescence	18
I-3 GIXRF and GEXRF application for nanostructures characterisation	19
I-3.1 Angular profiles of surfaces containing individual particles	20
I-3.2 Angular profiles of dense particles' distributions	20
I-3.2.1 Nevot-Croce model	21
I-3.2.2 Stack of layers of various density model	21
I-3.2.3 Linear combination of angular profiles	22
I-3.2.4 Limitations of the models	22
I-3.3 Periodic structures	23
I-3.3.1 Grating-like substrates	23
I-3.3.2 Multiple reflections in periodic structures	23
II Experimental	25
II.A GEXRF measurements	27
II.A-1 Von Hamos spectrometer	27
II.A-1.1 Spectrometer chamber	28
II.A-1.2 Construction details and motorisation	29
II.A-1.3 Bragg crystals	31
II.A-1.4 Detector	31

CONTENTS

II.A-2	Target holders	32
II.A-2.1	Carrousel target holder	32
II.A-2.2	Piezo target holder	33
II.A-2.2.1	Design	33
II.A-2.2.2	Spatial constraints	34
II.A-2.2.3	Target mounting	35
II.A-3	ESRF measurements	35
II.A-3.1	ID21 beamline overview	36
II.A-3.2	MI-975 experiment	37
II.A-3.3	MI-1108 experiment	38
II.A-4	SLS measurements	38
II.A-4.1	SuperXAS beamline overview	38
II.A-4.2	Experiment	40
II.B	GIXRF measurements	43
II.B-1	Beamlines	43
II.B-1.1	Plane grating monochromator beamline	43
II.B-1.2	Four-crystal monochromator beamline	44
II.B-2	GIXRF setup	45
II.B-2.1	Ultra-high vacuum x-ray spectrometry chamber	45
II.B-2.2	6-axis manipulator ultra-high vacuum chamber	46
II.B-3	Reference-free analysis	47
II.C	Samples	49
II.C-1	Evenly distributed structures	49
II.C-1.1	Fe, Cr and MgO thermal evaporated structures	49
II.C-1.2	NaCl nanostructures	51
II.C-2	Periodic structures	52
II.C-2.1	Cr pads	52
II.C-2.2	Cr stripes	52
II.C-2.3	Cr trapezoidal prisms	53
II.C-2.4	Disk patterns made of one and two superposed 3d elements	53
II.C-2.5	Samples with plane symmetries	54
III	Data analysis and data processing	59
III.A	CCD events analysis	61
III.A-1	Currently used algorithm	61
III.A-2	New algorithm	63
III.A-3	Energy window	65
III.A-4	Background consideration	66
III.A-5	Comparison between the two algorithms	67

III.B	CCD image correction in the von Hamos geometry	71
III.B-1	Image properties in the von Hamos geometry	71
III.B-2	GEXRF related properties	72
III.B-3	Applying corrections to a CCD image	73
III.B-4	Calculations of images	73
III.B-5	Angular resolution	75
III.B-5.1	Darwin width	75
III.B-5.2	Size of the fluorescence source	76
III.B-5.2.1	Horizontal dimension	76
III.B-5.2.2	Vertical dimension	76
III.B-5.2.3	Physical source dimensions	76
III.B-5.3	CCD pixel dimensions	77
III.C	Geometrical optics approach to GEXRF and GIXRF	79
III.C-1	Standing waves	79
III.C-2	Intermediate morphology	80
III.C-3	Ray tracing	80
III.C-3.1	Roughness model	81
III.C-3.2	Reverse ray tracing algorithm	82
III.C-3.3	Optical paths coherence	85
III.C-3.4	Multi structures	85
III.D	Effective flux of incidence radiation	87
III.D-1	Effective flux calculation	87
III.D-2	GEXRF and GIXRF comparison	88
III.D-3	Buried structures	89
IV	Results and Discussion	91
IV.A	Periodic structures	93
IV.A-1	Cr pads	93
IV.A-1.1	XSW simulation	94
IV.A-1.2	GO simulations	95
IV.A-2	Cr stripes	95
IV.A-2.1	XSW field calculations	97
IV.A-2.2	GO calculations	98
IV.A-2.3	Intensity modulation	98
IV.A-2.4	Effective flux correction	100
IV.A-3	Cr trapezoidal prisms	101
IV.A-3.1	GO ray tracing simulations	102
IV.A-4	Samples with plane symmetries	104
IV.A-4.1	Cr disc samples	104
IV.A-4.2	Co/Ni discs sample	104
IV.B	Evenly distributed structures	107
IV.B-1	NaCl nanostructures	107
IV.B-2	Fe and Cr layers of various roughnesses	108
IV.B-2.1	Application of sample morphology models	109
IV.B-3	Samples with Co and Ni discs	112

CONTENTS

IV.C	Remarks on experimental difficulties	115
IV.C-1	Exit angle calibration	115
IV.C-1.1	Calibration from the spectrometer corrections	115
IV.C-1.2	Calibration to the support material	116
IV.C-1.3	Calibration to the reference structure	116
IV.C-1.4	Calibration with the spectral background	116
IV.C-2	Background extraction	117
IV.C-3	Synchrotron radiation beam instabilities	118
IV.C-3.1	Beam spot position	119
V	Concluding remarks	121
V-1	Grazing angle x-ray fluorescence from surface nanostructures	123
V-2	GO ray tracing	123
V-3	Perspectives	124
V-3.1	XRF quantification model	124
V-3.2	Single shot GEXRF measurements	125
V-3.3	Grazing emission x-ray absorption spectroscopy	125
	Glossary	127
	List of Figures	131
	List of Tables	133
	Bibliography	135
	Appendices	141
	MATLAB functions	143
A	vonHamosSpot function	145
B	spe_read function	151
C	choose_files function	153
D	GEXRF_island function	155
	MATLAB tutorials	159
E	Spectrometer parameters correction	161
F	GEXRF profile creation	169
	Acknowledgments	179
	Curriculum Vitae	181

Summary

The present Ph.D. thesis was realized in the Atomic and X-Ray Physics ([AXP](#)) research group of Prof. Jean-Claude Dousse at the Physics Department of the University of Fribourg. It is devoted to the development of high-resolution X-Ray Fluorescence ([XRF](#)) methods at grazing angles, namely the Grazing Emission ([GEXRF](#)) and Grazing Incidence ([GIXRF](#)) X-Ray Fluorescence methods. These grazing angle techniques probe a sample in the near surface area and allow to perform trace-element analysis, surface contamination control, depth profiling of buried impurities or implanted ions, structure determination of layers and interfaces, and characterization of on-surface particles. A particular aim of this thesis was to establish the relations between the surface morphology and fluorescence intensity of a sample in the regimes of grazing emission and grazing incidence.

Most measurements were performed at synchrotron radiation facilities, namely at the European Synchrotron Radiation Facility ([ESRF](#)), in Grenoble, France, at the Swiss Light Source ([SLS](#)), at [PSI](#), in Villigen, Switzerland, and at the Electron Storage Ring BESSY II, in Berlin, Germany. The [GEXRF](#) projects were carried out using the von Hamos bent crystal spectrometer of Fribourg, whereas the [GIXRF](#) measurements were performed with the ultra-high vacuum x-ray spectrometry chamber and the 6-axis ultra-high vacuum manipulator of the Physikalisch-Technische Bundesanstalt ([PTB](#)).

The thesis is organized as follows:

In [Chapter I](#) the basic concepts concerning the grazing angle [XRF](#) methods and their applications for nanostructures' characterisation are presented together with an outlook of the related literature.

In [Chapter II](#) the experiments carried out for this study are described in detail. In particular, the instruments used to perform the [GEXRF](#) and [GIXRF](#) measurements as

well as the different synchrotron radiation beamlines where these measurements took place are presented. The investigated samples and the methods used to prepare them are also discussed in this part.

Chapter III is devoted to the data analysis and data processing methods. In order to interpret correctly the measured GEXRF spectra, new software packages were developed. They are presented in this chapter while a more detailed description of them is given in the Appendices, at the end of the thesis. First, a new algorithm for the analysis of CCD single and multiple hit events is discussed. The problems related to the correction of the CCD images in the von Hamos geometry are then addressed with a special focus on the properties of images collected in the grazing emission arrangement. A novel analytical method based on Geometrical Optics (GO) for simulation of the XRF angular profiles of nanostructures and nanoparticles densely distributed on flat substrates is also presented. Finally the influence of the grazing incidence geometry on the effective flux of the exciting radiation for particulate media is described.

Chapter IV presents the experimental results obtained for sample of various morphologies characterized by periodic and evenly distributed structures. The characteristic spectral features and trends of the measured GEXRF and GIXRF angular profiles are described and discussed. The experimental results are compared to the theoretical predictions from the GO model and to the values obtained from X-ray Standing Wave (XSW) simulations. At the end of this chapter, the experimental difficulties encountered during the different projects are discussed.

In Chapter V conclusions about the most significant aspects of the thesis are drawn. Future perspectives concerning possible applications of the described x-ray grazing angle techniques and developed data analysis methods are outlined.

Résumé

La présente thèse de doctorat a été réalisée au Département de Physique de l'Université de Fribourg dans le groupe de recherche « Atomic and X-Ray Physics » ([AXP](#)) du Prof. Jean-Claude Dousse. Elle est consacrée au développement de méthodes d'analyse basées sur la fluorescence X en haute-résolution et à angles rasants, plus spécifiquement la fluorescence X à émission rasante ([GEXRF](#)) et la fluorescence X à incidence rasante ([GIXRF](#)). Ces méthodes d'analyse à angles rasants permettent de sonder la surface d'échantillons ainsi que la région proche de la surface pour en extraire des informations comme la présence d'éléments-traces et la contamination de surface, la distribution en profondeur d'impuretés ou d'ions implantés, la structure de couches minces et d'interfaces et la caractérisation de particules déposées à la surface de substrats plats. Un objectif spécifique de cette étude était de déterminer comment l'intensité de fluorescence dépendait de la morphologie de la surface de l'échantillon pour les cas de l'émission rasante et de l'incidence rasante.

La plupart des mesures présentées dans la thèse ont été effectuées auprès de sources de rayonnement synchrotronique comme l'Installation européenne de rayonnement synchrotron ([ESRF](#)) à Grenoble, France, la Source de lumière suisse ([SLS](#)) de l'Institut Paul Scherrer à Villigen, Suisse et l'Anneau de stockage d'électrons BESSY II à Berlin, Allemagne. Les mesures [GEXRF](#) ont été réalisées à l'aide du spectromètre à cristal courbé von Hamos de Fribourg tandis que les mesures [GIXRF](#) ont été effectuées en utilisant la chambre ultravide de spectroscopie X et le manipulateur ultravide à 6 axes du « Physikalisch-Technische Bundesanstalt » ([PTB](#)) de Berlin.

Le mémoire de thèse est articulé de la manière suivante :

Dans le Chapitre I, les fondements des méthodes [XRF](#) à angles rasants ainsi que leur application pour la caractérisation de nanostructures sont présentés avec un passage en revue de la littérature existante.

Dans le Chapitre II, les expériences réalisées sont décrites en détails avec, en particulier, une présentation complète des lignes de faisceau sur lesquelles les mesures ont été effectuées ainsi que des instruments utilisés pour ces mesures. Les échantillons analysés et les méthodes utilisées pour la préparation de ces derniers sont également discutés dans ce chapitre.

Le Chapitre III concerne les méthodes utilisées pour l'analyse et le traitement des données. Pour pouvoir interpréter correctement les spectres [GEXRF](#), de nouveaux logiciels ont dû être développés. Les programmes correspondants sont présentés dans ce chapitre, une description plus complète de ces derniers étant donnée dans les annexes. Tout d'abord un nouvel algorithme développé pour l'analyse d'événements correspondant à des impacts simple et multiple sur la caméra [CCD](#) est discuté. Ensuite sont abordés des problèmes concernant la correction des images [CCD](#) obtenues en géométrie von Hamos avec un accent principal sur le cas de l'émission rasante X. On trouvera également dans ce chapitre la présentation d'un nouveau modèle basé sur l'optique géométrique ([GO](#)) pour la simulation des spectres [XRF](#) angulaires de nanostructures et de distributions denses de nanoparticules déposées sur des substrats plats. Enfin, l'influence de la géométrie à incidence rasante sur le flux du faisceau de photons utilisé pour irradier l'échantillon est analysée pour le cas des matériaux granulaires.

Le Chapitre IV présente les résultats obtenus pour des échantillons ayant des morphologies de surface correspondant à des distributions soit uniformes soit périodiques de structures de diverses formes et faites d'éléments différents. Les caractéristiques spectrales des profils angulaires [GEXRF](#) et [GIXRF](#) de ces échantillons sont présentées et commentées. Les résultats expérimentaux sont comparés aux valeurs théoriques obtenues à partir du nouveau modèle géométrique ([GO](#)) et du modèle des champs d'ondes stationnaires X ([XSW](#)). Le chapitre se termine avec un inventaire des principales difficultés expérimentales rencontrées durant la réalisation des différents projets.

Les conclusions principales du travail sont énoncées dans le Chapitre V. Une discussion sur les possibilités d'application des techniques de spectroscopie X à angles rasants et des méthodes d'analyse développées dans la thèse clôt ce dernier chapitre.

Chapter I

Introduction

I-1 Total reflection of x-rays

Total reflection of electromagnetic waves passing from a material with a higher refractive index to a material with a lower refractive index is a well known physical phenomenon. In the x-ray regime such an effect is also observed and was described by Compton already in 1923 [1].

In the x-ray regime the refractive index n is given by the following formula:

$$n = 1 - \delta + i\beta. \quad (\text{I.1})$$

The real part of the refraction index $1 - \delta$ is determined by the so called decrement δ which is related to the radiation dispersion and is given by:

$$\delta = \frac{N_A}{2\pi} r_0 \lambda^2 \rho \sum_j \frac{n_j Z_j}{A_j}, \quad (\text{I.2})$$

where N_A is the Avogadro number, r_0 the classical electron radius, λ the wavelength of the incoming x-ray radiation, ρ the density of the material and n_j , Z_j and A_j the molar fraction, atomic number and atomic mass of the j^{th} element of the material, respectively. The imaginary component β is a measure of the radiation attenuation in the material:

$$\beta = \frac{1}{4\pi} \mu \lambda, \quad (\text{I.3})$$

where μ is the linear mass absorption coefficient. The coefficients δ and β are both positive, and in the x-ray regime they are in the order of $\sim 10^{-6}$.

More precisely the refractive index can be calculated directly from the scattering factors f_1 and f_2 [2, 3]:

$$n = 1 - \frac{N_A}{2\pi} r_0 \lambda^2 \rho \sum_j \frac{n_j (f_{1j} - i f_{2j})}{A_j}. \quad (\text{I.4})$$

Comparing above equation with (I.2) and (I.3) the following relations can be deduced:

$$f_{1j} = Z_j, \quad (\text{I.5})$$

and:

$$\mu = 2N_A r_0 \lambda \rho \sum_j \frac{n_j f_{2j}}{A_j} \quad (\text{I.6})$$

Actually, since f_{1j} is defined as the ratio of the amplitude of the wave scattered by the j^{th} atom with respect to the one scattered by a single electron, Z_j corresponds to the maximum value of f_{1j} . According to Snell's law the total reflection of a radiation passing from a material with refractive index n_1 to a material with refractive index n_2

I INTRODUCTION

occurs for the glancing angles¹ smaller than the critical angle φ_c :

$$\varphi_c = \arccos \frac{n_2}{n_1}. \quad (\text{I.7})$$

The above equation entails the following condition on the refractive indexes:

$$n_2 < n_1. \quad (\text{I.8})$$

Thus, in the x-ray regime where $\Re n < 1$, the total reflection occurs in vacuum resulting in the so called total external reflection phenomena.

We should note, however, that even at total reflection conditions the evanescent radiation penetrates the near interface area of the material with lower refractive index. This is due to the electromagnetic field continuity condition.

Because for x-rays the refractive index is close to one, the critical angles are very small – usually not bigger than 1° .

I-2 X-ray fluorescence techniques related to the total reflection of x-rays

I-2.1 Total reflection x-ray fluorescence

In the [Total-reflection X-Ray Fluorescence \(TXRF\)](#) [4] technique the reflected radiation is used as an excitation probe that excites the sample only in the region above the surface and several nanometers below. The resulting fluorescence radiation is measured by a detector positioned on the top of the sample surface.

As all [X-Ray Fluorescence \(XRF\)](#) methods [5] the [TXRF](#) is also a nondestructive and element sensitive (and to some extent chemical sensitive) method. Additionally the method profits from a substantial decrease of the spectral background signal originating from the substrate material.

The [TXRF](#) method is mainly used for micro- and trace-element analysis of evaporated solvents, aerosols and powders. Another common application is the surface contamination control. The detection limits are in the order of picogram to femtogram if pre-concentration methods are applied.

A detailed description of the [TXRF](#) method can be found in Klockenkämper’s monograph [4] and in several review papers (see, *e.g.*, [6, 7]).

¹Note that here the angle of reflection is defined as a glancing angle, *i.e.*, the angle between the radiation direction and the sample surface. This is a common convention in grazing angle x-ray techniques.

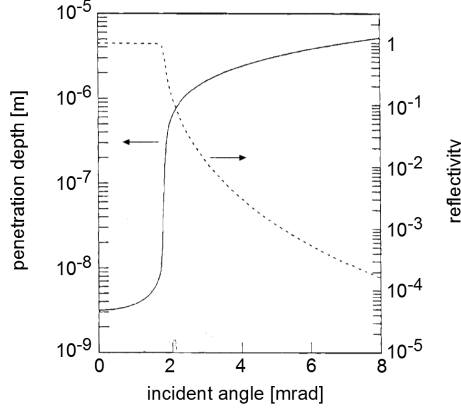


Figure I.1: Calculated penetration depth (solid line) and reflectivity (dashed line) for Mo $K\alpha$ x-ray radiation impinging on silicon. The critical angle is 1.8 mrad. [8]

The [Grazing Incidence X-Ray Fluorescence \(GIXRF\)](#) technique, called also [Angle Dependent X-Ray Fluorescence \(ADXRF\)](#) is an extension of [TXRF](#) where the x-ray fluorescence is measured as a function of the incidence angle².

I-2.2 Grazing incidence x-ray fluorescence

By varying the glancing angle continuously at very small angles the access to the sample structure in near surface area below the interface can be obtained. [Figure I.1](#) shows the penetration depth change when the incidence angle is varied. For incident angles below the critical angle, only the first few nanometers in the depth direction are reached by the incident radiation. Farther from the surface the x-rays are attenuated due to their evanescence character. For incident angles larger than the critical angle, the sample becomes sensitive to x-rays penetrating deeper into the sample. In this angular range the accessible depth region is limited by the material absorption coefficient for the incident x-rays.

The interference of the incident and reflected x-rays is another phenomenon that affects the [GIXRF](#) intensity. Also the interference pattern changes with the incident angle.

In addition to [TXRF](#) applications [GIXRF](#) is also employed for nondestructive depth profiling [9], structure determination of layers and interfaces, and for the characterisation of surface particles.

More information on [GIXRF](#) can be found in [4, 6–8].

²Here we should clarify the mismatch nomenclature found in the literature. Both [TXRF](#) and [GIXRF](#) are referenced as a general name for all x-ray fluorescence techniques employing the grazing incidence of x-ray radiation. However, [TXRF](#) is more often used when fixed angles of incidence below the critical angle are employed. [GIXRF](#) in turn applies to measurements where the fluorescence intensity is measured as a function of the incidence angle which is varied around the critical angle. Synchrotron-radiation based [GIXRF](#) is also addressed as [X-ray Standing Wave \(XSW\)](#) technique.

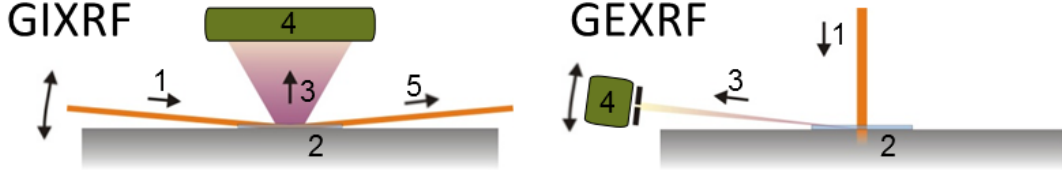


Figure I.2: Comparison of the [GIXRF](#) and [GEXRF](#) geometries. 1. incident beam, 2. sample, 3. detected fluorescent radiation, 4. detector, 5. reflected beam. In the [GIXRF](#) setup the incident x-ray radiation is collimated and the angle of incidence is tunable; the fluorescent radiation is detected perpendicularly to the sample surface within a large solid angle. In the [GEXRF](#) setup the fluorescent radiation is detected within a small solid angle and the angle of detection is tunable while the beam incidence angle is large, *e.g.*, 90° . In the case of [GEXRF](#) the excitation can be produced by any kind of ionizing radiation (x-ray radiation, electron beam, ion beam).

I-2.3 Grazing emission x-ray fluorescence

The operational principle of the [Grazing Emission X-Ray Fluorescence \(GEXRF\)](#) technique [10–13] consists in measuring the intensity evolution of an excited x-ray fluorescence line around its critical angle of total reflection. [GEXRF](#) can be regarded as a time-reversed [TXRF](#) or [GIXRF](#) experiment where the x-ray emitter and detector are exchanged (see [Figure I.2](#)). Thus in behalf of the reciprocity theorem [14] the [GEXRF](#) theoretical description can be based on derivations made for [TXRF](#) and [GIXRF](#) [10, 15]. However, more formal approaches employing the Maxwell’s equations [12, 13] and field expansion in plane waves [16, 17] can be found in the literature.

Thereupon the angular evolution of [GEXRF](#) is equivalent to that of [GIXRF](#). For exit angles below the critical angle, only the first few nanometers in the depth direction contribute to the measured fluorescence intensity, the x-rays emitted far from the surface vanishing due to their evanescence. For exit angles larger than the critical angle, the x-ray fluorescence detection setup becomes sensitive to x-rays emitted deeper inside the sample. In the latter case the accessible depth region is limited by the self-absorption of the fluorescence x-rays.

The [GEXRF](#) setup allows the use of wavelength-dispersive instruments for the detection of the fluorescence radiation [18–20]. This provides a much higher spectral resolution and thus a better separation of the fluorescence lines, which is of prime importance for light elements (from $Z > 4$). A further advantage of the [GEXRF](#) setup is the possibility of performing microanalysis and surface mapping, provided a sufficiently intense focused X-ray source is available [20]. Its main drawback resides in the lack of flexibility for the choice of the critical angle φ_c for total reflection. As the latter depends on the photon energy, in the [GIXRF](#) method φ_c can be varied continuously

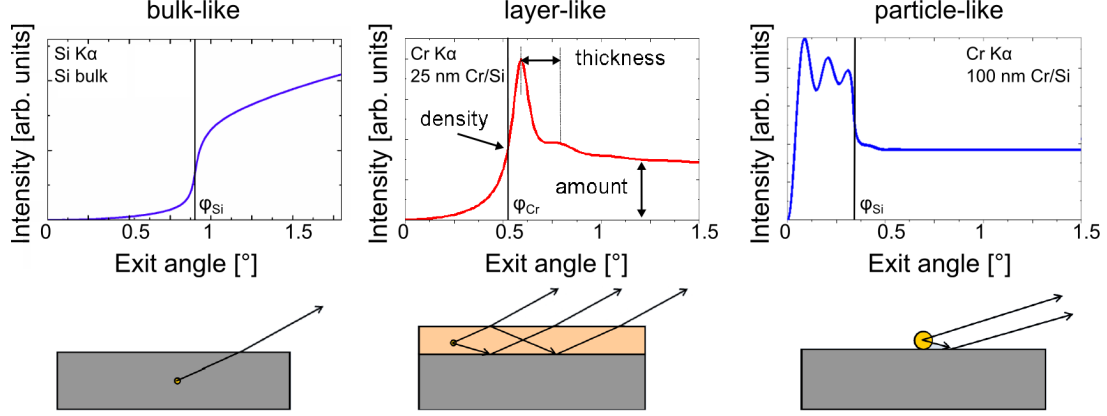


Figure I.3: Three types of [GEXRF](#) angular profiles for bulk-like, layer-like and particle-like structures. The critical angle positions correspond to the inflection points of the profiles. As shown in the middle panel, some information about the sample structure can be extracted straightforwardly from the measured profile: the critical angle position is indeed related to the optical density of the material, the distance between neighbour interference fringes correspond to the layer thickness, and the fluorescence intensity for $\varphi \gg \varphi_c$ is proportional to the total amount of fluorescent atoms. [GIXRF](#) profiles present similar features.

by tuning the energy of the incoming beam. This is, however, not possible with the [GEXRF](#) technique since in this case the critical angles are determined by the energies of the fluorescence lines of the investigated element.

A detailed description of the [GEXRF](#) method and of possible applications can be found in the following review papers [6, 13, 21, 22].

I-3 GIXRF and GEXRF application for nanostructures characterisation

The [GIXRF](#) and [GEXRF](#) as its reciprocal method are well known for their utility in surface analysis [4–7, 13, 21, 22]. As stated before they serve as very sensitive tools for trace element analysis [19, 20], thin layers' characterisation [23] and non-destructive depth profiling of implanted impurities [9, 24]. Their usefulness for nanoparticles' characterisation has also been proven [16, 17, 25–29].

Depending on the sample's morphology three well described types of [GEXRF](#) and [GIXRF](#) angular profiles are distinguished [11, 12]: bulk-like, layer-like and particle-like (see [Figure I.3](#)). For the bulk structure the emitted radiation is refracted once at the vacuum-bulk interface and the evolution of [GEXRF](#) follows approximately the inverse of the reflection coefficient of the bulk material. For the layer-like structure, for angles

slightly above the critical angle, an interference pattern in the detected fluorescence can be observed that results from the multiple reflections on the top and bottom interfaces of the layer [15]. For particle-like structures the detected x-rays result from the direct and singly reflected radiation. Thereby the radiation intensity is doubled below the critical angle of the support material.

I-3.1 Angular profiles of surfaces containing individual particles

The angular profiles of surfaces containing individual particles have been studied both theoretically [17, 27] and experimentally [25–27]. In [17] the GEXRF angular profiles of small particles located on a flat support were analyzed theoretically. In [27] similar theoretical investigations were performed for the case of GIXRF with the use of the XSW simulations. In addition to the particle shape also the particle size distribution and the x-ray coherence length were taken into account.

In both papers [17, 27] the appearing interference pattern was shown to contain valuable information about the particle structure and composition. However, as shown in [27] the nonuniform particle size distribution and the limited coherence length significantly reduce the interferences.

The experimental results reported in [25–27] confirm the theoretical predictions, demonstrating the utility of the method but also its ambiguity with respect to the interpretation of the data.

I-3.2 Angular profiles of dense particles’ distributions

The angular profiles of the x-ray fluorescence emitted by surfaces characterized by dense particles’ distributions are still not fully understood. Such structures can be considered as transition structures from particle-like to layer-like structures. In the literature they are usually treated as rough layer-like surfaces, the roughness being introduced as:

- a small perturbation of the interface potential within the Nevot-Croce model,
- a stack of layers with reduced average densities, or
- a composition of layers of different thicknesses.

A slightly different approach was presented in [30] where, in order to calculate the influence of the absorption effects, the sample surface was considered to be made of a series small towers of variable height and width. Yet, as stated by the authors, at the current stage of the simulations the results are still not satisfying.

I-3.2.1 Nevot-Croce model

Very dense particles' distributions can be regarded as rough layers, the surface and interfacial roughness being quantitatively described with the Nevot-Croce model [31–34]. In this theoretical model the effect of the roughness is calculated using the distorted-wave Born approximation in which the roughness is considered as a small perturbation of an electromagnetic potential with a Gaussian random distribution along the interface.

In the Nevot-Croce model, as compared to a smooth surface, both the reflectivity r and transmission t coefficients are modified as follows:

$$\tilde{t} = t \cdot \exp\left(\frac{-(k_y - k'_y)^2}{2} \sigma_h^2\right), \quad (\text{I.9})$$

$$\tilde{r} = r \cdot \exp(-k_y^2 \sigma_h^2), \quad (\text{I.10})$$

where k_y and k'_y correspond to the incident and refracted wave vectors' components perpendicular to the sample surface, respectively, and σ_h^2 is the variance of the Gaussian distribution of the potential.

The relations (I.9) and (I.10) are valid up to $O(k_y \sigma_h)$. Thus they can be used for small roughnesses fulfilling the condition:

$$k_y \sigma_h \ll 1 \quad (\text{I.11})$$

Calculations with the Nevot-Croce model up to $O(k_y^2 \sigma_h^2)$ and their application to GIXRF were performed by de Boer [35–37]. The resulting formulas depend on the rms value of the interface roughness σ_h , its lateral correlation length ξ and its degree of perpendicular correlation, as well as on the degree of jaggedness. The results are valid for $k_y \sigma_h \ll 1$ and $\xi k_y^2 / |\vec{k}| \ll 1$ or $\xi k_y^2 / |\vec{k}| \gg 1$.

The distorted wave Born approximation has been explicitly applied to dense distributions of islands on surfaces taking into account the correlation between particles' size and spacing in Ref. [38, 39]. However only the x-ray scattering was considered without direct links to GIXRF.

The Nevot-Croce formalism is commonly used for roughness compliance in GIXRF calculations [40]. However, the model is likely to fail for large rms values of the interfacial roughness. In general it is not suitable for grainy structures with separated components.

I-3.2.2 Stack of layers of various density model

The grainy region can be described as a transition layer in which the refractive index varies continuously with the depth [33, 41]. The interface can be then divided into

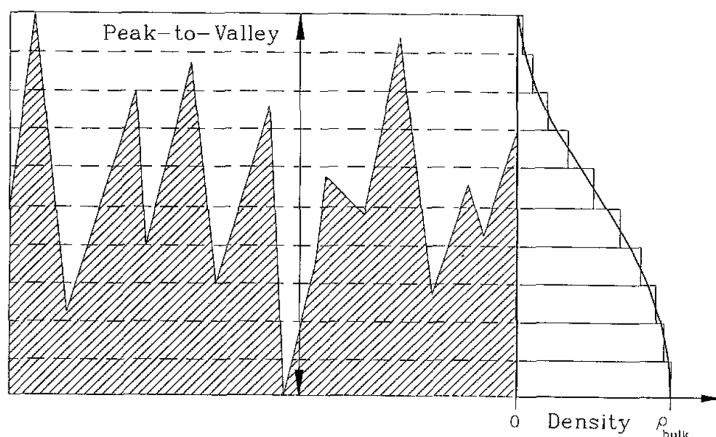


Figure I.4: Illustration of the stack of layers of various density model. The roughness is described by a stack of virtual layers with increasing density from zero to bulk. [41]

elementary layers in which the refractive index depends on the roughness distribution (see Figure I.4). In the most crude variant of this method the whole grainy region is approximated with a single layer of a low optical density [28].

In this model the structure height correlations and the local variation of the interface slope are not considered.

I-3.2.3 Linear combination of angular profiles

If the correlation length ξ of the height distribution is large enough, the resulting angular profile can be approximated by the sum of the profiles corresponding to layers of various thicknesses. The method was proved to give good results when applied to large islands [19, 42]. In [43] the method was applied to both particle-like and layer-like profiles.

A limitation of the method resides in the assumption that the different parts of the structure do not interact with each other.

I-3.2.4 Limitations of the models

While being certainly useful, the mentioned models employed for dense particles' distributions are too simple and do not cover phenomena such as highly correlated height distributions and large roughnesses [37], nor the propagation of the x-ray radiation through several particles [44].

However, a correct interpretation of these intermediate profiles would be of high importance, in particular for nanostructures' investigations and for TXRF measurements of droplets where the quantification problem is one of the main issues.

I-3.3 Periodic structures

Periodic structures might represent a further model for the description of particle-layer transition structures. With the structuration techniques available today almost any arbitrary structure can be produced. Thus the effects of the pattern size, distance and surface coverage can be examined and then simulated with relatively simple models.

I-3.3.1 Grating-like substrates

The use of periodic substrates for GIXRF investigations has been reported by Tsuji *et al.* in [44]. In comparison to smooth surfaces a clear peak of fluorescence intensity was observed in the angular profile near the critical angle.

A theoretical description of the GEXRF with a grating-like substrate was presented in [16]. As a result of the diffraction on the surface grating, distinct peaks were predicted to appear in the x-ray signal angular dependence. The magnitude of the latter can exceed several times the value of the x-ray intensity obtained with the use of a flat substrate under the same conditions of excitation.

The angular peaks positions φ_M can be approximated by:

$$\cos \varphi_M = M \frac{\lambda}{p}, \quad M \in \mathbb{N} \quad (\text{I.12})$$

where λ is the wavelength of the fluorescence x-rays, and p is the period of the grating structure. Because the x-ray wavelengths are very small the above equation implies that the diffraction peaks are only visible for soft x-rays and very dense ($p < 1 \mu\text{m}$) gratings.

I-3.3.2 Multiple reflections in periodic structures

As for layer structures, x-rays can be reflected many times by a periodic structure. This means that the x-ray path consists of multiple reflections and the single radiation that leaves the structure is the radiation refracted at the top interface.

Such a situation can happen if the distance between the consecutive reflections on the top or bottom interfaces of the structure is a fraction or a multiple of the structure period (see Figure I.5). Provided that the ray path is not refracted at the side interfaces of the structure, this condition can be written as follows:

$$\tan \theta_M = M \frac{h}{p}, \quad M \in \mathbb{Q}_+ \quad (\text{I.13})$$

where h and p are the height and period of the structure, respectively, and θ is the angle between the x-ray path and the direction parallel to the interface. If the radiation exits

I INTRODUCTION

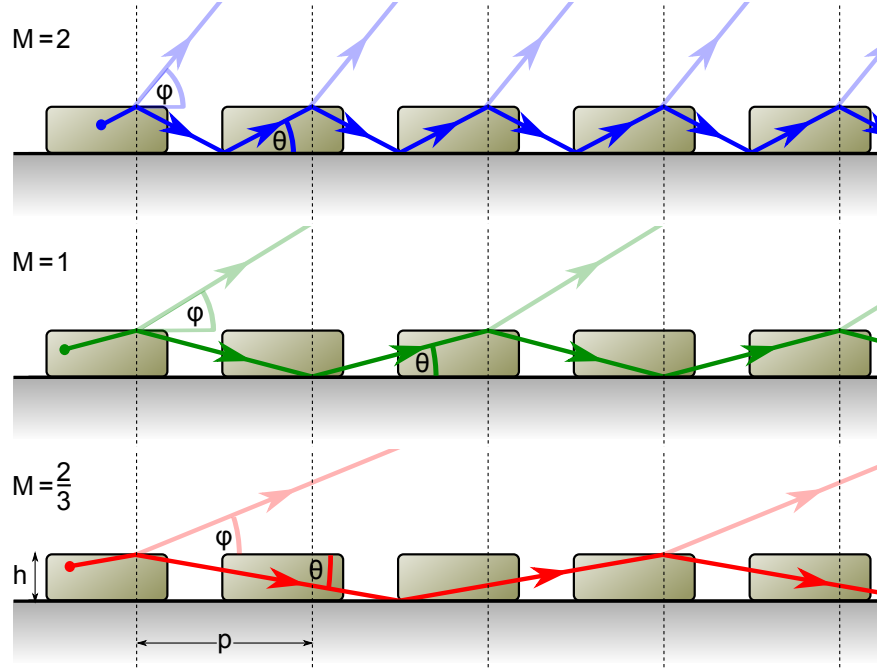


Figure I.5: Multiple reflections in a periodic structure. The period of the structure is indicated with dashed lines.

the sample by a side flank of the structure, θ can be approximated with the grazing angle φ , whereas if it exits the structure at the top interface θ is given by:

$$\theta = \arccos \frac{\cos \varphi}{n}, \quad (\text{I.14})$$

where n is the refraction index of the material.

In the periodic case the distance between the resulting [XRF](#) angular profile structures does not depend on the wavelength of the x-ray radiation.

Chapter II

Experimental

II.A GEXRF measurements

The presented [GEXRF](#) measurements were performed by means of the high-resolution von Hamos curved crystal x-ray spectrometer of the University of Fribourg [45]. In order to realise the synchrotron radiation based high-resolution [GEXRF](#) measurements the spectrometer was transported to the [European Synchrotron Radiation Facility \(ESRF\)](#) in Grenoble, France (beam line ID21) and to the [Swiss Light Source \(SLS\)](#) in Villigen, Switzerland (SuperXAS beam line).

II.A-1 Von Hamos spectrometer

The von Hamos spectrometer consists mainly of three components (see [Figure II.A.1](#)):

- an x-ray source,
- a cylindrically-curved Bragg crystal, and
- a position-sensitive x-ray detector.

In the von Hamos geometry the crystal is bent cylindrically around the x-axis which is parallel to the direction of dispersion and provides vertical focusing in the non-dispersive z-direction.

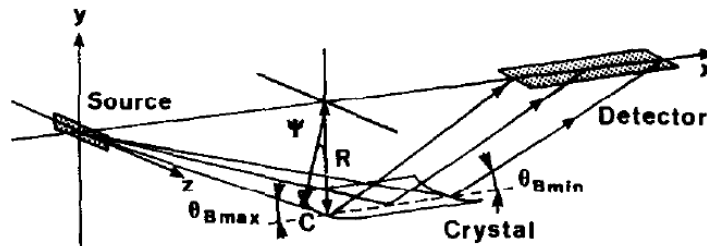


Figure II.A.1: Schematic drawing of the von Hamos geometry from Ref. [45].

II EXPERIMENTAL

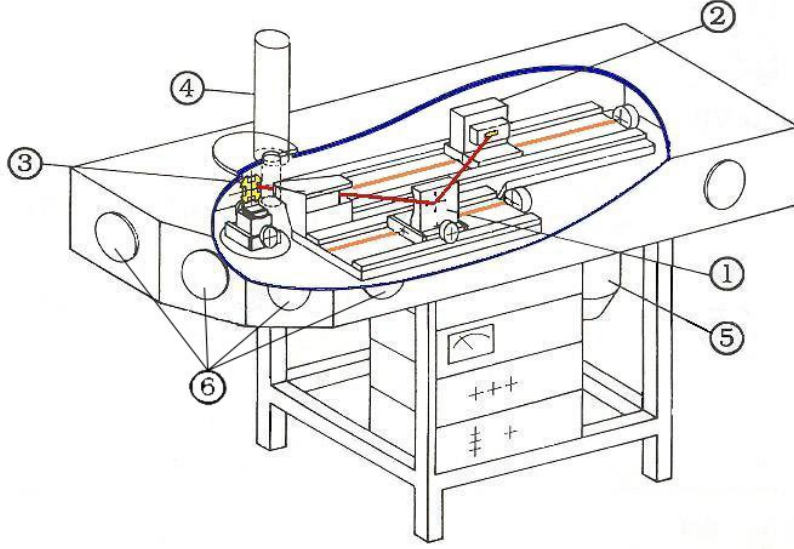


Figure II.A.2: Schematic view of the von Hamos spectrometer of Fribourg: (1) crystal, (2) CCD detector, (3) target holder, (4) x-ray tube, (5) vacuum pump and (6) beam ports.

The use of a wavelength-dispersive setup brings two main advantages: a high angular (and consequently energy) resolution (see [Sub-chapter III.B](#) on page 71) and a high background rejection.

Most of the background events produced in the sample have a different energy than the one of the fluorescence x-rays of interest. As a consequence, they are not diffracted by the crystal and are thus eliminated. Remaining background events are related to scattered photons, cosmic rays and electronic noise of the detector. Two algorithms for background subtraction are presented in [Sub-chapter III.A](#) on page 61.

II.A-1.1 Spectrometer chamber

The spectrometer is enclosed in a $180 \times 60 \times 24.5 \text{ cm}^3$ stainless steel chamber mounted on a mobile stand (see [Figure II.A.2](#)). The chamber can be pumped to about 10^{-7} mbar by a turbo-molecular pump and a two-stage rotary pump.

The chamber is equipped with four beam ports located in such a way that the direction of the incoming beam relative to the axis of crystal curvature equals 0° , 30° , 60° and 90° . The ports allow the connection to a synchrotron or ion accelerator beam line or the installation of an electron gun or collimated x-ray source. Additionally the ports can be used as view-ports for the visual control of the experiment under vacuum or to mount feedthrough electrical connectors for additional remote-controlled devices inside the chamber.

Three circular ports on the top of the spectrometer chamber permit access for the target, crystal and detector replacement. An x-ray tube can be mounted in place of the circular port above the target system.

In order to reduce the background an Al-Cu-Pb shielding separates the target chamber of the spectrometer from the crystal and detector parts.

II.A-1.2 Construction details and motorisation

For a fixed position of the crystal and detector, a certain angular range and consequently a certain energy interval is covered by the spectrometer. The size of the energy interval which varies with the central Bragg angle is determined by the detector extension in the direction of dispersion. In order to provide a wider range of available Bragg angles the crystal and the detector can be moved along translation axes (labeled DET for the detector and CRY for the crystal) which are both parallel to the dispersion axis. This permits to vary the Bragg angles from 24.4° to 61.1° . When changing the central Bragg angle the source-to-crystal and crystal-to-detector distances are both varied but kept equal.

In order to correct for deviations of the crystal curvature from the nominal value of 25.4 cm, the crystal can also be moved along an axis labeled CRF which is coplanar and perpendicular to the crystal and detector translation axes.

In the regular operation mode the x-ray source is defined by a rectangular slit placed on the detector axis. The real x-ray fluorescence source is located behind the slit. For each Bragg angle, the fluorescence source should be positioned so that its center lies on the straight line passing through the slit and the crystal center. For this reason, the target holder can be translated along an horizontal axis, labeled TAF, which is perpendicular to the CRY and detector DET axes (see [Figure II.A.3](#)). A rod connects the target holder carriage to the slit-rotation system and ensures an automatic alignment of the slit for any displacement of the target.

In addition the target holder can be moved along an axis, labeled TAT, parallel and coplanar to the CRY and DET axes and rotated around a vertical axis, labeled TAL, tangential to the surface of the fluorescence source and perpendicular to the plane determined by the CRY and DET axes.

All the above mentioned axes are equipped with remote-controlled step motors and their main characteristics can be found in [Table II.A.1](#). An overview of the translation axes is also depicted in [Figure II.A.4](#).

II EXPERIMENTAL

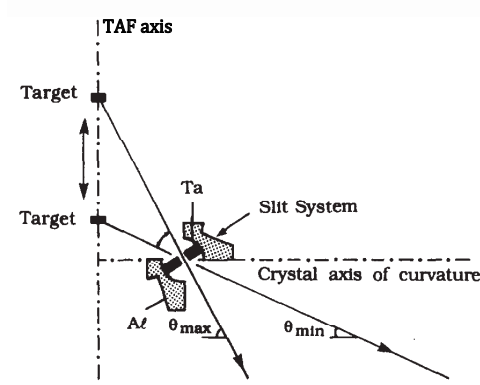


Figure II.A.3: Target-slit system of the von Hamos spectrometer (from [45]).

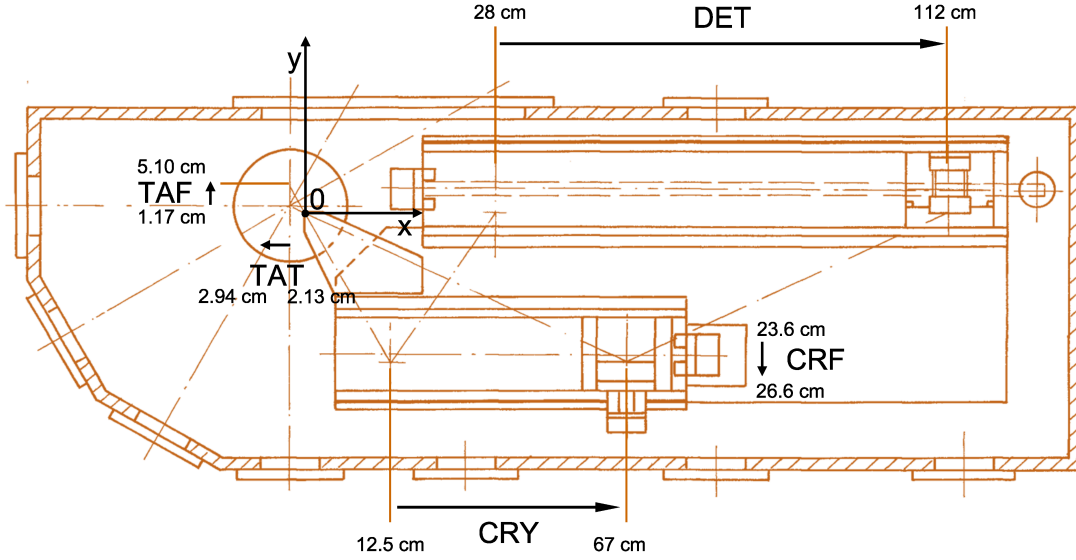


Figure II.A.4: Spectrometer chamber with indication of the motion axes.

element moved	axis name	parallel to	step	range
crystal	CRY	x	$5\ \mu\text{m}$	12.5 – 67.0 cm
	CRF	y	$2.5\ \mu\text{m}$	23.6 – 26.6 cm
detector	DET	x	$5\ \mu\text{m}$	28 – 112 cm
target	TAF	y	$2.5\ \mu\text{m}$	1.17 – 5.10 cm
	TAT	x	$2.5\ \mu\text{m}$	2.13 – 2.94 cm
	TAL	z	0.00225°	$-58.1 - 90.8^\circ$ *

* Angle between the TAF axis and the normal to the sample surface.

Table II.A.1: Step motors' characteristics. The ranges of the translation axes are given relative to the slit position.

II.A-1.3 Bragg crystals

The spectrometer can be equipped with different crystals whose dimensions and characteristics are listed in Table II.A.2. For all crystals, the nominal radius of curvature ρ is equal to 254 mm. For the measurements, the chosen crystal is mounted on a moveable carriage that can be translated along the CRY and CRF axes.

Crystal	$a \times b \times c$ [mm ³]	h [mm]	$2d$ [Å]	Energy range [keV]
TlAP (001)	$80 \times 50 \times 0.25$	20.60	25.772	0.544 – 1.178
ADP (101)	$100 \times 50 \times 0.30$	20.80	10.642	1.317 – 2.853
SiO ₂ ($\bar{1}\bar{1}0$)	$100 \times 50 \times 0.15$	20.55	8.5096	1.647 – 3.568
LiF (200)	$99 \times 46 \times 0.60$	21.15	4.0280	3.480 – 7.538
Ge (220)	$99 \times 50 \times 0.20$	20.30	4.0000	3.504 – 7.591
Si (220)	$85 \times 50 \times 0.25$	20.30	3.8410	3.649 – 7.849
SiO ₂ ($\bar{2}\bar{2}3$)	$100 \times 50 \times 0.40$	21.00	2.7500	5.097 – 11.041
SiO ₂ ($\bar{2}\bar{2}3$)	$85 \times 50 \times 0.30$	20.40	2.7500	5.097 – 11.041
LiF (420)	$80 \times 50 \times 1.10$	21.10	1.8010	7.782 – 16.859

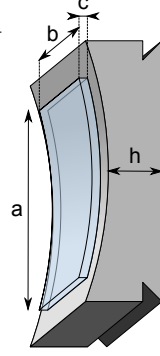


Table II.A.2: Crystals' characteristics.

II.A-1.4 Detector

For the detection of the diffracted x-rays a two-dimensional back-illuminated [Charge-Coupled Device \(CCD\)](#) camera is used. A detailed description of the detector can be found in [46].

The [CCD](#) is 2.68 cm long (in the dispersion direction) and 0.80 cm high and consists of 1340×400 pixels, each pixel having a size of $20 \times 20 \mu\text{m}^2$. The [CCD](#) chip is cooled down to -45° by a cold finger mounted on a water cooled two-stage [Peltier element](#). The cooling limits the dark charge noise of the [CCD](#).

For the read-out and digitalization of the [CCD](#) signal, a ST-133 controller from Roper Scientific is used. During the read-out and clean-out process the [CCD](#) is covered by a dedicated x-ray shutter made of stainless steel and Al. The data transfer rate of the ST-133 controller being 1 MHz, the time needed to read-out a full [CCD](#) image amounts to about 0.5 s, while the time for opening or closing the shutter is shorter than 0.2 s.

The use of a [2D](#) detector permits to correct the images for the geometrical aberrations related to the von Hamos geometry and to improve therefore the instrumental broadening of the spectrometer. In addition, the energy resolution capability of the [CCD](#) detector itself permits to sort good x-ray events by filtering the [2D](#)-images with appropriate energy windows. This permits to strongly reduce the background and to

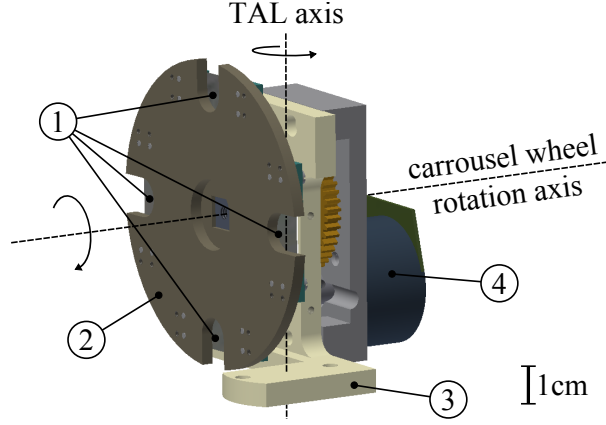


Figure II.A.5: Schematic view of the carousel target holder: (1) samples, (2) Al or Cu made carousel, (3) aluminium support, (4) step motor.

suppress events due to higher orders of diffraction. These two aspects will be discussed in details in [Sub-chapter III.A](#) on page 61 and [Sub-chapter III.B](#) on page 71.

II.A-2 Target holders

For the [GEXRF](#) measurements a precise control of the sample surface orientation relative to the direction of the exiting fluorescence x-rays is needed. This alignment is realized by rotating the sample around the vertical **TAL** axis. The latter is driven by a step motor through a one-stage worm gear-tooth wheel system. The sample rotation corresponding to one step of the motor amounts to 0.00225° , *i.e.*, about $39 \mu\text{rad}$.

For the measurements presented in this work two target holders were used that are described below.

II.A-2.1 Carousel target holder

This revolver barrel-like target holder consists of a motorized carousel on which up to four targets can be fixed simultaneously (see [Figure II.A.5](#)). The samples are mounted on the back side (as seen from the incoming beam) of the carousel wheel. This permits to keep the sample surface at the same position in the y-direction whatever the sample thickness is. The carousel wheel can be rotated around a horizontal axis via a remote-controlled motor, which permits the change of the samples without opening the spectrometer chamber. This is an important asset when measurements are performed at synchrotron radiation facilities, about one hour of beam time being indeed lost each time the spectrometer chamber has to be opened.

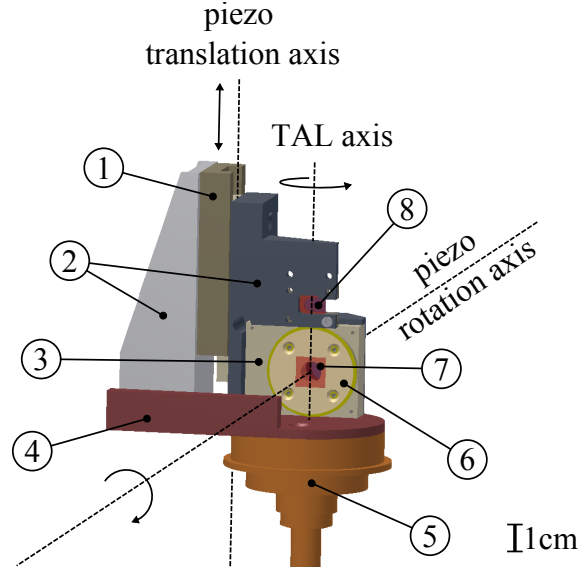


Figure II.A.6: Schematic view of the piezo target holder: (1) translation piezo motor SLC-2460-D-S, (2) aluminium supports, (3) rotary piezo motor SR-2812-S, (4) aluminium base plate, (5) TAL axis motorized stage, (6) aluminium plate screwed on the rotor of the rotary motor, (7) sample, (8) fluorescence screen or 2nd sample.

II.A-2.2 Piezo target holder

For the periodic structures' measurements a dedicated target holder was fabricated that allows the rotation of the sample about an axis perpendicular to the sample surface and a vertical translation along an axis which is parallel to the TAL axis. It should be noted that the exit angle of the fluorescence x-rays is not changed by such a rotation, nor by the vertical translation and that, as a consequence, the Bragg condition is not affected by these sample movements.

II.A-2.2.1 Design

The piezo target holder is depicted in [Figure II.A.6](#). It consists mainly of two piezo motors, one for the vertical translation and one for the rotation. The motors are mounted on aluminium custom machined supports. The whole assembly is fixed onto the motorized three-axes stage (described in [Subsection II.A-1.2](#) on page 29) by two countersunk screws.

Piezo motors were chosen because of their compactness and positioning precision. The main characteristics of the two motors, which are both from the company SmarAct GmbH, are listed below:

- linear positioner SLC-2430-D-S:

II EXPERIMENTAL

- 35 mm course,
- 1 nm precision,
- enlarged blocking force;
- rotary positioner SR-2812-S
 - unlimited rotation,
 - $2\ \mu^\circ$ precision,
 - 8 mm aperture.

Both motors are [Ultra-High Vacuum \(UHV\)](#) compatible and are equipped with an optical positioning sensor. In order to enforce the vertical linear positioner a spring system compensating the weight of the mobile part had to be added later on in the vertical stage.

The piezo motors are steered by a modular control system (MCS) to which the motor are connected via two sensor modules. For the electrical connection between the piezo motors located in the spectrometer chamber and the sensors modules which are outside, [High Vacuum \(HV\)](#) feedthrough LEMO connectors mounted on an unemployed beam port are used. The MCS controller can be connected to a PC by means of an USB interface or controlled manually with an external joystick-like device.

II.A-2.2.2 Spatial constraints

As the overall dimensions of the piezo target holder are somewhat bigger than those of the carrousel target holder, the slit system had to be redesigned in order to enable the use of the spectrometer over the full Bragg angular range (24.4° - 61.1°) or at least the widest possible part of it.

The new slit system is similar to the one presented in [Figure II.A.3](#) on page 30 but the slit width is no longer adjustable. This is, however, not dramatic because in the [GEXRF](#) setup the measurements are performed in the so called slit-less geometry [20] and in the latter geometry the slit is opened to its maximum aperture (about 2 mm).

Nevertheless, due to the enlarged dimensions of the piezo target holder the usable ranges of the TAT, TAF and TAL axes are diminished and, the following spatial constraints should be considered in addition to the limits quoted in [Table II.A.1](#) on page 30:

- TAL rotations should never exceed 20.25°
- TAF and TAT positions should never be simultaneously closer to the slit than 1.375 cm and 2.5 cm, respectively.

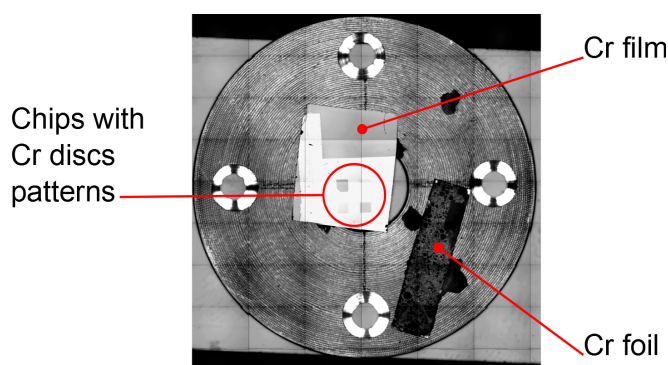


Figure II.A.7: Mosaic photograph of an Al plate employed to fix the samples (here a Cr discs sample made with the Stencil technique, see [Subsection II.C-2.4](#) on page 53) on the rotor of the piezo motor. The thin Cr film was used for the alignment of the Cr discs patterns and the metallic Cr foil for the optimization of the acquisition parameters of the spectrometer.

II.A-2.2.3 Target mounting

The rotary piezo motor is fixed to the aluminium support so that the distance between the front plane of the rotor and the TAL axis is 1.5 mm. The samples are glued (glue Electrodag 1415 from Agar Scientific Ltd) on dedicated aluminium plates (see [Figure II.A.7](#)) which are screwed on the rotor of the piezo motor. For each sample the thickness of the aluminium plate is chosen so that the total thickness of the sample plus backing system is exactly 1.5 mm. As a consequence, the condition that the TAL axis should lie in the sample surface is automatically satisfied.

The use of an intermediate aluminium plate for the target mounting presents the additional advantage of preserving the position of the sample if later on the latter has to be put back on the target holder.

For the mounting of the second target (which can be replaced by a fluorescence screen), the sample is fixed on the rear side of the support (see [Figure II.A.6](#) on page 33) as in the case of the carousel target holder.

II.A-3 ESRF measurements

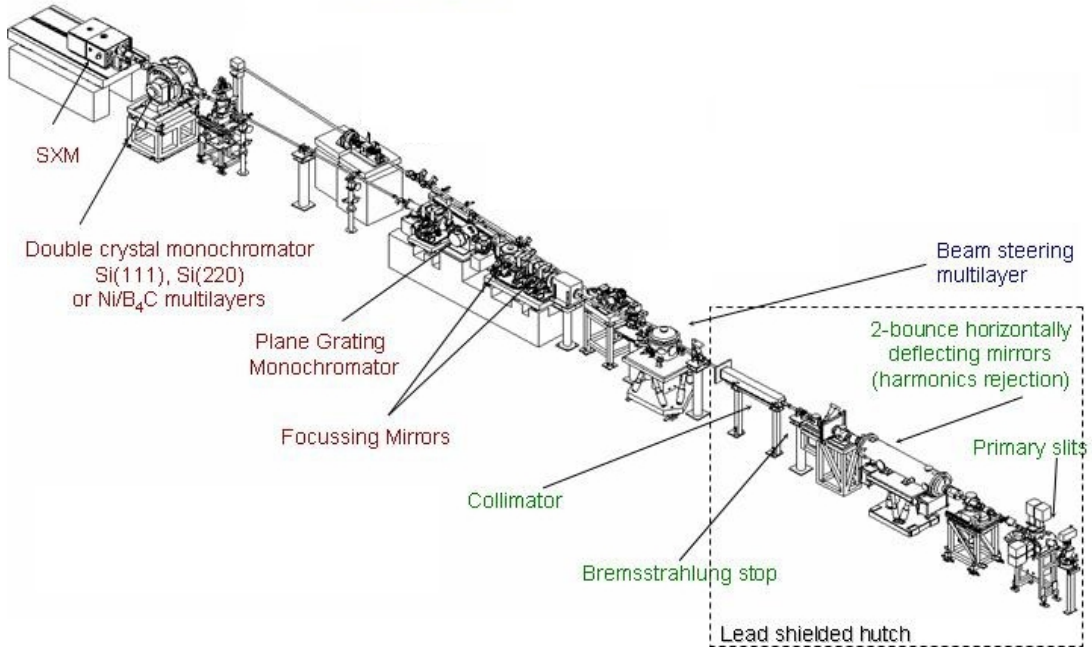
Two experiments were performed at the [ESRF](#), in Grenoble, France, both at the x-ray microscopy beamline ID21. During the first experiment (MI-975), samples with evenly distributed structures (see [Section II.C-1](#) on page 49) were measured. The second experiment (MI-1108) was devoted to the investigation of samples with periodic structures (see [Section II.C-2](#) on page 52). A further objective of the second experiment was to probe the goodness of the theoretical predictions provided by the geometrical optics [GEXRF/GIXRF](#) model (see [Sub-chapter III.C](#) on page 79).

II EXPERIMENTAL

II.A-3.1 ID21 beamline overview

The [ESRF](#) machine operates at an electron energy of 6 GeV and a maximum current of 200 mA. At the beamline ID21 monoenergetic photon beams with energies ranging from about 2 keV up to about 7.5 keV can be delivered to the users. Three different [Insertion Device \(ID\)](#) can be used for the production of the primary photon beam, namely a linear undulator, a helical undulator and a linear wiggler. They are installed on a 4.8 m long low beta straight section of the storage ring. The horizontal and vertical [FWHM](#) sizes of the photon source are 47 mm and 12 mm, respectively. The horizontal and vertical source divergences amount respectively to 82 mrad and 12 mrad at 7 keV and 85 mrad and 20 mrad at 2 keV.

Through the primary slits (aperture of $5 \times 12 \text{ mm}^2$) the white beam produced by the insertion devices enters the lead shielded hutch and reaches the double mirror system used for the rejection of the higher energy photons resulting from the [ID](#) upper harmonics. Mirrors with Rh, Si and Ni coatings are available. The incident cut-off angle can be tuned from 5 mrad to 20 mrad. Downstream from the mirror system, lead shielding is no more necessary, the energy of the so-called pink beam being sufficiently low.



<http://www.esrf.eu/UsersAndScience/Experiments/Imaging/ID21/Sxm/BeamlineOverview>

Figure II.A.8: Schematic representation of the ID21 beamline elements.

The pink beam passes through a Bremsstrahlung stop and a collimator with a $5 \times 5 \text{ mm}^2$ aperture and enters then into the optics cabin where it is further filtered and cleaned by several pre-focusing x-ray optics elements (beam steering multilayer, focusing mirrors, plane-grating monochromator).

At the entrance of the experimental cabin, a fixed exit double crystal monochromator from Kohzu Precision Co. Ltd is installed which allows energy scans with negligibly small spatial deviations of the beam. The monochromator is equipped either with two Si (111) single crystals for measurements requiring a high energy resolution (relative resolving power of 10^{-4}) or a NiB_4C multilayer optics for experiments requiring rather a high photon flux at a moderate energy resolution (relative resolving power of $10^{-3} - 10^{-2}$).

In order to minimize the absorption of the produced x-rays, the beamline is operated at [UHV](#) upstream from the monochromator and at [HV](#) downstream, which allows a windowless connection of the von Hamos spectrometer to the beamline. For the present measurements no x-ray focusing optics was used and the von Hamos spectrometer was installed downstream from the [Scanning X-ray Microscope \(SXM\)](#) chamber to which it was connected with a 1.8 m long evacuated pipe.

II.A-3.2 MI-975 experiment

The experiment was carried out in early April 2009. The [GEXRF](#) angular profiles of Fe, Cr and MgO nanostructures thermally evaporated on Si substrates (see [Subsection II.C-1.1](#) on page 49) were measured using two different beamline setups:

1. In the first setup, the synchrotron radiation was produced by two undulators mounted in series. Upper-harmonics photons were rejected by means of a Ni coated mirror set at a cut-off angle of 7.5 mrad. The beam energy was tuned to 6.4 keV for the Cr measurements and to 7.2 keV for the Fe measurements by means of a double NiB_4C multilayer monochromator. The resulting intensity on the samples was of the order of $2 \cdot 10^{13}$ photons/s.
2. In the second setup (MgO and bulk Si measurements), an undulator was used and the upper-harmonics were suppressed with a Si coated mirror operated at a cut-off angle of 7.5 mrad. The beam energy was tuned to 2.3 keV and 2.9 keV, using the same multilayer monochromator as in the first setup. In this case, the beam intensity on the sample was about $3 \cdot 10^{12}$ photons/s.

In order to reduce the wings of the spatial beam distribution a $1.5 \times 1.6 \text{ mm}^2$ pin-hole was installed in the [SXM](#) chamber. The [GEXRF](#) angular profiles were determined, using the $K\alpha$ x-ray lines of Fe, Cr, Si and Mg. For the Fe and Cr measurements, the von

II EXPERIMENTAL

Hamos spectrometer was equipped with a Ge (220) crystal, whereas for the MgO ones a TiAP (001) crystal was employed and the measurements were performed in second order of diffraction. For the calibration of the angular scale, the angular profile of the Si wafer of each sample was also measured, using an ADP (101) crystal.

II.A-3.3 MI-1108 experiment

During this experiment which took place in late November 2011, the [GEXRF](#) angular profiles of periodic nanostructures of chromium deposited on Si wafers were measured. Samples with different patterns (stripes, trapezoidal prisms, disks) were investigated (see Subsections [II.C-2.2](#), [II.C-2.3](#) and [II.C-2.4](#)).

The beamline setup was similar to the one used in the first part of the experiment MI-975 (two undulators in series, Ni coated mirror, NiB_4C multilayer monochromator) but, the beam energy was tuned to 6.48 keV and, instead of a pinhole, two slits with adjustable widths and perpendicular to each other were used to define the beam size. The latter varied between $0.05 \times 0.2 \text{ mm}^2$ and $1.2 \times 1.2 \text{ mm}^2$. For the biggest beam size, the intensity on the sample was $2.8 \cdot 10^{13}$ photons/s.

The [GEXRF](#) angular spectra of the periodic pattern samples were measured using the $\text{K}\alpha$ x-ray line of Cr. As in the previous experiment, for each sample the calibration of the angular scale was determined from the [GEXRF](#) angular profile of the corresponding Si wafer, using the Si $\text{K}\alpha$ x-ray line. For all measurements the von Hamos spectrometer was equipped with a SiO_2 ($\bar{1}\bar{1}0$) crystal, the Si $\text{K}\alpha$ x-ray line being observed in first order of diffraction, the $\text{K}\alpha$ x-ray line of Cr in second order.

II.A-4 SLS measurements

Our last experiment was carried out in mid March 2012 at the [SLS](#) SuperXAS beamline, in Villigen, Switzerland.

The [SLS](#) synchrotron facility is operated at an electron energy of 2.4 GeV and a current of 400 mA with a so-called top-up electron injection. In this mode the booster injects periodically electrons into the storage ring, keeping the intensity of the circulating electron beam constant. The top-up injection together with very small beam intensity losses ensures synchrotron radiation beams that are very stable in intensity and position.

II.A-4.1 SuperXAS beamline overview

SuperXAS is a beamline based on a 2.9 T bending magnet having a critical energy of 11.1 keV. The photon energy range available at the beamline spans from ~ 4.5 keV to

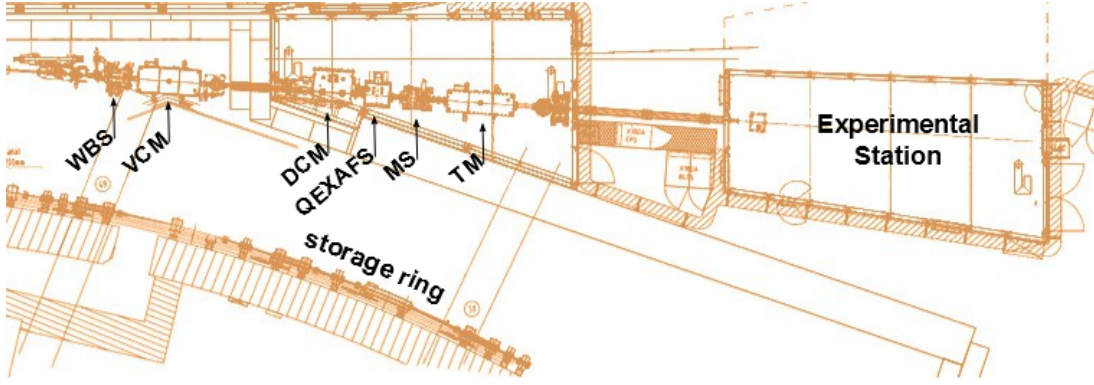


Figure II.A.9: Top view on the SuperXAS beamline: WBS – white beam slits, VCM – vertical collimating mirror, DCM – double crystal monochromator, QEXAFS – quick EXAFS monochromator, MS – monochromatic slits, TM – Toroidal Mirror.

~ 35 keV. The horizontal and vertical [FWHM](#) sizes of the photon source are $53\ \mu\text{m}$ and $16\ \mu\text{m}$, respectively, with divergences of 2 mrad in the vertical plane and 0.6 mrad in the horizontal one.

A schematic view of the superXAS beamline is presented in [Figure II.A.9](#). As shown, the synchrotron radiation produced by the bending magnet passes first through a graphite attenuator and a slit system (WBS) which define the intensity and dimensions of the so-called white beam. The latter is collimated in the vertical plane by a water cooled mirror (VCM) and monochromatized either by a double crystal monochromator (DCM) or, for fast scanning operation, by the [quick EXAFS \(QEXAFS\)](#) monochromator [47]. The Bremsstrahlung stopper serves to block the white and pink beams, while the secondary slits (MS) block the scattered beam and define the dimensions of the monochromatic beam which can be focused on the samples by means of a toroidal mirror (TM).

The substrates of the VCM and TM mirrors consist of 1100 mm long and 40 mm thick monocrystalline Si wafers which are 80 mm (VCM) and 70 mm (TM) wide. The optical active surfaces are made of Rh and Pt coatings with a Cr underlayer. In the case of the VCM mirror there is in addition a bare Si stripe between the Rh and Pt coatings. The Rh and Pt coatings and Si central stripe of the first mirror are 20 mm wide, while the width of the two coatings of the toroidal mirror amounts to 34 mm. The VCM mirror is bent cylindrically (radius of curvature adjustable from 4.5 km to 40 km) and the TM one is bent toroidally (bending radius from 3 km to 40 km). The mirror holders/benders are supported by massive granite blocks that are mechanically isolated from the vacuum chamber by means of edge-welded bellows. The mirrors can be remotely adjusted in five independent degrees of freedom (three rotations and two translations). The two translation stages allow to move the mirrors horizontally and

II EXPERIMENTAL

thus to change the coating between Pt and Rh (plus Si coating in the case of the VCM mirror).

The double crystal monochromator (DCM) consists of two Si (111) or Si (311) single crystals. The Si (111) crystals set is employed for the lower energy range (down to 4.5 keV) and the Si (311) one for the higher energies (up to 35 keV). The dimensions of the first crystal are $40 \times 70 \times 10 \text{ mm}^3$ and those of the second one $40 \times 170 \times 30 \text{ mm}^3$ (width \times length \times thickness). The exchange between the Si (111) and Si (311) crystal pairs can be done in vacuum by means of a remote-controlled linear stage. In order to withstand the thermal heat load the crystals are water cooled. The QEXAFS monochromator consists of a goniometer which permits to select a specific Bragg angle and a fast oscillating channel cut crystal attached to the goniometer. The oscillation of the monochromator crystal is produced by an eccentric disk that is continuously rotated by a motor. This system permits to scan up to ~ 40 energy points per second. Depending on the energy, a Si (111) or Si (311) crystal is used. The two crystals can be manually exchanged during shutdown periods.

Different components and detectors allowing setting up transmission and fluorescence experiments as well as Resonant Inelastic X-ray Scattering (RIXS) and High Energy Resolution Fluorescence Detected X-Ray Absorption Spectroscopy (HERFD XAS) measurements can be installed in the experimental station. A sample manipulator consisting of several modules including horizontal and vertical movements plus a rotation is also available. The components corresponding to the different setups can be easily exchanged or removed.

II.A-4.2 Experiment

The von Hamos crystal spectrometer of Fribourg was installed in the experimental station downstream from the optical tables (see Figure II.A.10). For our experiment all unnecessary parts of the beamline equipment were removed from the beam path and replaced by a bare beam pipe closed at the spectrometer side by a Kapton window. To simplify the venting of the spectrometer, the beam port of the latter was not connected mechanically to the beam pipe but closed with a thin Kapton foil. The distance between the beam port and the downstream end of the beam pipe amounted to a few cm only, resulting in a negligibly small absorption of the incoming photons in air.

The beam energy was tuned to 8.5 keV, using the DCM monochromator and the Rh coating for both mirrors. In order to reduce the wings of the spatial beam distribution and to preserve the angular resolution of the GEXRF measurements (see Subsection III.B-5.2 on page 76) a height of 0.5 mm was adopted for the horizontal monochromatic slit, whereas the width of the vertical slit was varied between 0.2 and 3.5 mm, depending on the measured sample. For the widest beam the intensity on the sample was $\sim 7 \cdot 10^{11}$ photons/s.

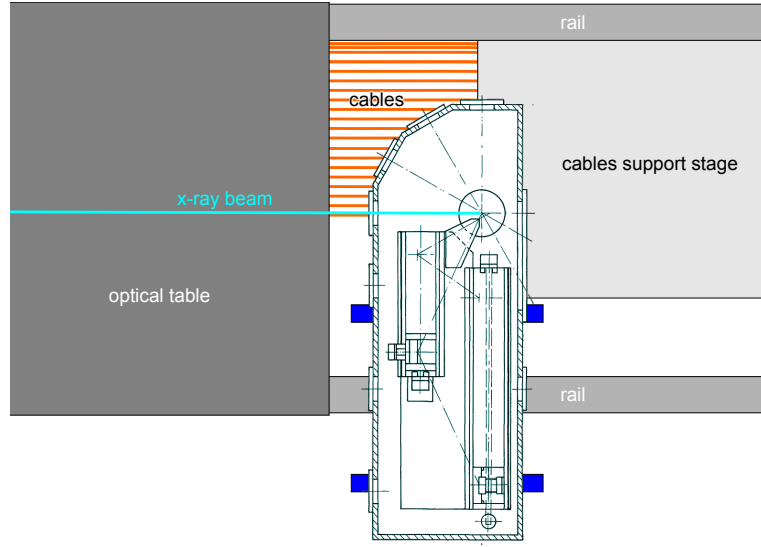


Figure II.A.10: Schematic drawing of the von Hamos spectrometer as installed at the [SLS](#) SuperXAS beamline.

Several structures with plane symmetries were measured (see subsection [II.C-2.4](#) and [II.C-2.5](#)). The [GEXRF](#) angular profiles were measured using the $K\alpha$ x-ray lines of Si, Co and Ni. The spectrometer was equipped with a Ge (220) crystal for the measurements of Ni and with a SiO_2 ($\bar{1}\bar{1}1$) crystal for those of Si. The Co measurements were performed partly with the Ge (220) crystal in first order of diffraction and partly with the SiO_2 ($\bar{1}\bar{1}1$) crystal in second order of diffraction.

II.B GIXRF measurements

II.B-1 Beamlines

The experimental GIXRF data were collected by Falk Reinhardt from [Physikalisch-Technische Bundesanstalt \(PTB\)](#) at two different beamlines of the electron storage ring BESSY II, in Berlin, Germany. The measurements in the soft x-ray range, *i.e.* the energy regime between 78 eV and 1860 eV, were performed at the [Plane Grating Monochromator \(PGM\)](#) beamline [48]. The measurements demanding a higher excitation energy were realized at the [Four-Crystal Monochromator \(FCM\)](#) beamline [49, 50], where x-ray energies between 1.75 keV and 10.5 keV are available. At both beamlines the incident synchrotron radiation is well characterized in terms of spectral purity and intensity profile in the focal plane.

II.B-1.1 Plane grating monochromator beamline

The PGM beamline is operated with two undulators characterized by periods of 180 mm and 49 mm, respectively. The undulators provide photons with energies ranging from 20 eV to 1900 eV with a high flux and a small transmittance of higher diffraction orders. The radiation impinging on the monochromator originates from the central cones of the first, third and fifth undulator harmonics.

The layout of the whole beamline is shown in [Figure II.B.1](#). The first optical element is a horizontally deflecting water-cooled toroidal mirror (M_1) which collimates the light in both the vertical and horizontal directions. The collimated beam passes through the plane-grating/plane-mirror assembly (M_2 , PG), equipped with two gratings (1200 and 300 lines/mm) and a long rotatable plane mirror. All optical elements are Au-coated except the plane mirror and the 300 lines/mm grating whose surfaces are divided into two halves which are coated one with SiC, the other one with Au. The 300 lines/mm grating and the plane mirror can be translated transversely to the optical axis. As a result, depending on the photon energy, a different coating can be used for an optimum suppression of the photons corresponding to higher-order diffractions. A horizontally

II EXPERIMENTAL

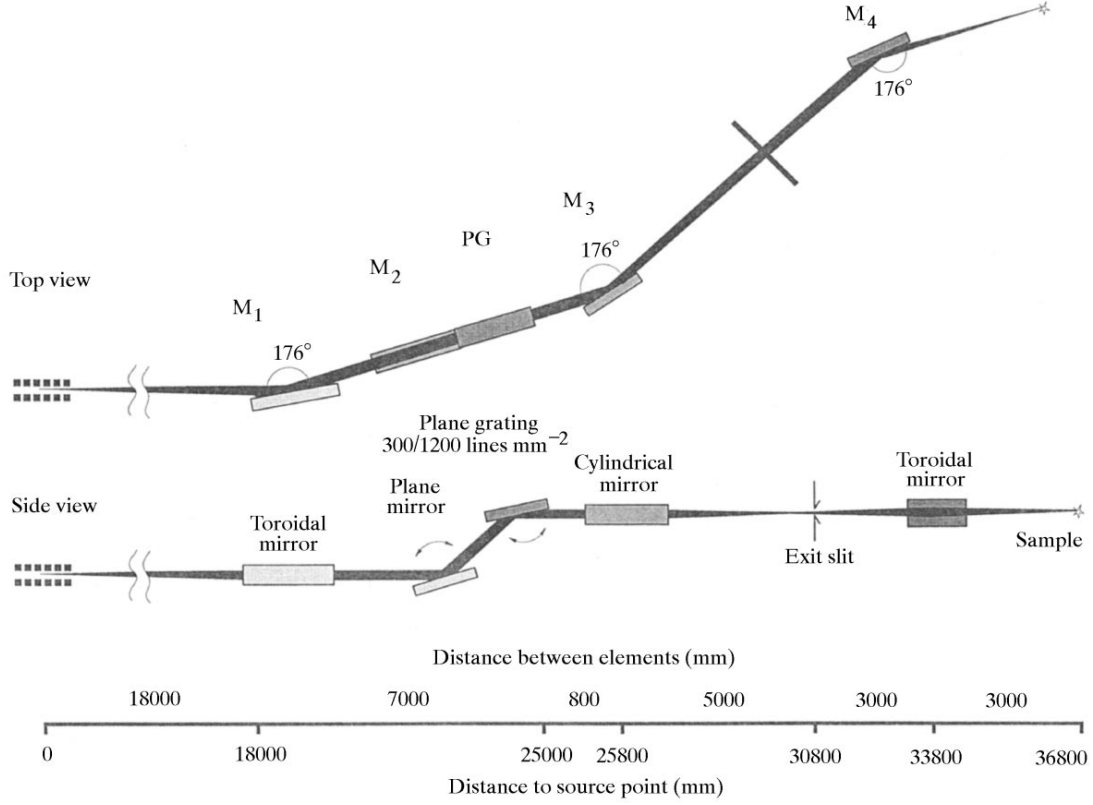


Figure II.B.1: Schematic view of the plane-grating monochromator beamline (from [48]).

deflecting cylindrical mirror (M₃) focuses the diffracted light vertically onto the exit slit. Finally the beam is refocused in both the vertical and horizontal directions at the toroidal mirror (M₄).

An advantage of this beamline is the possibility to downsize the vertical spread of the beam profile down to 20 μm .

II.B-1.2 Four-crystal monochromator beamline

The FCM beamline is fed with the radiation from a bending magnet having a characteristic energy of 2.5 keV. The beamline covers the energy range from 1.75 to 10 keV. In order to achieve the required reproducibility in photon energy, the monochromator and focusing elements are decoupled.

The beamline layout is presented in Figure II.B.2. The beam produced by the bending magnet is first reflected by a toroidal mirror. The latter focuses the beam in the horizontal plane and collimates it in the vertical plane. A four-crystal geometry is used to monochromatize the beam, employing the setup proposed by DuMond [51] which provides a fixed exit beam without crystal translations (see Figure II.B.3). To

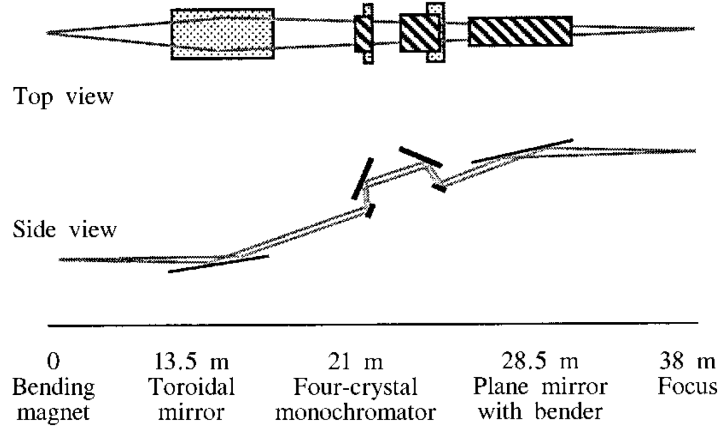


Figure II.B.2: Schematic view of the four-crystal monochromator beamline (from [49]).

cover the spectral range from 1.75 to 10 keV, two sets of four InSb (111) and Si (111) crystals are used. The two sets can be exchanged in vacuum by means of a horizontal translation. The monochromatized beam is then reflected by a quasi-flat mirror that can be bent down to a radius of 2 km to superpose the vertical and horizontal focal points. The beam at the FCM beamline can be vertically focused down to 300 μm .

II.B-2 GIXRF setup

II.B-2.1 Ultra-high vacuum x-ray spectrometry chamber

In order to perform the GIXRF measurements the samples need to be properly mounted and manipulated. To achieve this aim, a dedicated UHV x-ray spectrometry chamber was developed at the PTB. The latter allows to perform measurements in standard x-ray fluorescence conditions as well as in the GIXRF geometry [52, 53]. The GIXRF spectra of the samples consisting of NaCl nanostructures (Subsection II.C-1.2 on page 51) and Cr pads (Subsection II.C-2.1 on page 52) were measured using this PTB's x-ray spectrometry chamber.

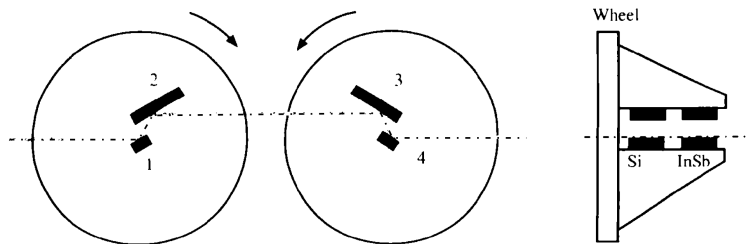


Figure II.B.3: Schematic view of the four-crystal monochromator (from [49]).

II EXPERIMENTAL

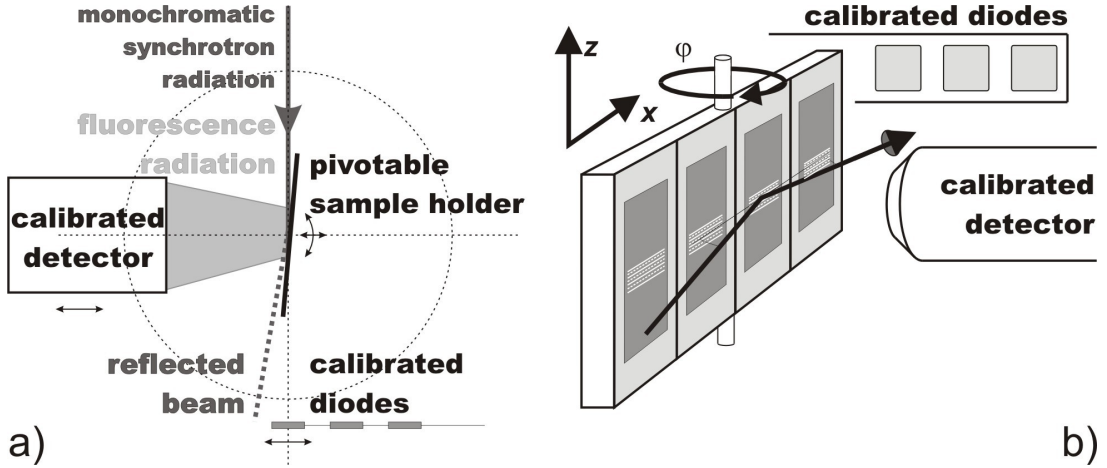


Figure II.B.4: Sketch of the PTB's GIXRF experimental setup: a) top view, b) view from the upstream side. The energy-dispersive SDD detector is aligned perpendicularly to the incident beam. This permits to minimize the intensity of the scattered radiation. The figure was taken from [54].

The sample fluorescence is produced by a monochromatic synchrotron radiation of well-known flux and intensity distribution in the focal plane. The intensity of the incident radiation is measured with a set of calibrated photodiodes. The latter are also used to determine the incident angle of the beam with respect to the sample surface (see Figure II.B.4). Thanks to a precise knowledge of the chamber geometry, the incident angle can be set with a precision of $\pm 0.005^\circ$. Together with the known beam profile, this ensures the accurate determination of the effective solid angle of detection for any incident angle and photon energy [53].

As the x-ray spectrometry chamber is equipped with a single rotation axis, a great care was devoted to the mounting of the Cr pads sample on the target holder: the rows in which the pads are arranged were accurately aligned on the direction corresponding to the spread of the beam footprint on the sample surface (see Figure II.B.4.b).

II.B-2.2 6-axis manipulator ultra-high vacuum chamber

The Cr stripes sample (Subsection II.C-2.2 on page 52) was mounted on the UHV 6-axis manipulator developed recently at the PTB [55]. The latter consists of a x - y - z -translation stage and a ϑ - χ - φ -rotation stage. Here χ denotes the angle of the sample surface with respect to the polarization plane of the incident synchrotron beam. Thus, for $\chi = 0^\circ$, measurements of s -polarized photons are possible, whereas measurements performed at $\chi = 90^\circ$ allow to minimize the scattering of the radiation in the sample. For $\chi = 90^\circ$, φ corresponds to the angle of the incident beam relatively to the substrate surface. This angle can be varied from 0° to 45° , enabling GIXRF and TXRF measurements as well as conventional XRF measurements in the standard $45^\circ/45^\circ$ -setup. The ϑ -stage rotates the sample around an axis which is normal to the sample surface.

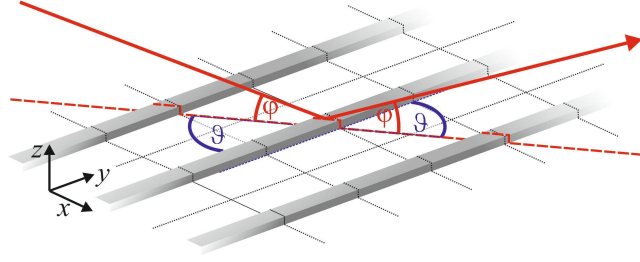


Figure II.B.5: Sample layout in the 6-axis manipulator chamber. The Cr stripes are parallel to the y -axis and lie in the x - y -plane. φ represents the angle between the incident radiation and the x - y -plane, whereas ϑ denotes the tilt angle between the y -axis and the projection of the incident beam on the x - y -plane.

For the measurements, the sample was aligned so that the center of the stripes structure coincided with the φ and ϑ rotation centers. Then the angle ϑ was varied from slightly below 0° to slightly above 90° in steps of 5° . At each ϑ -angle the XRF count rate was recorded with an SDD detector, varying the incident angle φ from 0° to 1.2° with a step width of 0.01° . The sample layout is presented in Figure II.B.5.

II.B-3 Reference-free analysis

As mentioned above, at both PTB beamlines the incident synchrotron radiation is well characterized in terms of spectral purity and intensity profile in the focal plane. Thus the projection of the beam onto the sample surface, the so-called footprint of the beam (see Figure II.B.6), can be precisely calculated. The fluorescence radiation emitted by the sample is measured with a SDD detector with a well characterized efficiency and spectral response function. Furthermore, for any incident angle the solid angle

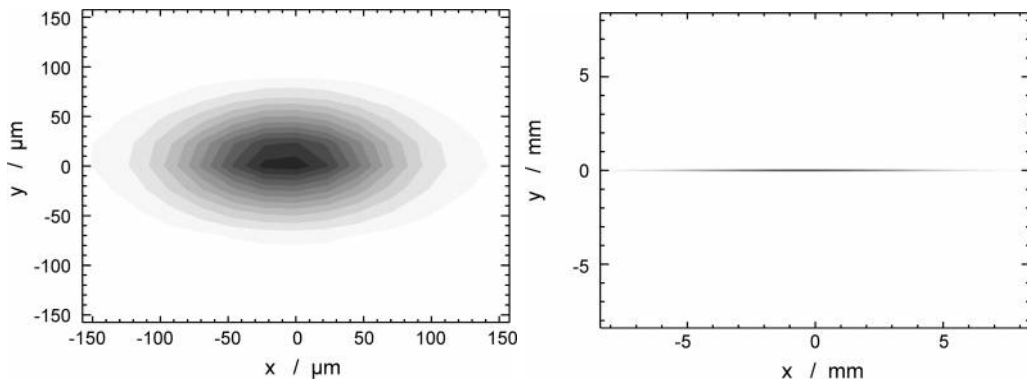


Figure II.B.6: Left: beam spot profile in the focal plane of the PGM beamline for an exit slit width of $70\ \mu\text{m}$. Right: beam spot profile projected on the wafer surface for an incident angle of 0.9° . Both profiles were taken from Ref. [52].

II EXPERIMENTAL

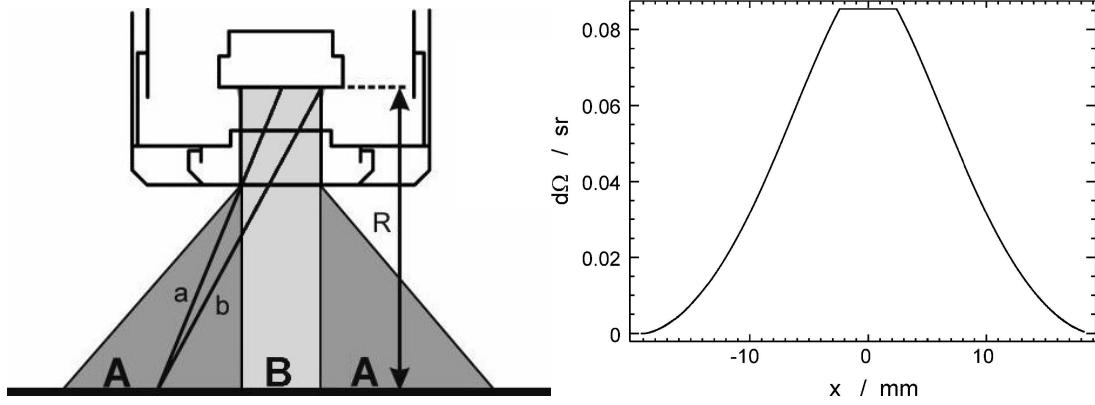


Figure II.B.7: Left: Illustration of the solid angle acceptance. The detector is placed at the distance R from the sample surface. The dimensions of the effective detection area is defined by a collimator placed in front of the detector. As shown, the fluorescence radiation from any point belonging to the region A of the sample surface is viewed only by a part of the detector surface (a and b denote the position-dependent distances between the considered point on the sample surface and the detector), whereas the radiation from points belonging to the region B can be seen by the whole detector surface.

Right: Solid angle acceptance function (lateral contribution) of the detector to be convoluted with the beam intensity distribution on the wafer surface.

Both figures were taken from [52].

acceptance of the detector is known (see Figure II.B.7). Thus, the effective solid angle of detection can be calculated from the convolution of the beam footprint on the sample surface with the solid angle acceptance of the detector.

With this precise knowledge of the effective solid angle of detection [53] and with the use of tabulated or measured fundamental parameters for the relevant atomic processes, *e.g.*, the photoionization cross sections and the fluorescence yields of the elements of interest, a reference-free quantification approach can be applied [52, 53]. However, for particulate media additional geometrical effects need to be taken into account [54]. This problem will be discussed in more detail in Sub-chapter III.D on page 87.

II.C Samples

For the realization of the project, several sets of dedicated samples with different surface nanostructures were fabricated. Most structures were made of transition metals (Cr, Fe, Ni, and Co). Other structures made of low-Z elements like Al or light element compounds such as MgO and NaCl were also prepared. In order to get good total reflection properties, substrate materials with low refractive indexes were preferably chosen, namely silicon, silica and sapphire.

It can be noted that for [GEXRF](#) measurements *3d* transition metals present advantageous properties. First, their refraction index is significantly different from the one of the chosen substrate materials. Secondly, their self absorption for the K-shell fluorescence lines employed for the measurements of the [GEXRF](#) and [GIXRF](#) angular profiles is relatively small.

The investigated samples can be divided into two groups:

- samples with evenly distributed structures ([Section II.C-1](#)) and
- samples with periodic structures ([Section II.C-2](#) on page 52).

The first group of samples was used mainly to investigate the general dependences of the [GEXRF](#) and [GIXRF](#) angular profiles on the surface particle distributions, whereas the samples belonging to the second group were employed to probe the geometrical model developed to interpret the [GEXRF](#) and [GIXRF](#) results.

II.C-1 Evenly distributed structures

II.C-1.1 Fe, Cr and MgO thermal evaporated structures

Most of these samples were fabricated by the Group of Magnetic Heterostructures at the Institute of Physics of the Polish Academy of Sciences in Warsaw, Poland, using the [Molecular Beam Epitaxy \(MBE\)](#) technique. As substrates Si (111) wafers with a native oxide layer of ~ 3 nm were used. The wafers were treated by organic solvents to remove

II EXPERIMENTAL

residual greases. For each deposition material four samples were fabricated which differ by the deposition rate and the structure growth conditions (see [Table II.C.1](#)).

sample number	cap material	growth temp.	annealing temp.	cap thickness	rms roughness
921A	MgO	25 °C	800 °C	1 nm	0.25 nm
921B	Cr				0.37 nm
921C	Fe				0.82 nm
922A	MgO	25 °C	800 °C	5 nm	0.21 nm
922B	Cr				4.07 nm
922C	Fe				5.91 nm
923A	MgO	800 °C	—	5 nm	0.11 nm
923B	Cr				0.55 nm
923C	Fe				3.42 nm
926A	MgO	25 °C	—	5 nm	0.21 nm
926B	Cr				0.26 nm
926C	Fe				0.31 nm

Table II.C.1: Samples fabricated by the Group of Magnetic Heterostructures at the Institute of Physics of the Polish Academy of Sciences. Cap thicknesses are nominal thicknesses derived from the deposition times. The [rms](#) surface roughnesses were determined from [AFM](#) measurements.

Additionally several Cr structures were made by means of thermal evaporation in the Surface Physics and Tunneling Spectroscopy Laboratory at the Institute of Molecular Physics of the Polish Academy of Sciences in Poznań, Poland ([Table II.C.2](#)).

sample number	cap material	growth temp.	cap thickness	rms roughness
5.2.2009 Cr30s	Cr	25 °C	5.7 nm	1.2 nm*
3.2.2009 Cr60s			11.5 nm	9.3 nm*
9.2.2009 Cr90s			17.2 nm	0.7 nm [†]
4.2.2009 Cr120s			22.9 nm	—

*Measured at the Physics Department of the University of Fribourg (Dr. Ivan Marozau).

[†]Measured at the Institute of Molecular Physics of the Polish Academy of Sciences (Surface Physics and Tunneling Spectroscopy group).

Table II.C.2: Samples fabricated in the Surface Physics and Tunneling Spectroscopy Laboratory at the Institute of Molecular Physics of the Polish Academy of Sciences. Cap thicknesses are nominal thicknesses derived from the deposition times.

As shown in [\[56, 57\]](#), for Fe deposited on pure Si (111) at temperatures up to 400 °C, a two-dimensional growth of iron silicide takes place, whereas upon annealing at temperatures higher than 500 °C, three-dimensional nanocrystallites with a CsCl-type metallic structure are formed. Iron does not diffuse into the Si bulk and the whole

amount of deposited material forms iron silicide crystallites. It can be noted that for higher amounts of deposited Fe the semiconducting β phase should be considered, too.

In our case the situation is slightly different since the oxide was not removed from the wafers' surface. Actually, although the removal of oxide takes place at *ca.* 700 °C, built-in oxygen atoms might still be present in the structure even for a deposition temperature of 800 °C. Nevertheless strong topographic similarities were found between the structure of the samples investigated in the present work and those discussed in [56, 57].

Regarding Cr, equilibrium diagrams suggest that its behaviour should be very similar to the one of Fe. The similarity is indeed confirmed by AFM measurements.

In the case of MgO growth on Si (111) the deposited material smoothly covers the Si surface regardless of the growth conditions.

II.C-1.2 NaCl nanostructures

NaCl nanoparticles were deposited on Si surfaces by means of the electrostatic aerosol sampling method. SEM pictures reveal that the NaCl nanoparticles form monodisperse single crystals of similar size (see Figure II.C.1). The nanoparticles' dimensions and their distribution densities are listed in Table II.C.3.

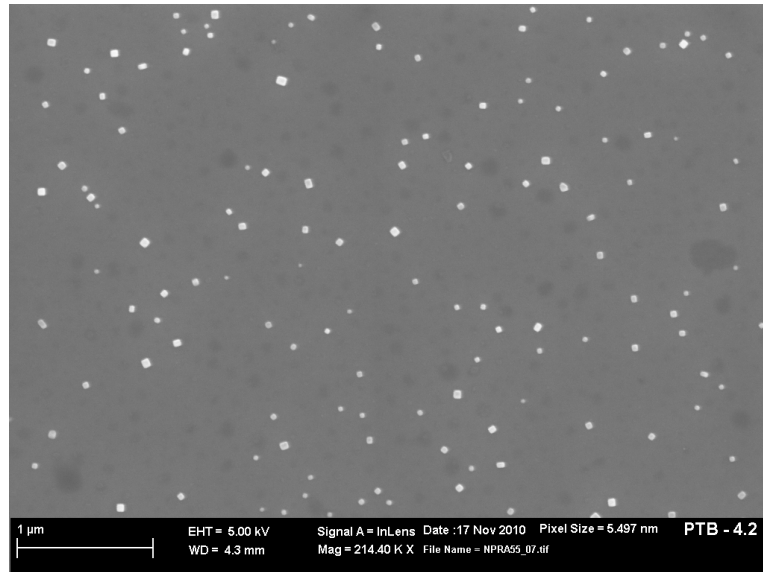


Figure II.C.1: SEM image of NaCl structures (NPR0055 sample).

II EXPERIMENTAL

sample number	av. particle dimension [nm]	particle density [particle/mm ²]
NPRA0053	100	200000
NPRA0054	50	1500000
NPRA0055	20	25000000

Table II.C.3: NaCl structures.

II.C-2 Periodic structures

II.C-2.1 Cr pads

The samples were produced by a lift-off procedure. A pattern of 2250 circular holes with a diameter of $2.7\text{ }\mu\text{m}$, arranged along 7 lines on the surface of a SiO_2 wafer, was imprinted on a photoresist by electron beam lithography. The whole surface was then covered with a chromium layer. After removal of the photoresist, Cr cylinders remained on the substrate in the same arrangement as the original hole pattern. The minimal distance between two neighbouring cylinders was $50\text{ }\mu\text{m}$. Thus, only about 0.2 % of the SiO_2 surface was covered with chromium. Samples with 20 nm, 50 nm and 100 nm high Cr pads were produced.

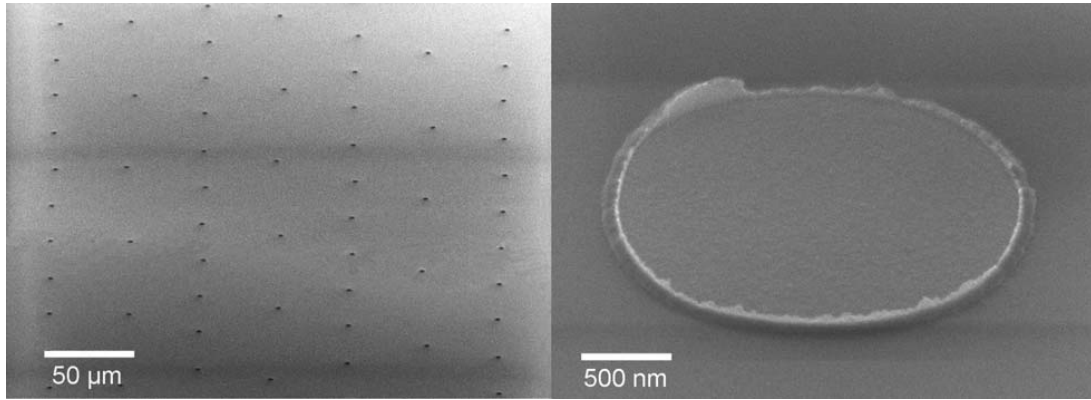


Figure II.C.2: SEM image of a Cr pads sample (left panel) with an enlarged view of a single pad (right panel). (From [54].)

II.C-2.2 Cr stripes

The sample was prepared using the same lift-off technique on a Si wafer having a native oxide layer of $\sim 3\text{ nm}$. A pattern of 1000 stripes having a length of 6 mm and a width of $1\text{ }\mu\text{m}$ and separated by a distance of $5\text{ }\mu\text{m}$ was imprinted on the photoresist. The latter was then covered with a thin chromium layer. After removal of the photoresist 10 nm high Cr stripes remained on the sample surface.

II.C-2.3 Cr trapezoidal prisms

The samples were prepared at the [École Polytechnique Fédérale de Lausanne \(EPFL\) Center of MicroNanoTechnology \(CMI\)](#), in Lausanne. A 10 cm in-diameter Si (100) wafer was used as common substrate for all samples. The wafer was first cleaned using a O_2 plasma and a Piranha solvent¹. Secondly, a chromium layer was deposited on the wafer by means of thermal evaporation at room temperature. The layer was then coated with a photoresist and the pattern of juxtaposed trapezoidal prisms was imprinted by a PC-controlled high-resolution laser beam. After development of the photoresist a wet etched Cr layer was obtained. Finally, the remaining photoresist was removed and the wafer was diced into different pieces corresponding each to a different sample.

For each sample, the pattern consisted of identical trapezoidal prisms having a length of 2 mm and widths varying from 2 μm to 10 μm (see [Figure II.C.3](#)). Samples corresponding to groups of 1, 2, 3, 4 and 5 prisms were prepared. The distance between the prisms in the same group was 12 μm and two adjacent groups were separated by a distance corresponding to 5 prisms, *i.e.*, 62 μm . A sample with a single group of 500 prisms was also produced.

The samples were fabricated from two wafers with Cr layer thicknesses of 6 nm and 10.7 nm, respectively.

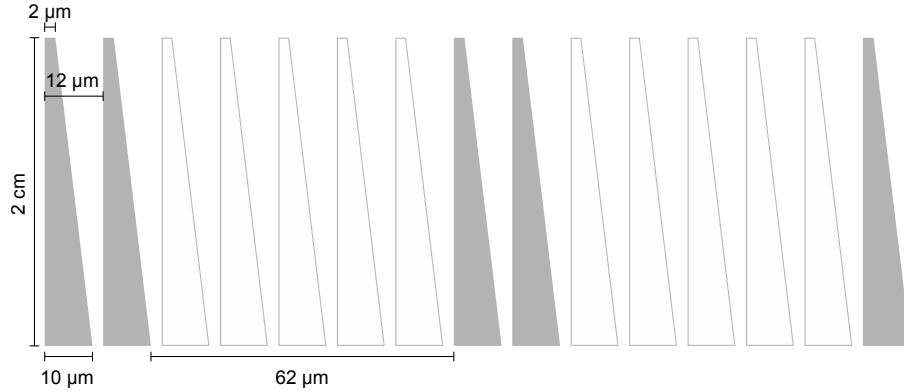


Figure II.C.3: Schematic drawing of a Cr sample with periodic trapezoidal structures.

II.C-2.4 Disk patterns made of one and two superposed 3d elements

The samples were prepared by Andreea Veronica Savu at the [Laboratory of Microsystems 2 \(LMIS2\)](#) of [EPFL](#), using the so-called stencil lithography method which is a high

¹mixture of sulfuric acid H_2SO_4 and hydrogen peroxide H_2O_2

II EXPERIMENTAL

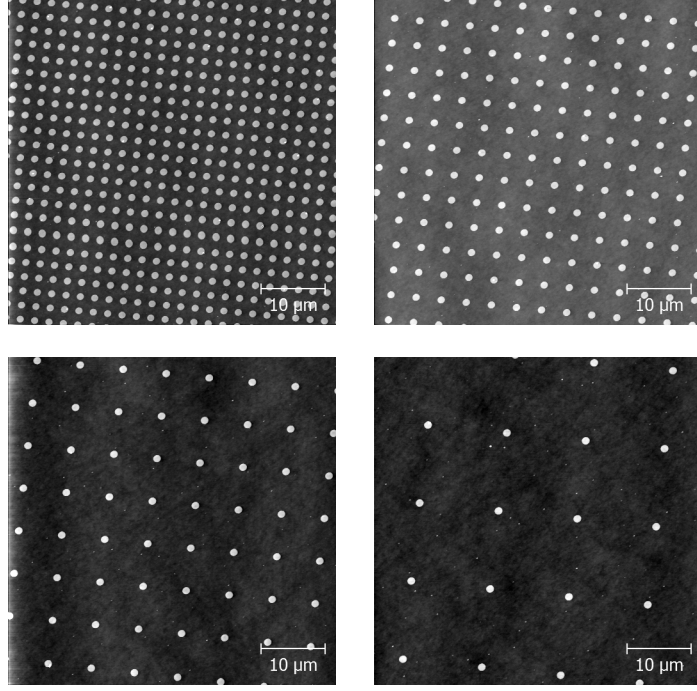


Figure II.C.4: [AFM](#) images of Cr disc patterns prepared with the stencil method.

resolution shadow-mask technique. The latter is usually employed for structuring surfaces at the micro and nanometer scales. A stencil, *i.e.*, a membrane with customized apertures, is clamped to a substrate. The clamped set is placed in an evaporator and the chosen material is deposited through the stencil's apertures onto the substrate. More details about this technique can be found in [58].

Stencils with four $800 \times 800 \mu\text{m}^2$ membranes were used. Circular holes with a diameter of $1 - 2 \mu\text{m}$ were drilled in the membranes to form p4m symmetry [59] periodic patterns with a different hole spacing for each membrane (see [Figure II.C.4](#)). For the present project the stencil membranes were placed on a SiO_2 substrate. Two types of disc structures were prepared. The first one was made by depositing on the substrate a 5 nm thick mono-layer of Cr. For the second one, Co and Ni layers having each a thickness of 3 nm were deposited to build patterns of disks made of Co superposed to Ni. [AFM](#) measurements showed that the [rms](#) roughness of these samples was in the order of 0.5 nm.

II.C-2.5 Samples with plane symmetries

The samples were prepared at the [EPFL CMI](#), in Lausanne, within an user process flow project. The steps of the process flow are presented in [Table II.C.4](#).

As a common substrate for all samples a 10 cm in-diameter Si (100) wafer was used. The designed structures consisted of 5 nm high and $2 \mu\text{m}$ in-diameter disks distributed


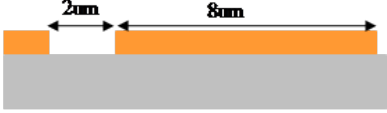


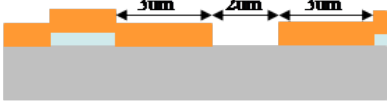




Step	Process description	Cross-section after process
0.	Substrate cleaning	
1.	Photoresist coating and photolithography	
2.	First metal evaporation	
3.	Lift-off resist removal	
4.	Photoresist coating and photolithography	
5.	Second metal evaporation	
6.	Lift-off resist removal	
7.	Protective coating before dicing	
8.	Dicing	

Table II.C.4: Process flow steps for the structuration of the plane symmetry samples.

II EXPERIMENTAL

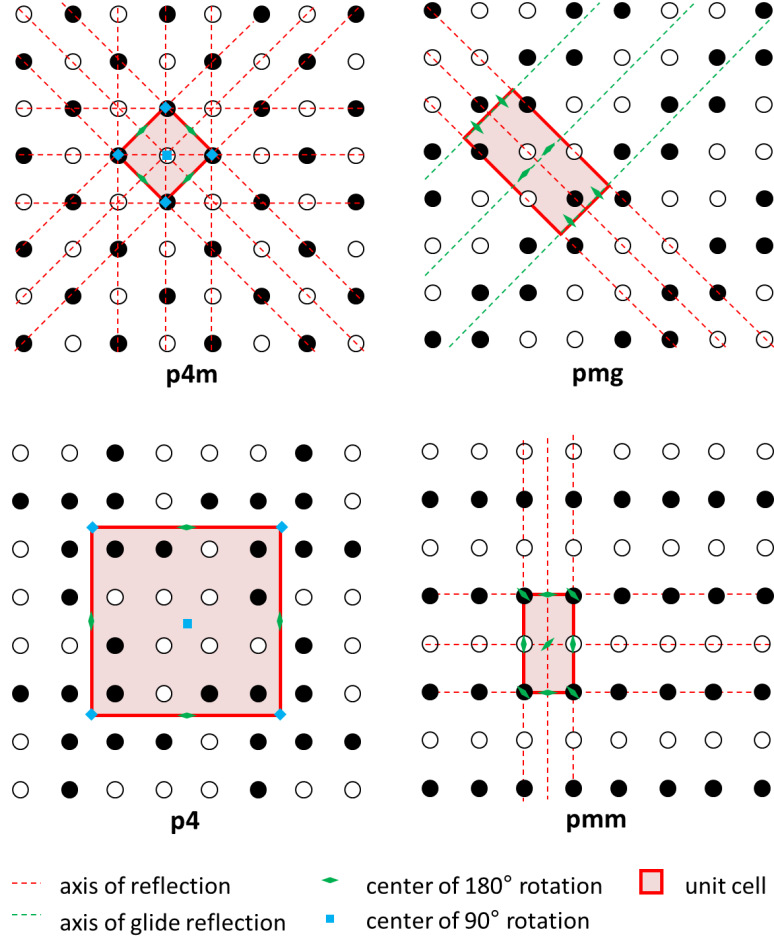


Figure II.C.5: Different plane symmetries (p4m, pmg, p4, pmm) [59] of the Ni/Co patterns.

on the intersection points of a rectangular grid having a $5\ \mu\text{m}$ period. Several patterns with two sorts of disks made of different metals, namely Ni or Co, and characterised by different plane symmetries (see Figure II.C.5) were fabricated. In addition, on the same wafer and within the same process flow, calibration samples consisting of Ni and Co layers were produced. The metallic layers were deposited by means of thermal evaporation. Finally, the wafer was coated with a photoresist layer in order to protect the nanostructures during transportation and storage and the wafer was cut into $1 \times 1\ \text{cm}^2$ dices. For the measurements, the photoresist coating was removed in an acetone bath.

The two-layer layout drawing of the wafer was prepared with a [Computer-Aided Design \(CAD\)](#) software. Each layer was imprinted on a photolithography mask by means of an optical pattern generator based on a Kr laser scanner having a $1\ \mu\text{m}$ resolution. The masks were then used for a direct on-wafer photolithography of the designed struc-

tures. The same masks could be used repeatedly. The masks corresponding to the two layers were aligned by means of an optical device using reference marks printed on each mask. The alignment precision was in the order of $1\ \mu\text{m}$.

Despite of several attempts in which the parameters of the production steps were slightly modified, the 5 nm thick Co layer appeared to be very unstable and systematically deteriorated during the lift-off process. No clear explanation could be found for the layer deterioration and thus no Co-Ni double layer sample of good enough quality could be obtained. Note that such a difficulty was not encountered with the Ni layer.

Chapter III

Data analysis and data processing

III.A CCD events analysis

The analysis of the [CCD](#) images permits to distinguish good x-ray events from background events. The charge deposited in a single [CCD](#) pixel or in a group of neighboring pixels is indeed proportional to the energy of the absorbed photon. Good event pixels can thus be sorted by filtering the data with an energy window. Actually, if the pixel charge fulfills the conditions of the energy window, a 1 is assigned to that pixel, if not a 0. This procedure reduces the number of background events originating from scattered photons, photons diffracted by the crystal in higher orders of diffraction, or cosmic rays. For strong x-ray lines, the energy window can be determined directly from the frequency distribution of the charges deposited in the pixels, whereas for weak x-ray lines, it can be determined from the known linear energy response of the [CCD](#) camera. The latter was indeed determined precisely, using the $K\alpha$ transitions of a variety of elements ranging from Mg ($E=1.254$ keV) to Mo ($E=17.479$ keV) [46].

III.A-1 Currently used algorithm

The filtering algorithm used so far by the [Atomic and X-ray Physics \(AXP\)](#) group of Fribourg was presented in [46]. In the latter article it was shown that for the back illuminated [CCD](#) camera charges are either deposited in a single pixel or split randomly between several neighboring pixels. These two cases are treated differently by the algorithm. In particular different energy windows are used for the two cases, the energy window having to be wider and shifted to higher energies for split events.

Let us shortly describe the algorithm steps:

1. Single events sorting

If the charge deposited in a pixel fits the energy window for single events the corresponding event is cataloged as a good event and a 1 is assigned to this pixel which is excluded from further analysis.

2. Split events sorting

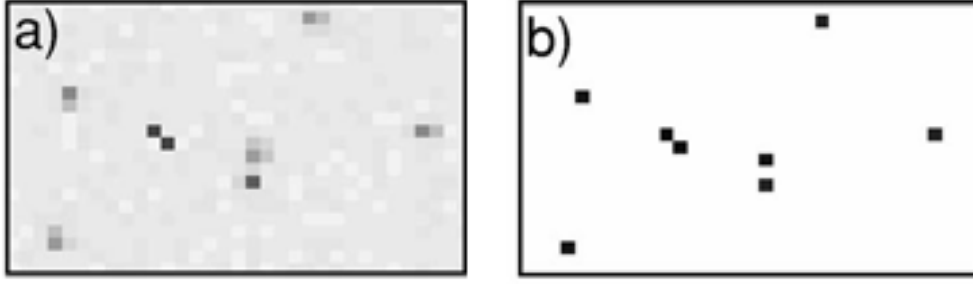


Figure III.A.1: Selected area of a raw (a) and corrected (b) [CCD](#) image. (From Ref. [46].)

(a) Threshold charge

After the sorting of the pixels corresponding to single events the image is reanalyzed and only those pixels that have a charge above a certain threshold value (established experimentally) are considered.

(b) Nearest neighbors sum

For each pixel satisfying the threshold condition, the total charge obtained by summing the charge of this pixel with those of its nearest neighbors is calculated.¹ The pixels taken into consideration for the calculation of the total charge are then excluded from further analysis.

(c) Good events sorting

If the above mentioned total charge fits the energy window for split events, a good event is attributed to the pixel with the highest partial charge in the group and, in the filtered image, a 1 is assigned to this pixel.

An example of image filtering is presented in [Figure III.A.1](#)

The algorithm described above counts all events within the chosen energy window provided that, for split events, pixels are not shared. This is in general true for low charge deposition rates when only few good events are observed for each [CCD](#) image. However, going to high brilliance x-ray radiation sources such as synchrotron light sources, the probability that the above condition is not satisfied might be rather high.

If in the same [CCD](#) image, a pixel is hit more than one time, one observes a so-called **multiple hit event**. Such an event is eliminated by the single event sorting algorithm and two or more good events will be thus lost. The same holds for split events if two or more shared pixels are hit within the same exposure (**split multiple hit event**). As a result many good events could be missing at the end of the filtering process and the

¹It should be noted here that the sum is calculated over 9 pixels and not 4 as stated in [46].

intensity of the measured spectrum might thus be affected by systematic errors. For single pixel events, a possible solution to this multiple hit problem consists to reanalyze the [CCD](#) images using energy windows corresponding to the double and, if necessary, triple value of the energy of the measured x-rays and to assign a 2 or a 3 to these good double or triple hits events. However, such a procedure increases the background by a factor 3 (double hit analysis) or 4 (triple hit analysis) and is hardly applicable to split events.

Therefore we have developed a new algorithm which should satisfy the two following conditions: a correct sorting of the multiple hits for both single and split events and, for small numbers of events, the results should be equal to those obtained with the former algorithm.

III.A-2 New algorithm

In this section the new algorithm that should resolve multiple hit events is presented together with its application limits. The equivalence of the new and old algorithms in the limit of small charge deposition rates is then discussed for split single hit events.

The new algorithm consists of the following steps:

0. Background subtraction (see [Section III.A-4](#) on page 66)

This is not really an algorithm step but rather a part of the data acquisition process. However, the algorithm requires that the average background level is 0.

1. Single pixel threshold charge

The image is scanned to sort pixels having a charge above the preset threshold.

2. Threshold charge for groups of neighboring pixels

For each pixel with a charge above the single pixel threshold, the charge of this pixel is added to the ones of the nearest neighbors.

- If the sum is higher than the lower limit of the energy window for split events, all the pixels belonging to the group are retained for further analysis.
- Otherwise, the central pixel is checked for the condition of a single event window and assigned as a good event if the condition is fulfilled.

3. Multiple hit domains

For each [CCD](#) image, groups of pixels corresponding to split multiple hit events are identified by means of a modified version of the flood filling algorithm. Such groups named hereafter **multiple hit domains** consist of pixels having a charge

above the single pixel threshold and of all neighboring pixels of the latter (see Figure III.A.2). Two domains are non-contiguous if the pixels with a charge above the threshold have pairwise no common neighbors, *i.e.*, the pixels of each pair are separated by at least 3 pixels.

For each multiple hit domain D the sum S_D of the charges of all pixels belonging to the domain is calculated.

4. Hit regions.

Each multiple hit domain is probed for non-contiguous sub-groups of pixels having a charge above the single pixel threshold. Such sub-groups called **hit regions** are composed of the pixels with a charge above the threshold and of all nearest neighbors of the latter. Thus, hit regions inside a multiple hit domain may have some common pixels (see Figure III.A.2).

For each hit region R the sum S_R of the charges of all pixels belonging to the region is calculated.

In order to calculate the charge deposited in a specific hit region S_D is shared between the regions belonging to the same domain according to the following relation:

$$\tilde{S}_R = S_R \cdot \frac{S_D}{\sum_{R' \subset D} S_{R'}}. \quad (\text{III.A.1})$$

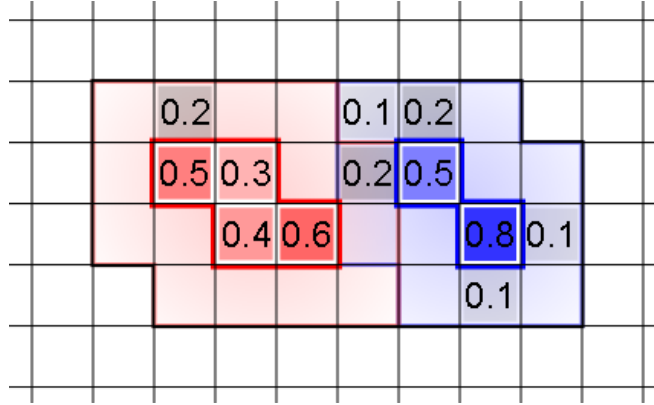


Figure III.A.2: Example of a multiple hit domain consisting of two (red and blue) hit regions. The numbers noted in the pixels correspond to the partial charges deposited in these pixels. Pixels with a charge above the threshold (set here to 0.25) are colored and surrounded with a thick colored line. The charges deposited in the pixels lying in two hit regions is shared equally between the latter; this gives hit regions with partial charges \tilde{S}_R of ~ 2.1 (red) and ~ 1.9 (blue) which would both correspond to good multiple hit events by setting an energy window of 10%. Note that none of the four pixels with the highest partial charges presented in the figure would be recognized as good split events by the previous algorithm since the sum of the charges of the nearest neighbours is much bigger than the charge deposited by a single event.

5. Multiplicity assignment

If \tilde{S}_R fits the energy window corresponding to a multiple hit of multiplicity n then this multiplicity n is assigned to the hit region.

6. Good events assignment

- Hit regions with no multiplicity

If the hit region has no multiplicity then each of the pixels belonging to this region and having a charge above the threshold is probed for the energy windows corresponding to single hit events and multiple hit events. The multiplicities of the applicable energy windows are then assigned to these pixels.

- Single hits

If a multiplicity of 1 is assigned to a hit region then a good event is assigned to the pixel with the highest deposited charge.

- Multiple hits

For split multiple hits the assignment of integer numbers of events to a pixel is troublesome owing to the fact that the charge distribution in a hit region might be very complex. In the new algorithm, an alternative solution is thus proposed which consists of assigning partial multiplicities to all pixels of the hit region having a charge above the threshold. The assigned multiplicity is proportional to the charge deposited in the pixel. The sum of all partial multiplicities assigned to the pixels within a hit region must be equal to the multiplicity of this region.

It should be noted that the distinction between the assignment of good events for single and multiple hits is somewhat artificial and was introduced only on account of compatibility with the previous algorithm.

III.A-3 Energy window

For the proper analysis of the multiple events a suitable definition of the energy window is needed. For single hits the definition is straight forward: depending on whether we check a single pixel or a domain the energy windows are defined as in the previous algorithm for the cases of single and split events, respectively.

The determination of the energy windows for higher multiplicities can be done, similarly to the previous case, experimentally. However, provided that the charge frequency distribution for single events has a Gaussian shape, the energy windows can be also determined theoretically.

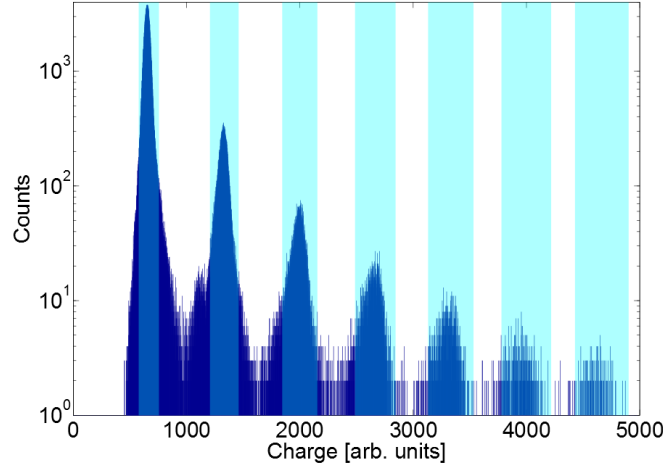


Figure III.A.3: Histogram of the charge distribution in hit regions for a measurement with densely distributed events. The energy windows corresponding to multiple hits are indicated by light blue stripes.

The charge deposited in a multiple hit does indeed correspond to the sum of the charges deposited in separated single events. Therefore the charge frequency distribution of a multiple hit should be a convolution of n charge frequency distributions for single events, *i.e.*, according to the above assumption, a convolution of n Gaussians centered at I_0 and with [HWHM](#) widths δ . Thus, the charge distribution related to a multiple hit should also be a Gaussian centered at $n \cdot I_0$ and with a [HWHM](#) of $\sqrt{n} \cdot \delta$.

Above statements permit to determine the energy windows for multiple hits in a straightforward way from the corresponding single hit energy window. If the single hit energy window is given by the interval $[min, max]$, the energy windows for higher multiplicities can indeed be written simply as:

$$n \cdot \frac{max+min}{2} + \sqrt{n} \cdot \frac{max-min}{2} \cdot [-1, 1] \quad (\text{III.A.2})$$

Again, depending on whether we check a single event pixel or a multiple hit domain, the intervals $[min, max]$ should correspond to the single hit energy windows for single and split events, respectively.

III.A-4 Background consideration

As already mentioned, the algorithm requires that the background mean value is 0. If it is not the case the sum of the pixel charges in a domain depends on the size of the latter. This results for each multiplicity in a broadening and a shift of the charge frequency distribution and thus also of the corresponding energy window.

To avoid such a dependency of the energy windows on the background level, a background image should always be taken before a measurement and then subtracted from each acquired image. Actually, the subtraction of the background image from each real image is done automatically by the CCD controller. It should be noted that background images should be measured within the same exposure time as the real images and without any incoming radiation, *i.e.*, with the x-ray shutter closed. The charges of the pixels in a background image are due to the dark current and readout noise. The background charges originating from the dark current are proportional to the acquisition time, whereas those due to the readout noise are constant. This on-line background subtraction from the collected images permits the use of beforehand chosen energy windows. However, the widths of the energy windows should be chosen carefully. In particular, as the widths of the charge frequency distributions are mostly due to the dark current noise of the CCD, increasing the exposure time may require the use of wider energy windows.

It should be mentioned also that the background image itself does not contain all types of background events. Scattered photons and cosmic rays are additional background components that cannot be eliminated before the analysis. If such a background event occurs in a multiple hit domain the total charge of this domain is too large. For this reason, if the total charge of a domain does not meet the condition of the energy window, the individual charges of all pixels belonging to the domain are probed.

The multiple hit analysis algorithm cannot distinguish between multiple hit events and photons diffracted in higher orders by the crystal. The algorithm treats indeed photons diffracted in the n^{th} order exactly in the same way as hits having a multiplicity equal to n . This may lead to systematic errors in the determination of the intensities, energies and widths of the x-ray lines of interest if the latter are in overlap with higher order x-ray lines originating, *e.g.*, from impurities or trace elements in the measured sample.

III.A-5 Comparison between the two algorithms

The two algorithms discussed above are compared in Figure III.A.4 and Figure III.A.4. Both figures represent the same high-resolution $K\alpha$ x-ray spectrum measured using either a weak fluorescence source corresponding to a low charge deposition rate in the CCD (Figure III.A.4) or an intense source corresponding to a high charge deposition rate (Figure III.A.5). The spectra were constructed by projecting the filtered two-dimensional CCD images onto the spectrometer dispersion axis which is parallel to the length of the CCD detector.

III DATA ANALYSIS AND DATA PROCESSING

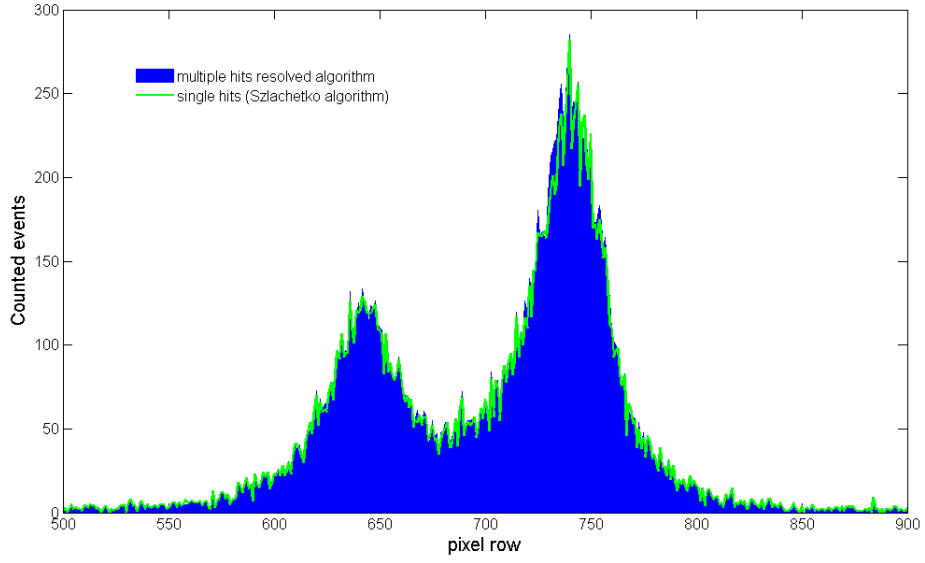


Figure III.A.4: Comparison between the two analysis algorithms for the case of a low CCD charge deposition rate.

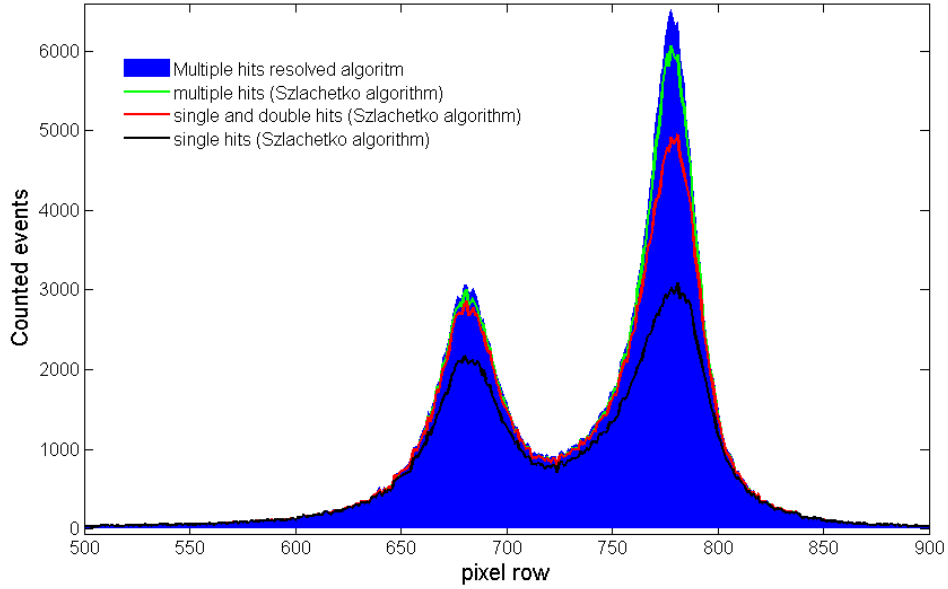


Figure III.A.5: Comparison between the two analysis algorithms for the case of a high CCD charge deposition rate.

It can be seen that for the low CCD charge deposition rate the resulting spectra are very similar. Nevertheless some small differences are visible. For instance, in the spectrum analyzed with the multiple hit algorithm some small additional peaks are observed which correspond probably to cosmic ray events. Slight differences in the noise distribution can also be seen.

In the spectrum corresponding to the high CCD charge deposition rate the comparison shows that the new algorithm surpasses the previous algorithm for multiple hit events.

III.B CCD image correction in the von Hamos geometry

All x-ray spectra presented in this work were measured by means of the high-resolution von Hamos bent crystal spectrometer of Fribourg [45]. For the detection of the diffracted photons a back-illuminated CCD camera was used. The use of a 2D detector provides the opportunity to perform a detailed investigation of the geometrical effects related to the von Hamos geometry.

The standard analysis of the CCD images involves the definition of a certain Region Of Interest (ROI) which restricts the number of the pixels to be analyzed. This restriction on the photon collection area permits to improve the angular resolution of the spectrometer, but on the other hand leads to a diminution of the integral intensity.

Nonetheless, a proper analysis of the whole CCD image without ROI restriction is possible and also useful since such an analysis can increase significantly the angular resolution and integral intensity of the signal. In this case, however, more sophisticated mathematical methods are required.

III.B-1 Image properties in the von Hamos geometry

In the von Hamos geometry, provided that the x-ray source is monochromatic and the latter as well as the detector are located both on the focal line of the cylindrically bent crystal, the image of a point-source remains a point. In such a configuration the x-ray radiation that reaches the detector propagates along the generatrices of two symmetric oblique circular cones. The directrix of both cones lies on the reflecting crystal. The apex of the first cone is the radiating point, and the apex of the second cone is the point-like image on the CCD. Moving away the source or the CCD from the focal line makes the image to become parabolic.

The image of an extended source can be considered as the sum of images of point-like sources.

III DATA ANALYSIS AND DATA PROCESSING

In the standard von Hamos setup the effective x-ray source is defined by a rectangular slit. The intersection of the focal line with the rectangular slit is a point so that the other points of the source are defocused. Thus, the resulting image of the slit on the [CCD](#) is no more rectangular but presents a characteristic "banana shape".

In the slit-less operation mode the slit is open widely and the effective source of radiation is the beam spot on the sample. In this case the whole source is out of focus. If the distance of the source from the focal line is large enough then all points of the source produce images with similar parabolic shapes which are slightly shifted with respect to each other. In the slit-less operation mode the image has thus the shape of a broadener parabola.

If the source and the detector are not located in the focal plane, *i.e.*, in the vertical plane containing the focal line, a point-like imaging of a point-source can be retrieved (provided that optical aberrations can be neglected) by moving the crystal along the [CRF](#) axis which is perpendicular to the direction of dispersion of the spectrometer. This is not always possible, however, because the range of the [CRF](#) axis is limited to 30 mm. Moreover, as it will be shown later, the parabolic shape of the image on the [CCD](#) can be useful, especially in the case of [GEXRF](#) measurements.

III.B-2 GEXRF related properties

Let us consider the case in which the source point is located on the focal line and the detector is out of focus. Also in such a configuration the x-ray radiation that reaches the detector propagates along the generatrices of two cones. The apex of the first cone is the radiating point and the directrix lies on the reflecting crystal. The second cone is the image of the first one with respect to the plane containing the base of the cone.

Because the detector lies out of focus, the image on the [CCD](#) has a parabolic "banana" shape, *i.e.*, the shape of the intersection of a cone section with a plane (detector front surface).

Due to the form of the radiation paths the grazing angle between the radiation direction and the surface of the sample is not uniform along the directrix of the emission cone. The grazing angle is the largest for the Bragg reflections taking place in the central part of the crystal. Reflections at other parts of the crystal correspond to smaller grazing angles.

As a consequence the resulting [CCD](#) image represents a certain range of exit angles which vary across the "banana"-like image. A proper analysis of [GEXRF](#) images should account for such optical aberrations and be able to determine the correct exit angles.

III.B-3 Applying corrections to a CCD image

Once the method to model the image shape on the [CCD](#) is defined, the optimal set of parameters to fit the acquired images can be found. With such a set of parameters the calculation of the Bragg angle, exit angle and projection of the radiation direction on the surface of the sample can be performed for each individual pixel of the [CCD](#) image. The way to find the optimal parameters is presented in [Appendix E](#) on page 161.

An acquired image can then be represented in different colors as a function of the collected x-ray intensity and, depending on needs, as a function of the Bragg angle (or corresponding x-ray energy), pixel number, exit angle or as a function of the coordinates x and y corresponding to the projection of the radiation direction on the surface of the sample.

In the case of [GEXRF](#) angular scans the acquisition is performed for many (from 20 to 200) exit angles. With the y coordinates transformed to exit angles consecutive images can be summed up along the exit angle axis. The results can be presented as a [2D](#) plot of the overall intensity per exit angle or as a [3D](#) image of the [GEXRF](#) scan with the third axis corresponding to the energy, projection of the radiation direction, *etc.* Detailed instructions for the creation of the different [GEXRF](#) profiles are presented in [Appendix F](#) on page 169.

III.B-4 Calculations of images

Following the notations used in [45, 60] (see also [Figure II.A.1](#) on page 27) we assign the x -axis to the dispersion direction of the crystal and the z -axis to the focusing direction, the crystal being bent around the x -axis in the y - z plane.

Let us further define the following geometrical parameters:

$S = (S_x, S_y, S_z)$ the emitting point,

$R = (R_x, R_y, R_z)$ the point of incidence on the crystal,

\vec{R} the x-ray vector incident to the crystal,

$P = (P_x, P_y, P_z)$ the point-like image,

\vec{P} the x-ray vector reflected by the crystal,

ρ the radius of curvature of the crystal,

θ_B the Bragg angle and

Ψ the angle suspended by the arc of a circle whose length is defined by the points (R_x, R_y, R_z) and $(R_x, R_y, 0)$.

III DATA ANALYSIS AND DATA PROCESSING

For consistency with the above axes' definition, we choose a coordinate system O with its origin located at the position of the slit center and with the x direction parallel to the translation axis of the detector. However, the slit center may not lie exactly on the focal line of the crystal; moreover, due to mechanical misalignments, the focal line may be slightly tilted with respect to the translation direction of the detector. For these reasons the optical path calculations were performed using the coordinate system O' in which the x' axis is collinear with the curvature axis of the reflecting crystal.

Detailed calculations of the coordinates of a point of incidence on the crystal can be found in [60]. The final result has the following form:

$$R' = \left(S'_x + \sqrt{|BR|^2 \cot^2 \theta_B - |AB|^2}, -\rho \sin(\Psi), \rho \cos(\Psi) \right), \quad (\text{III.B.1})$$

where $|BR|$ and $|AB|$ are functions of ρ , Ψ , S'_y and S'_z .

The incident ray vector \vec{R} can be written as:

$$\vec{R} = \overrightarrow{SR}, \quad (\text{III.B.2})$$

and the reflected ray vector \vec{P} can be determined as the symmetric vector to \vec{R} with respect to the crystal normal $\vec{n} = (0, -\sin(\Psi), \cos(\Psi))$:

$$\vec{P} = \vec{R} - 2 \left(\vec{R} \cdot \vec{n} \right) \vec{n} \quad (\text{III.B.3})$$

The image point is given by the intersection of a line collinear with \vec{P} and the [CCD](#) plane. We can again transform our coordinate system into a system O'' so that the detector lies in the $y'' = 0$ plane. Then the image points can be easily found from a translation of R by the scaled \vec{P} vector:

$$P = R + \alpha \vec{P}, \quad (\text{III.B.4})$$

where $R''_y + \alpha \left(\vec{P} \cdot \hat{e}''_y \right) = 0$.

If the sample has a flat surface then the exit angle φ of a fluorescence x-ray is given by:

$$\varphi = \arccos \frac{\vec{n}_S \cdot \vec{R}}{|\vec{R}|}, \quad (\text{III.B.5})$$

where \vec{n}_S is the unit vector normal to the sample surface.

The angle ϑ between the x-ray radiation direction and the sample surface orientation can be calculated similarly using a vector \vec{t}_S tangent to the sample surface.

$$\vartheta = \arccos \frac{\vec{t}_S \cdot \vec{R}}{|\vec{R}|}, \quad (\text{III.B.6})$$

A dedicated Matlab function was written for the calculation of the von Hamos images. The function manual can be found in [Appendix A](#) on page 145.

III.B-5 Angular resolution

To each point on the [CCD](#) detector we can attribute a corresponding Bragg angle (thus energy) and exit angle. It should be noted that along the dispersion direction of the crystal the exit angle change is equal to the Bragg angle change as long as the projection of the radiation direction on the sample surface is constant. However, along the focusing direction of the crystal the radiation direction changes resulting in an additional shift of the exit angle.

There are three main factors that can influence the resolution of both the Bragg and exit angles. These are:

- the [Darwin width](#) of the diffracting crystal,
- the size of the fluorescence source,
- the [CCD](#) pixel's dimensions.

In the following the above listed contributions will be estimated for the case of the spectrometer of the University of Fribourg [45].

III.B-5.1 Darwin width

The Bragg angle resolution is affected first by the Bragg reflection itself. The parameter that characterises the Bragg reflection angular resolution is the [Darwin width](#). The [Darwin widths](#) of the crystals used for this work are presented in [Table III.B.1](#).

	Si(220)	Ge(220)	SiO ₂ (1-10)	SiO ₂ (2-23)	TiAP(001)
σ max	0.006	0.02	0.01	0.001	0.1
π max	0.003	0.009	0.007	0.0005	0.09
σ min	0.002	0.004	0.002	0.0004	0.04
π min	4e ⁻⁶	0.0002	0.0002	0.0004	0.001

Table III.B.1: Darwin widths in first order of diffraction for the crystals employed in the present study (from [61]). The widths are given for σ and π polarized x-rays and for Bragg angles varying from 25° (label min) to 60° (label max). Quoted values are expressed in degrees.

III.B-5.2 Size of the fluorescence source

III.B-5.2.1 Horizontal dimension

The influence of the horizontal dimension dX_S of the radiation source to the Bragg and exit angle resolution can be calculated from (III.B.1) and (III.B.4). From the latter one can conclude that horizontally the image is also broadened by dX_S . Fortunately in the case of GEXRF measurements the effective horizontal dimension of the source and thus of the image is drastically reduced because it is proportional to the sine of the exit angle. If the GEXRF angular scan is performed up to 2° then the maximum image broadening dX_P is:

$$dX_P = \sin(2^\circ)dX_S \approx 0.03dX_S. \quad (\text{III.B.7})$$

The corresponding angular resolution is then:

$$\delta\theta_B = \arctan \frac{2\rho}{2\rho \cot \theta_B + dX_P}. \quad (\text{III.B.8})$$

III.B-5.2.2 Vertical dimension

The effect of the vertical extent of the source is more difficult to calculate explicitly. Unfortunately, it is usually more pronounced.

The image of a vertical line consists of a sum of parabolic segments corresponding each to an individual point source. The vertical distance between two parabolic segments is proportional to the distance between the corresponding source points. The image has the characteristic shape of a “banana” with a narrower central part.

For a given vertical position of the point source the resulting resolution can be calculated from the Bragg and exit angle distributions of a calculated image. The resolution is the smallest in the central part of the image and the largest in the upper and lower parts.

III.B-5.2.3 Physical source dimensions

It should be noted that very often it is not possible to determine precisely the dimensions of the fluorescence source. This is mainly due to the fact that the photon or particle beam employed to produce the sample fluorescence has a non uniform intensity distribution. The beam spot size can be estimated by determining the sample region with a fluorescence intensity above a certain threshold.

III.B-5.3 CCD pixel dimensions

Another factor that influences the angular resolution is the spatial resolution of the detector. For a CCD camera the spatial resolution is directly related to the pixel size.

We have used a CCD camera consisting of $20 \times 20 \mu\text{m}$ pixels. Using equation (III.B.8) one finds that a distance $dX_P = 20 \mu\text{m}$ in the dispersion direction corresponds to Bragg (and exit) angle differences which vary from 0.0001° up to 0.002° for Bragg angles ranging from 25° to 60° .

In the focusing direction the change of the Bragg angle is proportional to the curvature of the “banana” shape and found to be rather small.

Finally, the change of the exit angle, in turn, depends on the vertical extent of the image. The overall variation range of the exit angles extends from 0.3° to 0.4° . For an image height corresponding to 200 pixels this results in an exit angle resolution of $\sim 0.002^\circ$.

III.C Geometrical optics approach to GEXRF and GIXRF

Below a [Geometrical Optics \(GO\)](#) based ray tracing algorithm will be presented. For clarity we will describe the problem for the case of [GIXRF](#). However, knowing that [GEXRF](#) is a reciprocal method the argumentation is also valid for the later case.

III.C-1 Standing waves

A very elegant and widely used way of interpreting the [GIXRF](#) measurements of, for example, nanoparticles on surfaces consists to calculate the [XSW](#) field resulting from the interference between the incident beam and the part of the beam which is subject to external total-reflection. The change of the incident angle modifies the [XSW](#) field, *i.e.*, the radiation intensity exciting the surface particles, yielding changes in the x-ray fluorescence signal. However, the [XSW](#) based theory treats the particles as a small perturbation, which is only valid if absorption and interference effects caused by the particles can be neglected [27]. This requires small particle dimensions and large distances between them. For wide and densely distributed structures the [XSW](#) approximation is likely to fail.

Alternatively, provided the wavelength of the exciting radiation is much smaller than the size of the structures, the concept of [GO](#) can be used. Here, a [GO](#)-based ray tracing approach taking into account reflection, refraction, and absorption effects is considered. Assuming the optical path differences between different rays to be shorter than a predefined coherence length, the interference of different rays at a given point can be taken into consideration by simply summing the amplitudes of the corresponding waves. In the geometrical optics approach the [XSW](#) method can be seen as a limiting case of very small and sparsely distributed particles where absorption and multiple reflections inside the particles are negligible.

III.C-2 Intermediate morphology

The transition of the x-ray fluorescence emission from a particle-like to a layer-like morphology is still not fully understood. In literature such samples with an intermediate morphology are treated as layer-like structures with the roughness introduced as a small perturbation of the interface potential (Nevot-Croce model) [33], as a stack of layers with reduced average densities [41], or as a composition of layers of different thicknesses [44]. These crude models, however, cannot be used for surfaces characterized by large roughnesses and/or highly correlated height distributions [37], or for grainy structures for which the incident x-ray radiation passes through several successive grains [44]. For those sample systems the well-established XSW approach will yield reliable results only in very specific cases, *e.g.*, surface depositions with low-Z elements of neglectable absorption.

III.C-3 Ray tracing

For x-rays with an energy above about 2 keV, the wavelength is smaller than the dimensions of the investigated structures. Thus, the incident x-ray beam can be treated in a purely geometric approach, *i.e.*, the geometrical optics ray tracing method. In general, the latter describes very well the effects of reflection, refraction, transmission and absorption. In this work a 2D reverse ray tracing approach was developed which tracks the full evolution of plane waves from their source to the point, where they are absorbed. For nanoscaled structures, where absorption in the detection channel has a negligible small effect, the number of detected fluorescence photons is directly proportional to the number of absorptions taking place in the sample. Therefore, in order to get the final radiation intensity, one has to consider all the possible ray paths between the source and a given absorption point, taking into account the interferences of the different rays. This is, however, a very complex and hardly solvable problem.

To significantly reduce the free parameters, two assumptions were made:

1. the exciting beam is perfectly parallel;
2. the on-surface objects have only horizontal and vertical interfaces.

With these assumptions, for any given incident radiation direction, the refraction into the structure can be realized only on a horizontal or a vertical interface. Of course, the direction of a ray passing through the vacuum between two vertical interfaces of neighboring structure elements does not change.

In a 2D coordinate system, where the axis x lies in the plane of the substrate surface and the axis y is perpendicular to that interface, reflections at the horizontal interfaces

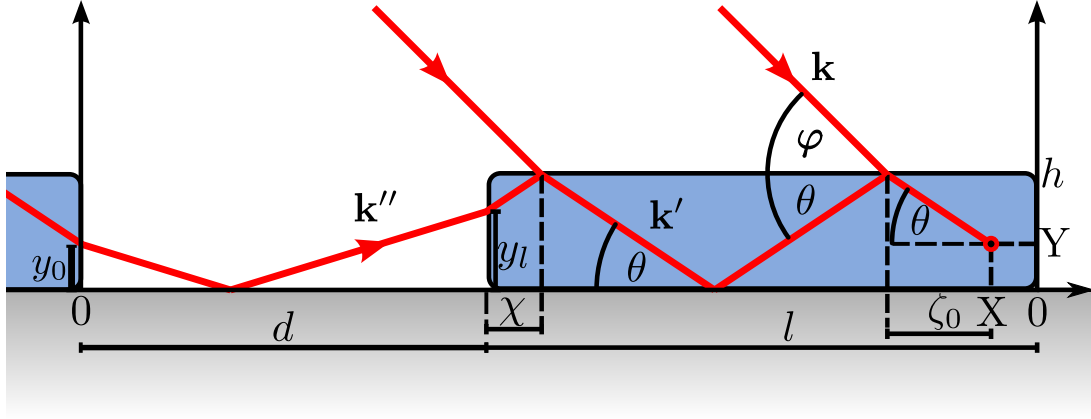


Figure III.C.1: Graphical representation of a ray path in a rectangular island structure. The symbols are explained in the text.

change only the y -component of the wave vector, the length of the latter remaining unchanged.

Reflections at vertical interfaces can be neglected as in the x-ray regime the reflectivity quickly goes to zero for large angles of incidence. Thus, provided that a structure has a constant height, only four final ray path directions have to be considered: two ray path directions (up and down) for incident radiation reaching the structure from horizontal interfaces, and two ray path directions (up and down) for incident radiation reaching the structure from vertical interfaces. However, due to multiple reflections in the structure elements, the actual number of x-ray paths is usually much higher than four. Actually, as shown in [Figure III.C.1](#), a fluorescence point can be reached by the incoming radiation after 0, 1, 2, *etc.*, reflections at the horizontal interfaces of the structure elements.

If structure elements differ in height then the number of ray path directions that should be considered grows but still can be limited to a tractable number.

In order to obtain an information on the whole sample, the ray tracing should be performed for as many absorption points as needed.

For the purpose of this work a dedicated Matlab program has been written (see [Appendix D](#) on page 155) that computes [GEXRF/GIXRF](#) intensities for rectangular islands on a flat support.

III.C-3.1 Roughness model

The effects of the surface roughness can significantly change the [GIXRF/GEXRF](#) signal [33, 35–37, 41, 42, 44, 62]. Thus, it is of paramount importance to introduce a roughness model into the ray tracing method.

It this work a very simple roughness model was used. Keeping in mind the above stated assumption about the structures' interfaces that should be either horizontal or vertical, the roughness can be introduced as a simple height variation $h(x)$ of the structure with a standard deviation σ_h corresponding to the [rms](#) of the roughness.

It should be noted that this model ignores the effects of the scattering of the radiation at the interface.

III.C-3.2 Reverse ray tracing algorithm

Let us consider an absorption point of coordinates $[X, Y]$ located in an island of length l , variable height $h(x)$ and distant by d from the previous neighboring island.

The incident radiation can be characterize by the following ray vector \vec{k} :

$$\vec{k} = (k_x, -k_y) = k (\cos \varphi, -\sin \varphi), \quad (\text{III.C.1})$$

where k is the radiation wave number and φ the angle of incidence. The wave vector \vec{k}' of the radiation refracted into the structure can be described as follows – if the radiation reaches the vertical interface:

$$\vec{k}' = \left(\sqrt{(nk)^2 - k_y^2}, -k_y \right), \quad (\text{III.C.2})$$

or, if the radiation reaches the horizontal interface:

$$\vec{k}' = \left(k_x, -\sqrt{(nk)^2 - k_x^2} \right), \quad (\text{III.C.3})$$

where n stands for the refraction index for x-rays of the structure material.

If the height of the structure elements varies then the ray vectors resulting from the following recursive equations are taken into consideration (see [Figure III.C.2](#)):

$$\begin{aligned} \vec{k}'_0 &= \left(\sqrt{(nk)^2 - k_y^2}, -k_y \right), \\ \vec{k}'_{i+1} &= \left(\sqrt{k^2 - k_{iy}'^2}, -\sqrt{(nk)^2 - k^2 + k_{iy}'^2} \right), \\ \vec{k}'_{i-1} &= \left(\sqrt{(nk)^2 - k^2 + k_{ix}'^2}, -\sqrt{k^2 - k_{ix}'^2} \right). \end{aligned} \quad (\text{III.C.4})$$

It should be noted that the \vec{k}'_0 and \vec{k}'_1 values given by the equations [\(III.C.2\)](#) and [\(III.C.3\)](#) can be retrieved from the first and second ($i = 0$) equations [\(III.C.4\)](#).

For a given wave vector \vec{k}' the ray paths with the following final wave vector components have to be considered: (k'_x, k'_y) and $(k'_x, -k'_y)$.

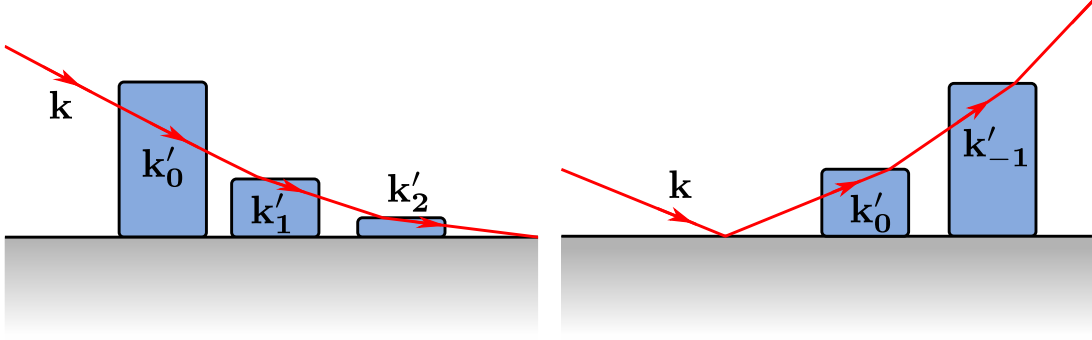


Figure III.C.2: Various wave vectors as described in text.

The incident angle of the refracted radiation is given by:

$$\theta = \arctan \frac{\Re k'_y}{\Re k'_x}, \quad (\text{III.C.5})$$

where $\Re z = \frac{1}{2}(z + \bar{z})$ stands for the real part of the complex number z . The lateral distance between the absorption point and the last reflection on the top interface of a structure can be written as:

$$\zeta_0 = \begin{cases} (h_1 + Y) \cot \theta & \text{for } k'_y > 0 \\ (h_1 - Y) \cot \theta & \text{for } k'_y < 0 \end{cases} \quad (\text{III.C.6})$$

whereas for the ray paths where a higher number of reflections occur the distance between two consecutive reflections on the top interface of the structure element is given by:

$$\zeta_i = (h_{i-1} + h_i) \cot \theta, \quad (\text{III.C.7})$$

where h_i is the island's height at the i^{th} top interface reflection.

The maximal number N of top interface reflections in a structure element is:

$$N = \max \left\{ \tilde{N} \in \mathbb{N} : \sum_{i=1}^{\tilde{N}} \zeta_i \leq l - X \right\}. \quad (\text{III.C.8})$$

A longer ray path, entering the structure element by a vertical interface, covers an additional distance χ :

$$\chi = l - X - \sum_{i=1}^N \zeta_i, \quad (\text{III.C.9})$$

and enters the structure element at the height y_l :

$$y_l = |h_N - \chi \tan \theta|. \quad (\text{III.C.10})$$

III DATA ANALYSIS AND DATA PROCESSING

At the vacuum side of the vertical interface the wave vector \vec{k}'' of the ray path has the following form:

$$\vec{k}'' = \left(\sqrt{k^2 - k_y'^2}, k_y' \right), \quad (\text{III.C.11})$$

The ray path crosses the vertical interface of the consecutive element at the height of:

$$y_0 = \left| y_l + \text{sgn}(\chi \tan \theta - h_N) \cdot d \cdot \frac{\Re k_y''}{\Re k_x''} \right|. \quad (\text{III.C.12})$$

If the following condition is fulfilled:

$$y_0 < h, \quad (\text{III.C.13})$$

the ray tracing procedure can be repeated for coordinates relative to the next element starting at the point $[0, y_0]$.

If the condition (III.C.13) is not fulfilled and $k_y'' > 0$, then the ray tracing procedure can be repeated for the ray vector \vec{k}_{i+1}' and coordinates relative to the next element starting at the point $\left[\frac{\Re k_x''}{\Re k_y''}(y_l - h) - d, y_0 \right]$ provided that:

$$-l < \frac{\Re k_x''}{\Re k_y''}(y_l - h) - d < 0 \quad (\text{III.C.14})$$

For the ray vectors $\vec{k}_{i>0}'$ also the rays refracted at the top interface should be checked for the condition (III.C.13) with y_0 defined as follows:

$$y_0 = h_j + (d + l - x_j) \frac{\Re k_y^*}{\Re k_x^*}, \quad (\text{III.C.15})$$

where $[h_j, x_j]$ are the coordinates of the refraction point and \vec{k}^* is the wave vector at the vacuum side of the horizontal interface:

$$\vec{k}^* = \left(k_x', -\sqrt{k^2 - k_x'^2} \right). \quad (\text{III.C.16})$$

If the condition (III.C.13) is fulfilled the ray tracing procedure can be continued for the wave vector \vec{k}_{i-1} and the coordinates relative to the next element starting at the point $[0, y_0]$.

If the condition (III.C.13) is not fulfilled and if the wave vector of the considered ray path after the first refraction has the form (III.C.3) or (III.C.2), then the resulting radiation amplitude evolution is calculated and added to the radiation intensity at the absorption point.

The amplitude evolution E across the ray path follows the wave equation:

$$E = E_0 \prod_{j,k,l} r_k t_l \exp \left\{ -i \Delta x_j \left(k_{jx} + k_{jx} \frac{\Re k_{jy}}{\Re k_{jx}} \right) \right\}, \quad (\text{III.C.17})$$

where E_0 is the initial amplitude, Δx_j is the lateral distance between consecutive top interface reflections and/or refractions on vertical interfaces (*e.g.* ζ and χ), (k_{jx}, k_{jy}) is the wave vector at the distance Δx_j , and r_k and t_l stand respectively for the reflection and transmission coefficients for all reflections and transmissions encountered in the ray path.

The ray tracing procedure is stopped whenever the ray path amplitude calculated with (III.C.17) becomes smaller than a previously chosen threshold. The number of wave vectors \vec{k}_i to consider should also be limited to a reasonable number.

III.C-3.3 Optical paths coherence

For the interference effects to occur the interfering optical paths need to be coherent. This implies that the length difference between the optical paths should be within the radiation coherence length ξ .

In case of [GIXRF](#) the coherence length depends on the radiation source parameters and can reach up to several microns for third generation synchrotron radiation sources [63]. For the case of [GEXRF](#) the coherence length is related to a life time of a fluorescent state τ by relation:

$$\xi = \tau c. \quad (\text{III.C.18})$$

The resulted intensity I can be calculated with the following integral:

$$I = \int dx \left| \sum_i E_i C_\xi(x - L_i) \right|^2, \quad (\text{III.C.19})$$

where E_i is the electric field of the ray path i at the absorption point, $C_\xi(x)$ is the coherence correlation function characterized by the coherence length ξ and L_i is the length of the optical path i .

In the above equation only the amplitudes of the ray paths which have some degree of coherence, *i.e.*, $C_\xi(L_i - L_j) \neq 0$, are taken into consideration in the sum. If the length difference between the optical paths is too high, *i.e.*, $C_\xi(L_i - L_j) = 0$, only the sum of the squared amplitudes is performed $I = \sum_i |E_i|^2$

III.C-3.4 Multi structures

So far we have only considered structures made of a single element and of constant height (if we neglect the roughness). Nevertheless, a similar methodology can be applied to multi structures, *i.e.*, structures made of several elements and having different

III DATA ANALYSIS AND DATA PROCESSING

heights. Obviously, by increasing the complexity of the investigated structure, the difficulty of the related mathematical problem increases, too.

If the same procedure as the one presented in the previous section is repeated, one sees that the number of possible ray vectors reaching the detector increases drastically with the number of elements contained in the structure. This is primarily due to the fact that a ray passing through the vacuum between two islands made of different elements does not preserve its direction. A second reason is the deflection undergone by the ray path when passing from a top to a side interface and *vice versa*.

As a consequence, the number of optical paths to consider would be much more than four, remaining, however, a finite number.

III.D Effective flux of incidence radiation

In the case of granular structures a part of the incident radiation might be reflected on the substrate surface without reaching the on-surface objects. As a consequence, a part of the incoming beam intensity does not contribute to the fluorescence production of the structure of interest. Moreover, the relative intensity of this inactive beam part changes as a function of the grazing incidence angle. In order to properly calculate the angular evolution of the fluorescence intensity for a granular structure the beam flux Φ has therefore to be corrected.

III.D-1 Effective flux calculation

The incident radiation can be divided into three parts (see [Figure III.D.1](#)):

- I the radiation reaching the structure elements directly,
- II the radiation reaching the structure after a reflection and

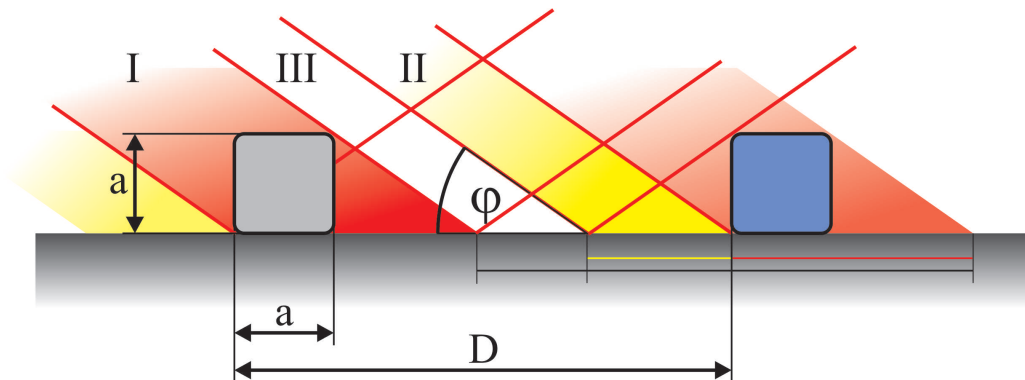


Figure III.D.1: Illustration of the effective flux for an on-surface structure of evenly distributed squares and an incidence angle φ of the incoming radiation.

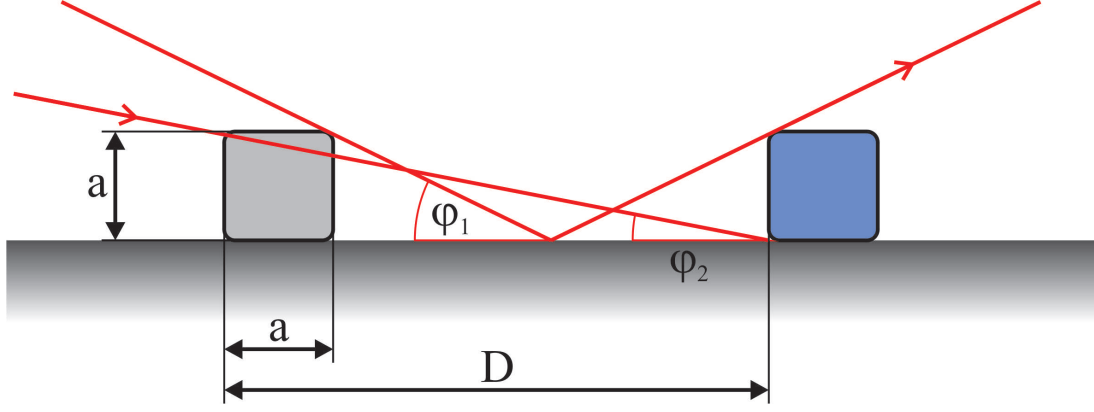


Figure III.D.2: Boundary case ($\varphi_1 = \arctan \frac{D-a}{2a}$) of incident angles for which $\Phi_{eff} = \Phi$.

III the radiation which never reaches the structure.

The effective flux Φ_{eff} that should be considered can be given with the ratio σ :

$$\Phi_{eff} = \sigma \cdot \Phi = \frac{\text{I} + \text{II}}{\text{I} + \text{II} + \text{III}} \Phi. \quad (\text{III.D.1})$$

The calculation of Φ_{eff} requires the knowledge of the distribution and dimensions of the on-surface objects and in most cases it cannot be obtained from in a simple formula. Still, the general rule is that σ is equal to the covering rate R of the structure if the radiation is perpendicular to the surface and reaches the limit value of 1 for very shallow angles.

As an example let us consider a 2D structure consisting of evenly distributed squares with a side length a , the distance between two consecutive squares being D (see Figure III.D.1 and Figure III.D.2). For the radiation perpendicular to the surface σ is equal to the covering rate of the structure, *i.e.*, $R = \frac{a}{D}$. For smaller incidence angles, σ can be derived from the following formula:

$$\sigma = \begin{cases} R(1 + 2 \cot \varphi) & \text{if } \varphi > \arctan \frac{D-a}{2a} \\ 1 & \text{else.} \end{cases} \quad (\text{III.D.2})$$

For a well characterized structure σ is calculated using the structure parameters obtained from SEM or AFM images.

III.D-2 GEXRF and GIXRF comparison

In the case of GEXRF the incident angle of the incoming beam is large and the sample is rotated only over a narrow angular range during the measurement. Thus the change

III.D EFFECTIVE FLUX OF INCIDENCE RADIATION

of the cross section corresponding to the intersection of the incident radiation with the on-surface structure is negligible, the cross section being proportional to $\cot \varphi$ (III.D.2).

For GIXRF the situation is drastically different since the sample is irradiated by the incoming beam under very small angles. In this case, the change of the effective flux of the incidence radiation and consequently the one of the fluorescence intensity may be huge, even within a single angular scan. Corrections for the effective flux are thus mandatory for a correct interpretation of GIXRF angular scans.

III.D-3 Buried structures

Above considerations about effective flux corrections are also applicable to structures buried in a substrate, *e.g.*, to depth profile measurements of impurities implanted in wafers. However, in this case the corrections should be applied to the refracted beam.

Chapter IV

Results and Discussion

IV.A Periodic structures

IV.A-1 Cr pads

The Cr pads (see [Subsection II.C-2.1](#) on page 52) were measured with the [GIXRF](#) technique (see [Sub-chapter II.B](#) on page 43). The structures were specially designed in order to minimize the normalisation for geometrical effects. Thus the correction for the effective flux (see [Sub-chapter III.D](#) on page 87) was not necessary. Additionally, in order to facilitate the intensity normalisation for the effective solid angle of detection, the samples were mounted in such a way that the lines on which the Cr pads were deposited were along the beam footprint.

The results of the measurements have been already published in [25, 54]. For illustration, some results are plotted in [Figure IV.A.1](#). It can be seen that the measured profiles present clear particle-like characteristics.

Because the chromium pads structure was designed with a lift-off technology, all the structure morphology parameters needed for simulations were taken directly from

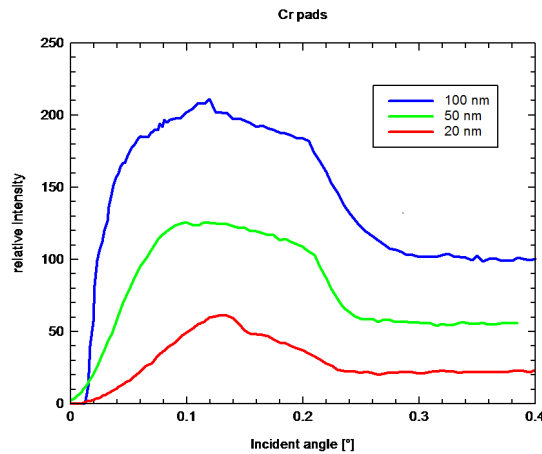


Figure IV.A.1: [GIXRF](#) profiles of Cr pads. The intensity scale is normalized in such a way that for large incident angles the intensity corresponds to the pads height.

IV RESULTS AND DISCUSSION

the sample specification. The performed SEM images (see Figure II.C.2 on page 52) confirm this approach.

IV.A-1.1 XSW simulation

As it can be seen from Figure IV.A.2.a the XSW simulation only roughly reproduces the measurement. The simulation exhibits a faster intensity growth at shallow incident angles when compared to the measurement. Moreover, the predicted pronounced interference fringes are not present in the acquired data. Only the critical angle position and the average intensity in the particle like region are reproduced.

In [54] an adapted quantification procedure is presented that deals with extended lateral dimensions of the pads. This procedure results in an integral modification factor for the XSW intensity changing with the height and length of the pads. This factor is then applied to the easily calculable undisturbed XSW above the support surface

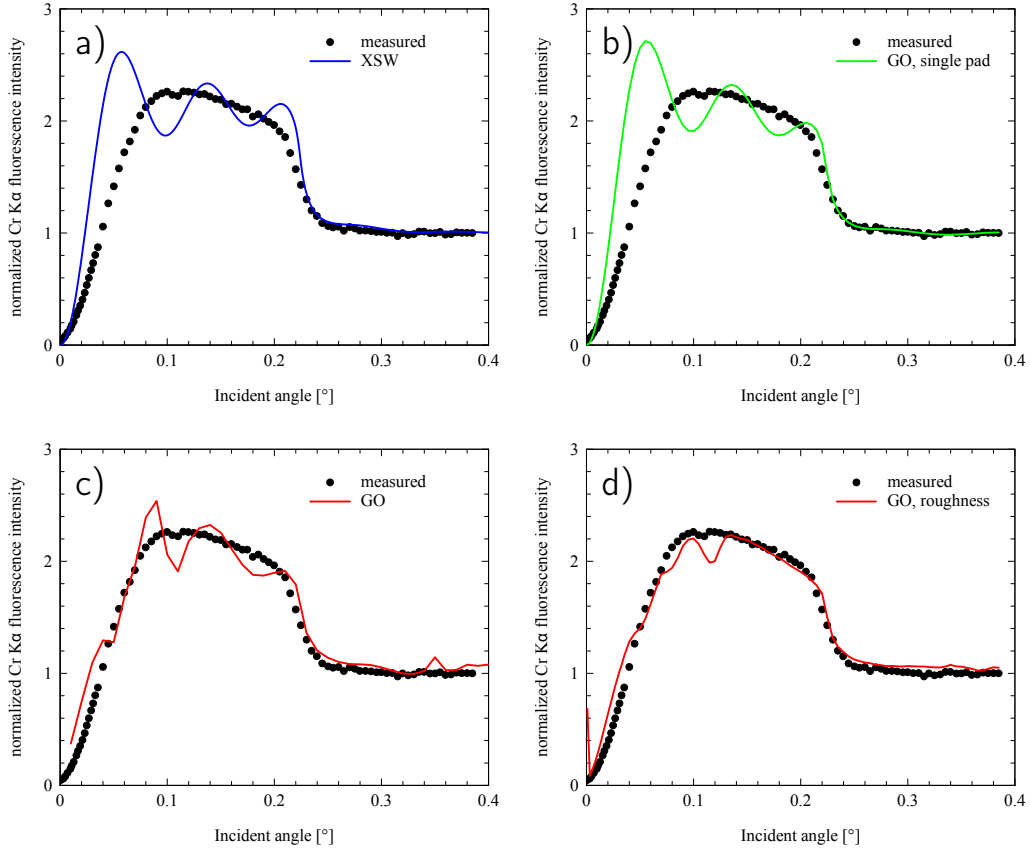


Figure IV.A.2: Simulations of the GIXRF profiles of the 50 nm Cr pads: (a) XSW simulation, (b) single island GO ray tracing simulation, (c) GO ray tracing over the full structure with no surface roughness (c) GO ray tracing over the full structure comprising the surface roughness.

in order to describe the effective excitation intensity within the pads. The difference between the initially calculated [XSW](#) intensity and the modified value ranges from 15 % to 25 %. However, it seems that there is no good agreement between the proposed calculations and the measurements.

IV.A-1.2 GO simulations

The [GO](#) ray tracing simulations were performed for three different configurations – for a single (or well separated) pad, for an ideal pattern of pads with no roughness, and for the pattern of pads with an introduced surface roughness.

The [GO](#) simulation of a single pad ([Figure IV.A.2.b](#)) does not yield a much better profile than the [XSW](#) field approach. However, it shows a slightly better match around the critical angle because attenuation effects were accounted for.

The [GO](#) simulation that considers the full pads pattern ([Figure IV.A.2.c](#)) fits the data far better. As an effect of consecutive pads shadowing, the intensity growth at shallow angles is well reproduced. Also the intensity decrease around the critical angle is very close to the measured one.

After introducing an additional pad's surface roughness of 5 nm [rms](#) the interference fringes smear out (see [Figure IV.A.2.d](#)). As a result, a [GO](#) simulation is obtained that very well represents the measured data. In comparison to currently used models (*i.e.* [XSW](#) simulations) the agreement is excellent.

IV.A-2 Cr stripes

The sample with Cr stripes (see [Subsection II.C-2.2](#) on page 52) was studied with both [GEXRF](#) and [GIXRF](#) techniques. Measurements at different angles ϑ of the sample surface orientation allowed for the investigation of the [GEXRF](#)/[GIXRF](#) profiles of different periodicities p corresponding to $p_0/\sin \vartheta$.

For $\vartheta = 0$ the [GEXRF](#)/[GIXRF](#) spectra exhibit layer-like profiles of a 10 nm Cr layer (see [Figure IV.A.3.a](#)) corresponding to the nominal thickness of the structure. Increasing ϑ , a characteristic peak corresponding to particle-like profiles becomes visible at φ_c of the support (see [Figure IV.A.4](#) on page 97). When recording the [GIXRF](#) spectra for higher ϑ , in addition to those two main features, a modulation above the critical angle of external total reflection of the substrate can be observed. The frequency of this modulation decreases with the sine of the tilt angle ϑ (see [Figure IV.A.3.b, c and d](#)).

IV RESULTS AND DISCUSSION

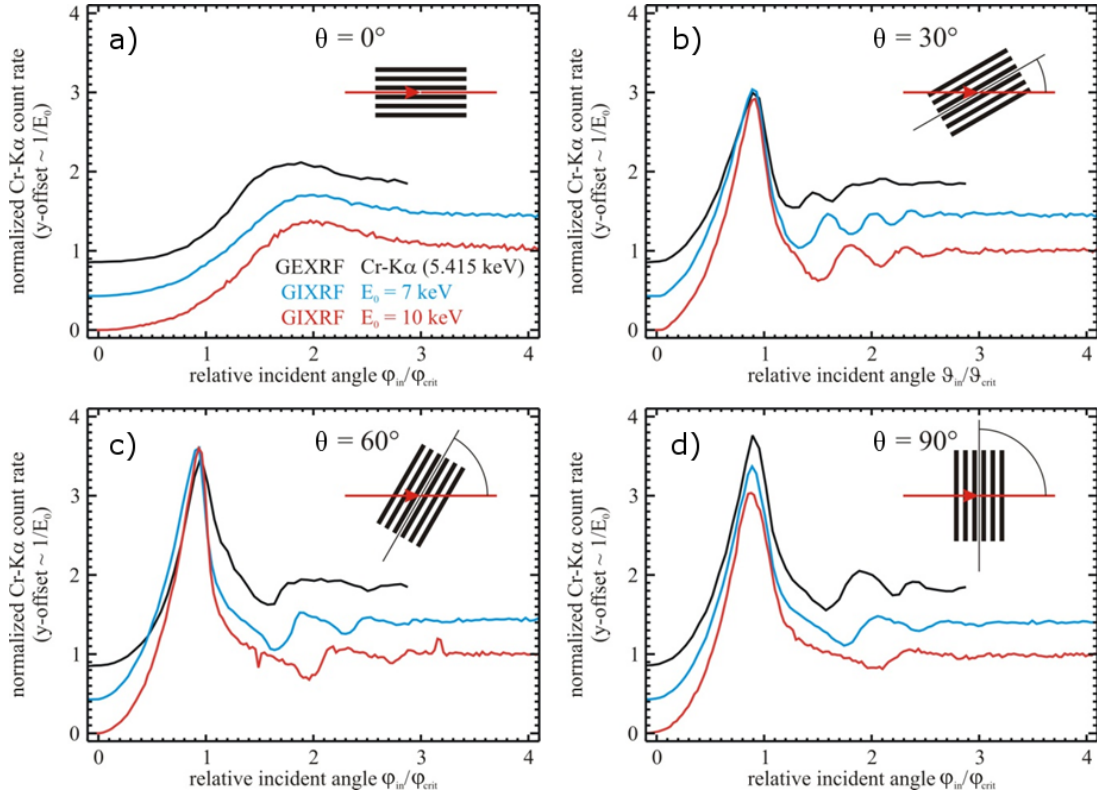


Figure IV.A.3: GEXRF and GIXRF angular profiles of the Cr stripes sample. The grazing angles are normalized to the critical angle of the silica support φ_{Si} , and the intensity is normalized to one for large angles.

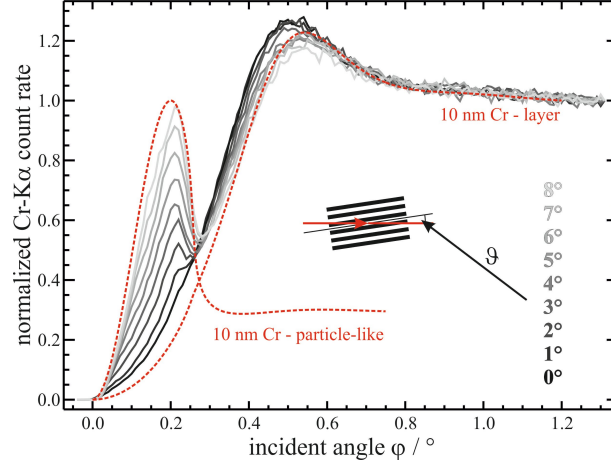


Figure IV.A.4: [GIXRF](#) data for tilt angles ϑ from 0° to 8° . For $\vartheta = 0^\circ$ the measured spectrum follows the [XSW](#) calculations for a 10 nm chromium layer. For all other tilt angles the angular profile shows an additional feature which corresponds to a particle-like chromium contamination on a Si wafer and becomes more intense for larger ϑ .

IV.A-2.1 XSW field calculations

[XSW](#) field intensities were calculated for the incident photon energy of 7 keV using the IMD software package [64]. Two different components were considered: the layer-like contribution, namely a 10 nm thick chromium layer on a Si bulk, and the particle-like contribution, which was obtained from the calculation of the [XSW](#) above a flat Si substrate and successive integration over the first 10 nm. The idea was to simulate the excitation intensity of the chromium structures by a simple linear combination of those two [XSW](#) contributions.

If the sample is excited along the lines ($\vartheta = 0$), two distinct interactions between the sample and the incident beam can take place: either the beam impinges onto the Cr bars – then the interaction is that of a closed Cr layer, or the beam hits the Si substrate – then above the Si substrate the usual undisturbed [XSW](#) emerges along the beam propagation direction. Without any component of the lines sidewalls being orthogonal to this direction there is no significant interaction with chromium. Thus, in the angle dependent Cr signal only the contribution of a 10 nm layer is to be expected.

For all tilt angles $\vartheta \neq 0$ there is a component of the Cr sidewalls that will interact with the [XSW](#) which forms above the Si surface. This will result in an additional angular dependence which corresponds to the signal of a thin, non-absorbing layer [4] respectively that of an particle deposited on a Si substrate.

In figure IV.A.4 the recorded [GIXRF](#) spectra for tilt angles ϑ from 0° to 8° are shown and compared to the two distinct [XSW](#) contributions. It is evident that this

IV RESULTS AND DISCUSSION

simple superposition of the two contributions leads to very satisfying results for these values for ϑ .

There is however a difference between the maximum position of the measured layer-like signal which could be overcome by assuming a thicker layer. This contradicts the particle-like signal, where a better fit could be achieved by assuming smaller particles, because the measured curve appears to be ‘sharper’ than the calculated one with a maximum shifted slightly to higher angles. In [Figure IV.A.5.c](#) a XSW simulation is presented where the 2 nm non-absorbing layer and the 10 nm absorbing layer were taken correspondingly as particle-like and layer like components. The resulting simulations quite well represent the measured GIXRF profiles, though no intensity modulations above φ_{Si} are visible.

IV.A-2.2 GO calculations

Owing to simple geometrical properties of the chromium lines sample (constant height and only horizontal and vertical interfaces), a limited number of ray paths is required for the calculations. Indeed, for a given incident radiation direction, the refraction into the chromium structure can be realized only in two manners – on the horizontal or the vertical interface. Thus, at a given fluorescence spot we can consider only four final ray path directions: two ray path directions (up and down) for incident radiation reaching the structure from the horizontal interfaces, and two ray path directions (up and down) for incident radiation reaching the structure from the vertical interfaces. Consecutive ray paths arise due to the multiple reflections on horizontal interfaces of chromium lines – a given fluorescence point can be reached after 0, 1, 2, *etc.* reflections.

For excitation along the lines ($\vartheta = 0$) the ray tracing procedure is performed only for reflections on horizontal interfaces, thus the obtained result is equivalent to that of a closed Cr layer. For all the other tilt angles ($\vartheta \neq 0$) the computations were performed as for a sample with the chromium lines of a width $l = l_0 / \sin \vartheta$ and periodicity $p = p_0 / \sin \vartheta$.

The GO ray tracing reproduce both the particle-like and layer-like parts of the spectra (see [Figure IV.A.5.b](#)). In addition, the clearly visible structures above the critical angle of external total reflection at the substrate can be attributed to the modulations in the measured spectra.

IV.A-2.3 Intensity modulation

The positions of the intensity modulation maxima visible in the measured spectra and in the GO simulations can be calculated as the incident angle for which the number of possible ray paths is significantly higher than for other angles. Such a situation

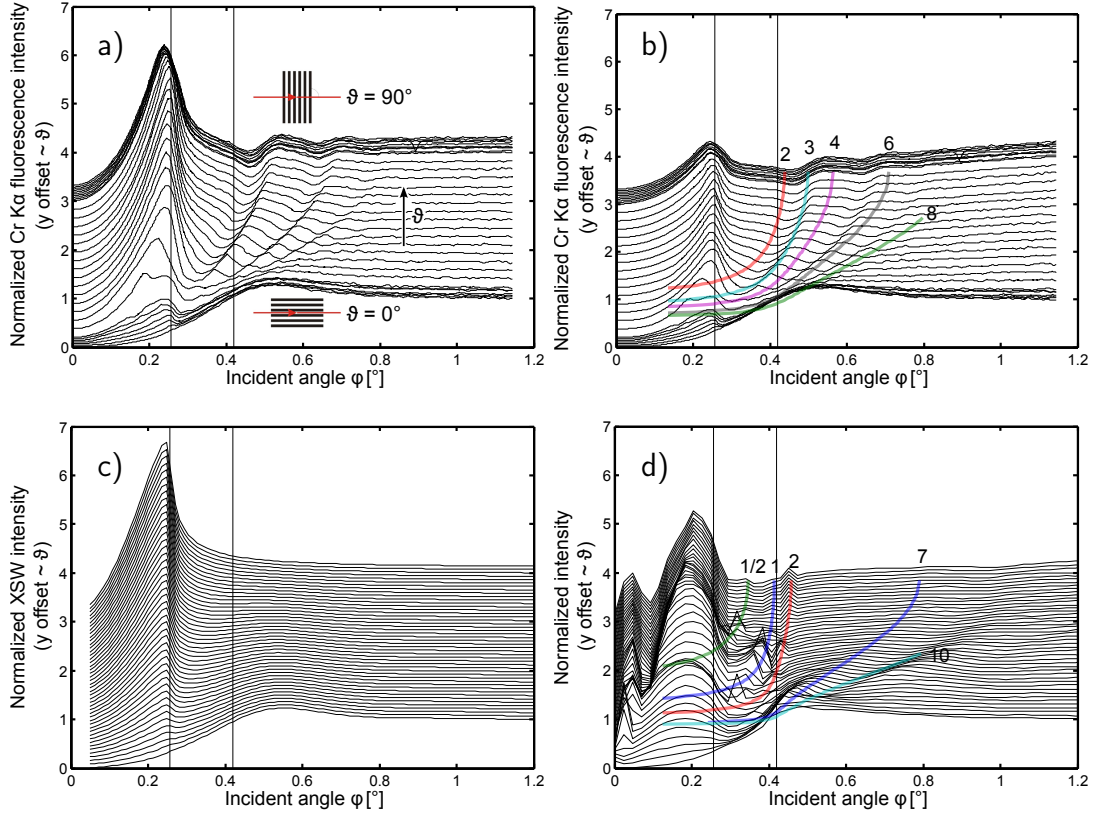


Figure IV.A.5: Comparison between the experimental [GIXRF](#) fluorescence intensity measured at an incident beam energy of 7 keV and the calculated excitation intensities according to the [XSW](#) and [GO](#) approaches. (a) Raw [GIXRF](#) angular profiles of Cr stripes; (b) [GIXRF](#) angular profiles of Cr stripes corrected for the effective flux of incident radiation; (c) [XSW](#) simulation as a linear combinations of 10 nm layer-like and 2 nm particle-like profiles; (d) [GO](#) ray tracing simulation. Colored eye guides in (b) and (c) stand for calculated intensity modulations positions corresponding to inscribed indexes. Black vertical lines represent the positions of φ_{Si} and φ_{Cr} critical angles.

can happen if multiple reflections can take place in a periodic structure (see [Subsection I-3.3.2](#) on page 23).

Equation (I.13) on page 23 gives the necessary condition for the intensity maxima to occur. Using (I.14) and substituting p with $p_0/\sin\vartheta$ we can write this condition as follows:

$$\varphi_M = \arccos \left\{ n_{Cr} \cos \left[\arctan M \frac{h \sin \vartheta}{p_0} \right] \right\}, \quad M \in \mathbb{Q}_+. \quad (\text{IV.A.1})$$

Thus the oscillations positions can be calculated directly from the refractive index n_{Cr} , height h and period p_0 of the Cr structure, and the angle of surface orientation ϑ . Though, as seen in the presented measured data and the [GO](#) simulations not all of the calculated maxima positions are visible (see [Figure IV.A.5.b](#) and [Figure IV.A.6](#)). This can be attributed to more complicated interference effects. Nevertheless, for the [GEXRF](#) and [GIXRF](#) measurements the modulations with the same indexes M are observed. This is not the case, however, for the [GO](#) calculations for which the noticeable modulations, thought present, do not correspond to the measurement.

As already stated, in the measured spectra the oscillations are clearly visible. However, in order to completely reproduce their positions from (IV.A.1) an additional attenuation factor β' had to be introduced in the expression for the refractive index:

$$\tilde{n} = n + i\beta'. \quad (\text{IV.A.2})$$

The factor β' was found to be $5 \cdot 10^{-6}$ both for [GIXRF](#) and [GEXRF](#) measurements. We attribute this additional component to the radiation scattering on the rough interfaces of the structure.

The final refractive indexes used for the calculation were:

$$\begin{array}{lcl} \delta & & \beta \\ \tilde{n}(7 \text{ keV}) & = 1 + 2.6956 \cdot 10^{-5} - i(3.5512 \cdot 10^{-6} + \boxed{5 \cdot 10^{-6}}) \\ \tilde{n}(\text{Cr K}\alpha) & = 1 + 4.2655 \cdot 10^{-5} - i(1.0775 \cdot 10^{-6} + \boxed{5 \cdot 10^{-6}}). \end{array}$$

The values for δ and β were taken from [3].

IV.A-2.4 Effective flux correction

Due to the simple sample geometry the calculation of the effective flux correction (see [Sub-chapter III.D](#) on page 87) can be done explicitly. For a striped structure of height h , length l and period p the structure cross-section can be calculated in the following way. The radiation reaching the structure at the top interface is equal to l/p of the total flux impinging on the sample. The radiation directly reaching the structure at

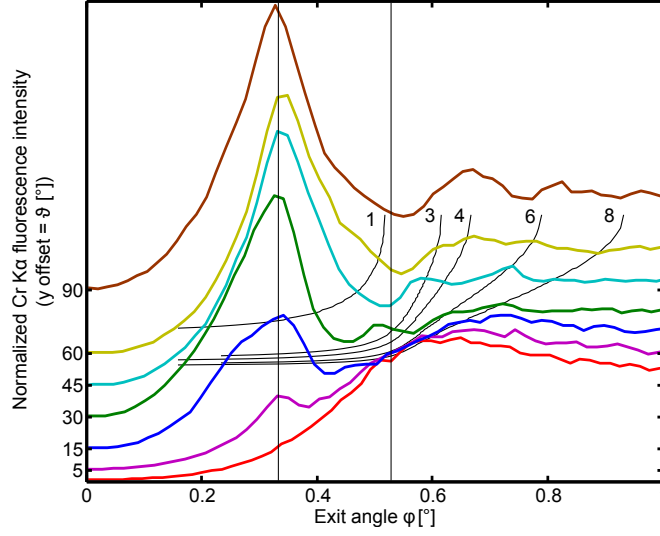


Figure IV.A.6: GEXRF profiles of the sample with Cr stripes. Eye guides stand for the calculated intensity modulations positions corresponding to inscribed indexes. Black vertical lines represent the $\varphi_c(Si)$ and $\varphi_c(Cr)$ positions.

the side interface makes $h \cot(\varphi)/p$ of the total flux. Exactly the same fraction makes the radiation reaching the structure after reflection on the support. Thus, taking into account that with ϑ the effective structure length and the period should be scaled with $1/\sin \vartheta$, the structure cross-section can be given by the following formula:

$$\sigma = \begin{cases} \frac{(l_0/\sin \vartheta + 2h \cot \varphi)}{p_0/\sin \vartheta} & \text{if } \varphi > \arctan \frac{p_0 - l_0}{2h \sin \vartheta} \\ 1 & \text{else.} \end{cases} \quad (\text{IV.A.3})$$

As can be seen in [Figure IV.A.5](#) on page 99 the effective flux correction significantly changes the [GIXRF](#) profiles. Most noticeable is the reduction of the particle-like region of the spectra. Also the slope of the spectra above the φ_{Cr} corresponds better to the one of [GO](#) calculations.

IV.A-3 Cr trapezoidal prisms

The sample (see [Subsection II.C-2.3](#) on page 53) was measured only with the [GEXRF](#) technique. The measurements were performed for various positions of the beam spot on the structure in order to investigate the variation of the [GEXRF](#) profiles as a function of the prism width while keeping the structure period fixed. All the measurements were performed for the same sample surface orientation for which the detected radiation propagates across trapezoidal prisms.

IV RESULTS AND DISCUSSION

The results presented in the left panel of [Figure IV.A.7](#) demonstrate a strong dependence of the [GEXRF](#) profiles on the prism width.

The most visible changes concern the region in between the critical angle of the support φ_{Si} and of the structure φ_{Cr} material. At φ_{Si} a peak characteristic for particle-like profiles appears. Around φ_{Cr} the intensity increases creating a characteristic intensity valley between critical angles. The depth of the valley decreases with the prism width. For wide prisms the particle-like peak is not visible; however the [GEXRF](#) intensity below φ_{Cr} is still increased with respect to the calculated layer-like profile.

Effects of multiple reflections (see [Subsection I-3.3.2](#) on page 23) can also be seen. The blue lines in [Figure IV.A.7](#) represent positions of the modulations calculated with the modified refractive index $\tilde{n} = n + i\beta'$ as defined in [Subsection IV.A-2.3](#) on page 98. Interestingly, the intensity modulations with the same indexes M are visible as for the sample with Cr stripes.

IV.A-3.1 GO ray tracing simulations

The [GEXRF](#) spectra were simulated with the ray tracing method as described in [Subchapter III.C](#) on page 79. Similarly as for the Cr stripes (see [Subsection IV.A-2.2](#) on page 98) the simple geometry of the trapezoidal prisms structure facilitates the calculations. The number of ray paths directions required for the calculations is limited only to rays leaving the structure from the horizontal and vertical interfaces. In order to better represent the measurement the simulations were performed with an additional parameter of the surface [rms](#) roughness (see [Subsection III.C-3.1](#) on page 81) of 1 nm. The results of the simulations are presented in the right panel of [Figure IV.A.7](#).

Even though the [GO](#) simulations do not reproduce precisely the measured data the main trends are correctly represented. We can observe a very similar evolution of the intensity valley between the critical angles of total reflection φ_{Si} and φ_{Cr} . The variation of the intensity modulations due to multiple reflections is also similar.

For wider prisms the simulations most significantly differ from the measurements around φ_{Cr} . This difference can be attributed to the limited optical paths coherence (see [Subsection III.C-3.3](#) on page 85) that has not been considered in the present simulations.

The simulated intensity evolution below φ_{Si} does not coincide with the measurement neither. The sharp peak around 0.5° is a computation accuracy artefact and has no physical meaning. However, the effect of consecutive prism shadowing is not well represented because the particle-like peak maximum position is shifted to lower exit angles being closer to the one for a fully particle-like structure. This might be due to the non negligible surface roughness that suppresses the coherent x-ray reflection and that could result in the sharpening of the particle-like structure in the measured signal.

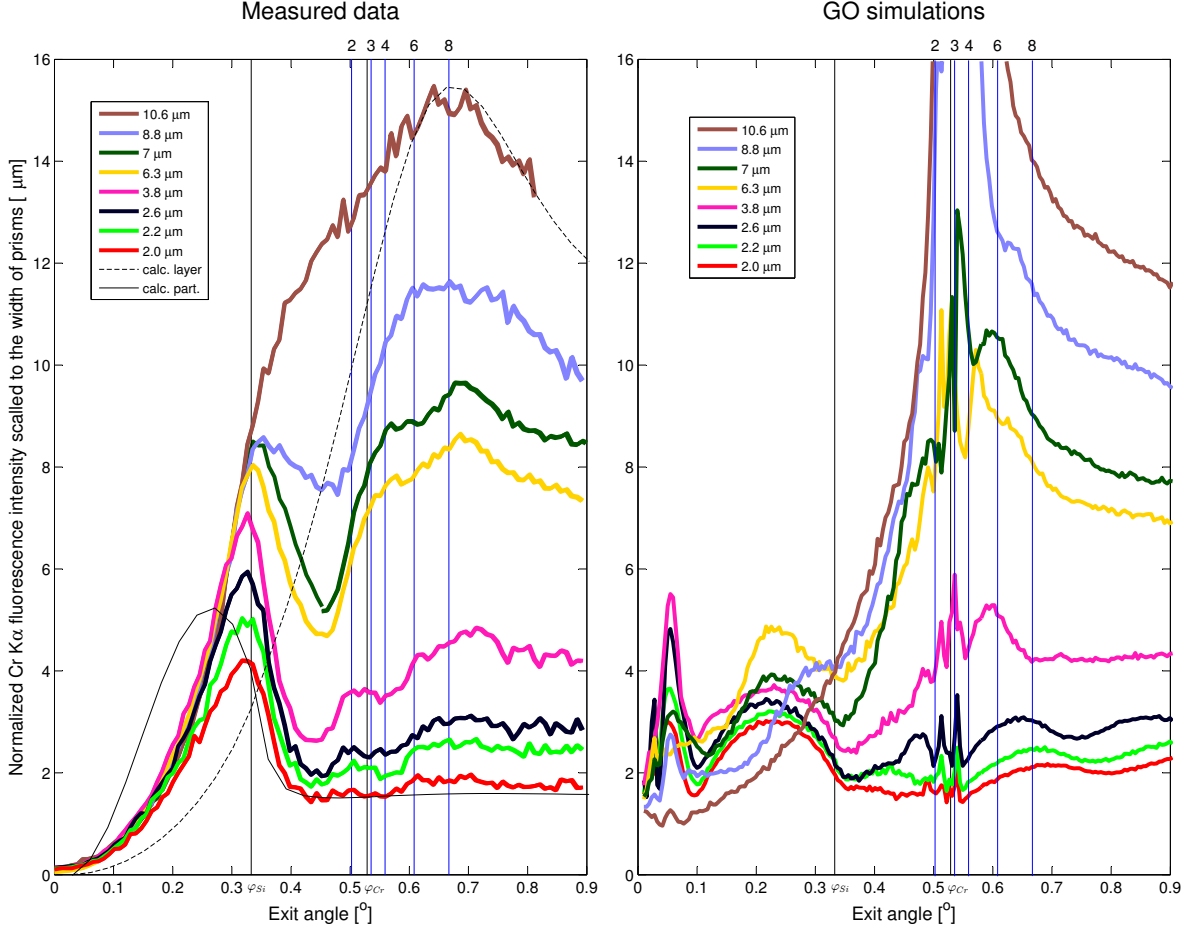


Figure IV.A.7: **GEXRF** profiles of the sample with Cr trapezoidal prisms. **GO** calculations performed including 1 nm **rms** roughness are shown in the right panel. The fluorescence intensity is normalised and scaled to the prism width. Black dashed line: calculated profile of a 10.7 nm Cr layer scaled to the intensity of a 10.6 μm wide prism. Black solid line: calculated profile of a 10.7 nm Cr particle scaled to the intensity of a 2 μm wide prism. Vertical lines correspond to the following: blue – intensity modulations positions corresponding to labeled indexes calculated with the modified refractive index (see text); black – critical angles for Si and Cr.

IV.A-4 Samples with plane symmetries

Samples with plane symmetries (described in [Subsection II.C-2.4](#) on page 53 and [Subsection II.C-2.5](#) on page 54) were measured with the [GEXRF](#) technique at [ESRF](#) and [SLS](#). All samples were installed on the piezo target holder (see [Subsection II.A-2.2](#) on page 33) to allow measurements for different angles ϑ of the sample surface orientation. Special attention was paid to align the chips of the investigated structures in the center of the rotor.

IV.A-4.1 Cr disc samples

The results of the Cr discs [GEXRF](#) measurements are presented in [Figure IV.A.8](#). For all the samples the [GEXRF](#) profiles differ noticeably for different ϑ values. The most pronounced changes are visible around φ_{Cr} and above. These differences are caused by positions of the intensity modulations (see [Subsection I-3.3.2](#) on page 23) which change with the structure periodicity along the direction imposed by the sample surface orientation.

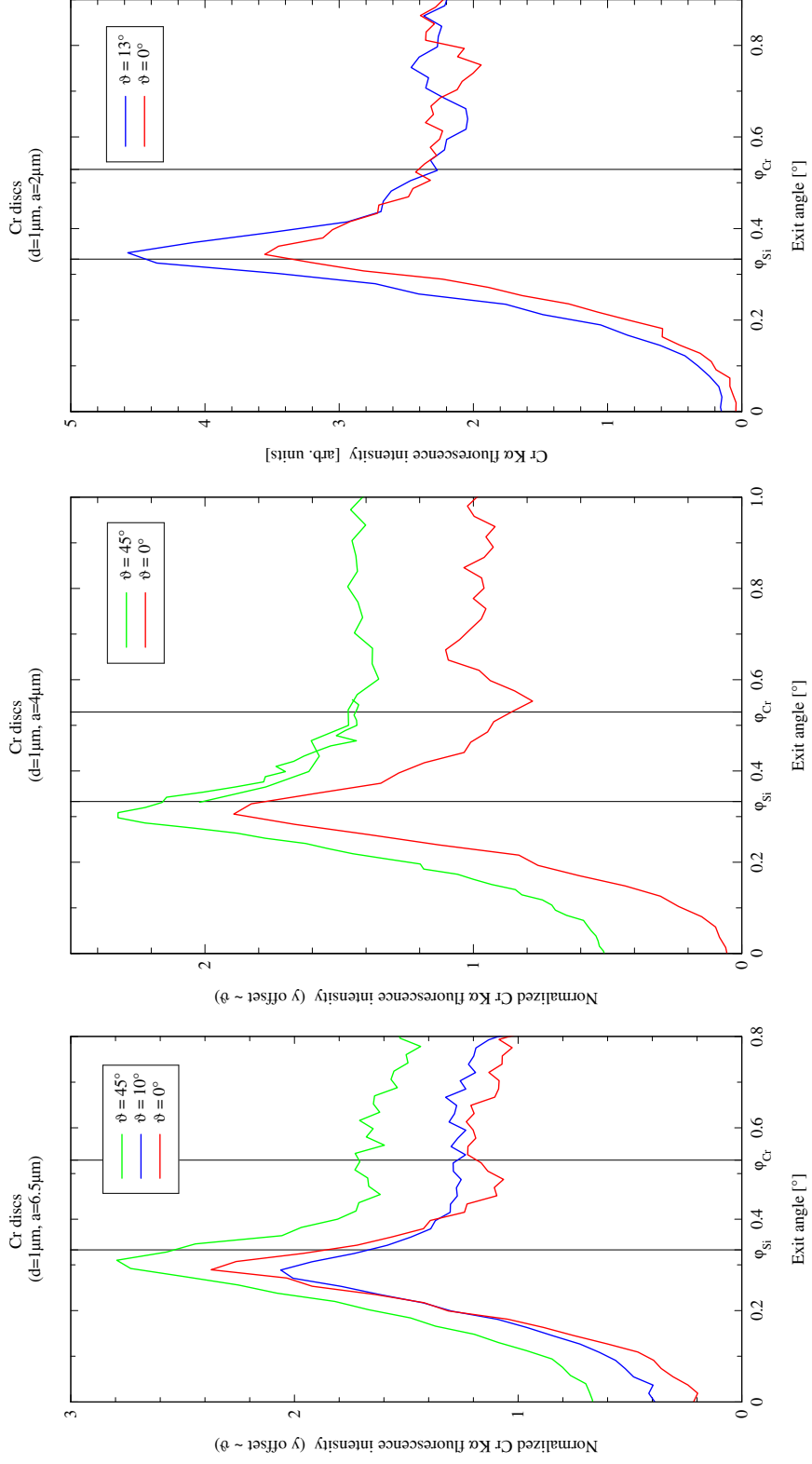
IV.A-4.2 Co/Ni discs sample

In [Figure IV.A.9](#) on page 106 the [GEXRF](#) profiles of the Co/Ni disc structures detected for both the Co and Ni $K\alpha$ lines are presented. The comparison of the [GEXRF](#) calculations with the signal from the Co/Ni bilayer confirm the sample fabrication parameters *i.e.* a 3 nm Co layer superposed on a 3 nm Ni layer.

Cobalt and nickel have very similar refractive indexes for both the Co and Ni $K\alpha$ fluorescence lines (see [Table IV.A.1](#)). Thus, the refraction and reflection phenomena on their interfaces are very small and can be neglected. Simplifying, the Co and Ni [GEXRF](#) signals from Co/Ni discs can be regarded as the signals from the top and the bottom parts of an optically uniform disc.

			δ		β
Co $K\alpha$	n_{Co}	$= 1 +$	$2.6639 \cdot 10^{-5}$	$- i$	$5.6724 \cdot 10^{-7}$
	n_{Ni}	$= 1 +$	$2.9329 \cdot 10^{-5}$	$- i$	$6.7736 \cdot 10^{-7}$
Ni $K\alpha$	n_{Co}	$= 1 +$	$3.2504 \cdot 10^{-5}$	$- i$	$7.5241 \cdot 10^{-7}$
	n_{Ni}	$= 1 +$	$3.4715 \cdot 10^{-5}$	$- i$	$9.0584 \cdot 10^{-7}$

Table IV.A.1: Comparison of n_{Co} and n_{Ni} refractive indexes for energies corresponding to Co $K\alpha$ (6.93 keV) and Ni $K\alpha$ (7.48 keV) fluorescence lines.

Figure IV.A.8: [GEXRF](#) profiles of different p4m Cr disc patterns.

IV RESULTS AND DISCUSSION

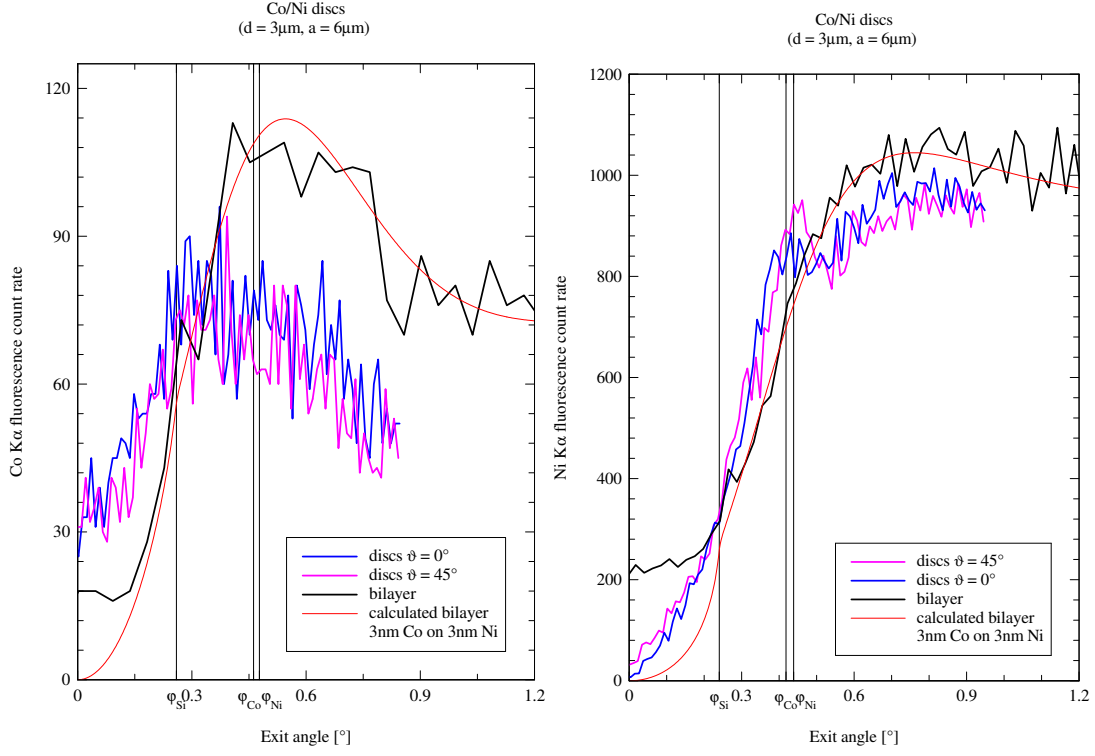


Figure IV.A.9: Co K α (left panel) and Ni K α (right panel) GEXRF profiles of the Co/Ni disk pattern (blue and violet lines). The corresponding experimental (black lines) and theoretical (red lines) GEXRF profiles of a calibration sample consisting of a Co/Ni bilayer (thickness of 3 nm for each layer) are also depicted.

Looking at these GEXRF profiles one can see that relatively to critical angles of the support (φ_{Si}) and discs materials (φ_{Co} and φ_{Ni}) the first intensity peak appears at a different position. In fact, the Co profile exhibits an intensity growth at φ_{Si} which correspond to a particle-like signal and the Ni profile at $\varphi_{Co}/\varphi_{Ni}$ which can be attributed to intensity modulations caused by multiple reflections. From that we can draw a conclusion that the particle-like part of the signal is created only by the top part of the disc structure, whereas the multiple reflections in the structure are more likely to happen for the bottom part. For the Ni K α signal we can see similar changes of the intensity modulation at $\varphi_{Co}/\varphi_{Ni}$ as for the Cr discs structures at φ_{Cr} (see Figure IV.A.8).

IV.B Evenly distributed structures

IV.B-1 NaCl nanostructures

The NaCl structures were investigated with the [GIXRF](#) technique. The obtained results for the NPRA0053 sample (see [Subsection II.C-1.2](#) on page 51) are presented in [Figure IV.B.1](#).

In order to obtain the particle size and size distribution of the NaCl nanoparticles [SEM](#) images (see [Figure II.C.1](#) on page 51) of the sample were evaluated. Although these [SEM](#) images do not give explicit information on the structures height, the height of the particles was assumed to be equal to the square root of the area occupied by the individual particles. Such an assumption is justified assuming the uniform growth of the NaCl nanocrystals in all three dimensions – length, width and height.

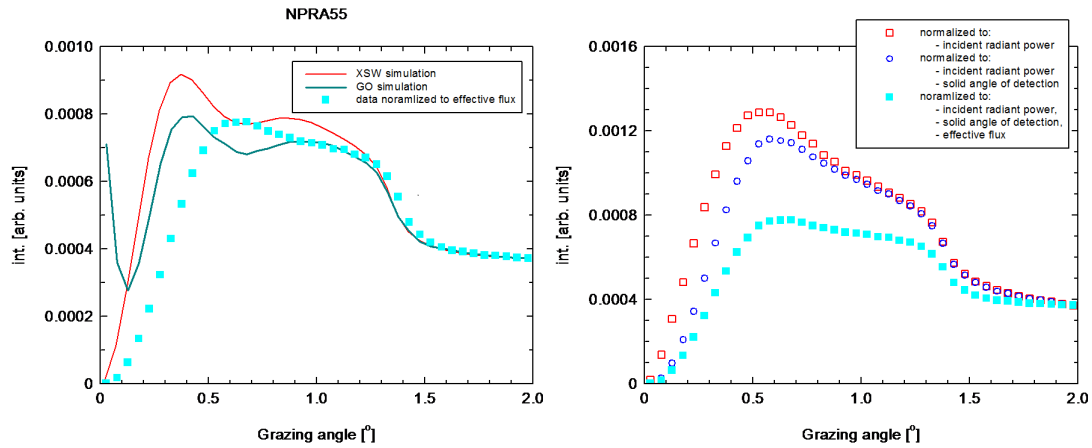


Figure IV.B.1: [GIXRF](#) profile of the NPRA0053 sample with NaCl nanostructures measured with an incident beam energy of 1260 eV. Left: normalized [GIXRF](#) intensity (blue squares) together with the [XSW](#) (red line) and [GO](#) (green line) simulations. Right: Subsequent steps of intensity normalization – incident radiation power (red squares), solid angle of detection (dark blue circles), effective flux (light blue squares).

IV RESULTS AND DISCUSSION

To properly analyze the data an appropriate normalization of the [GIXRF](#) intensity was necessary. In the right graph of [Figure IV.B.1](#) the three consecutive normalisation steps are presented:

- normalisation for the incident radiation power,
- normalisation for the solid angle of detection (see [Sub-chapter II.B](#) on page 43),
- normalisation for the effective flux (see [Sub-chapter III.D](#) on page 87) calculated from the particle size distribution from the [SEM](#) image.

It should be noted that normalisation for the effective flux most significantly affects the intensity profile.

Using the particle size distribution from the [SEM](#) images the [GIXRF](#) profile was calculated with both [XSW](#) and [GO](#) methods (see left panel of [Figure IV.B.1](#)). The [XSW](#) curve was obtained from the linear combination of weighted [XSW](#) simulations performed for particle sizes corresponding to the given size distribution.

One can first see that the overall shapes of the angular profiles corresponding to the two simulations are similar. It seems further that the experimental data are slightly better reproduced by the [GO](#) calculations, particularly above 0.9° where an excellent agreement is observed. For lower angles, however, there are some significant differences. There could be three reasons for the discrepancy between the measured [GIXRF](#) profiles and the [GO](#) and [XSW](#) simulations:

- the roughness of the substrate surface that was not taken into consideration in the simulations and could additionally disturb the x-ray reflection at shallow angles;
- the nonuniform NaCl crystal growth that would result in a different height distribution and
- the difficulties encountered at small incidence angles with the normalization of the fluorescence intensity.

IV.B-2 Fe and Cr layers of various roughnesses

In [Figure IV.B.2](#) the [GEXRF](#) profiles of several samples (922C, 923C, 926C, 922B, 926C – see [Table II.C.1](#) on page 50) with Fe and Cr layers of a nominal thicknesses of 5 nm are presented.

The [GEXRF](#) intensity of a layer measured at angles above the critical angle is proportional to the number of investigated atoms in the layer, and thus corresponds to the overall amount of the deposited material. Even though the nominal thickness

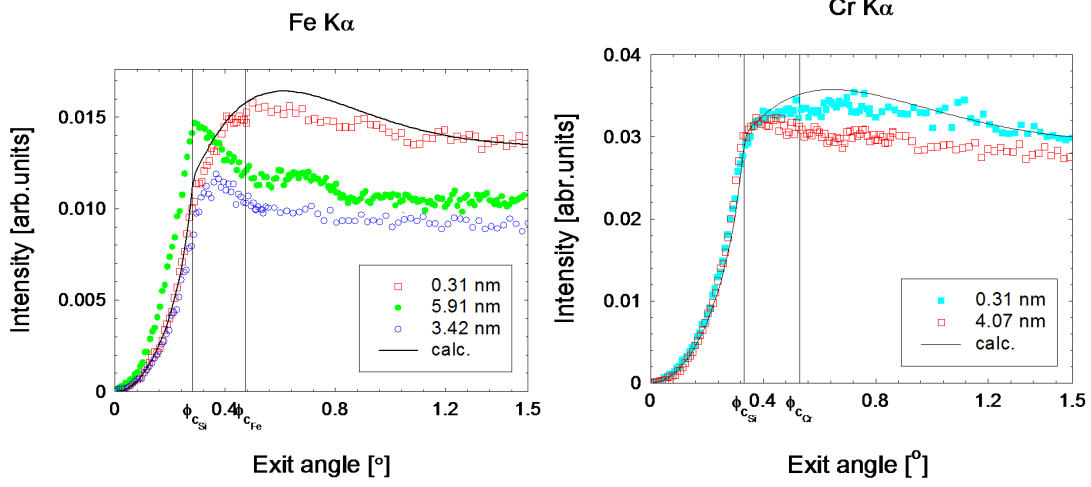


Figure IV.B.2: **GEXRF** profiles of 5 nm Fe (right) and Cr (left) layers of different roughnesses. Calculated curves of flat 5 nm layers are plotted with black lines. In the legend the **rms** roughnesses of the layers are indicated.

of all layers was expected to be constant, an intensity variation of $\sim 15\%$ can be seen at 1.5° .

For both cases of Fe and Cr, significant differences in the **GEXRF** profiles for the flat and rough layers are visible. All rough samples exhibit a more pronounced intensity peak in the proximity of the critical angle for the support material φ_{Si} . Such a peak is characteristic for very thin layers. For exit angles larger than the critical angle for the layer material (φ_{Fe} , φ_{Cr}) an additional intensity bump is visible.

IV.B-2.1 Application of sample morphology models

In **Figure IV.B.3** on page 111 four different models for the samples morphology are applied to the **GEXRF** profile of the most rough sample – 922C – with the Fe layer roughness **rms** of 5.91 nm.

Nevot-Croce model

In the Nevot-Croce model [33] the effect of the roughness is calculated with the distorted-wave Born approximation. Thus the roughness is considered as a small perturbation of a electromagnetic potential with a Gaussian random distribution along an interface.

In the Nevot-Croce model, as compared to a smooth surface, both the reflectivity r and transmission t coefficients are modified as follows:

$$\begin{aligned}\tilde{t} &= t \cdot \exp\left(\frac{-(k_y - k'_y)^2}{2} \sigma_h^2\right), \\ \tilde{r} &= r \cdot \exp\left(-k_y^2 \sigma_h^2\right),\end{aligned}$$

IV RESULTS AND DISCUSSION

where k_y and k'_y correspond to the incident and refracted wave vectors components perpendicular to the sample surface, respectively, and σ_h^2 is the variance of the Gaussian distribution of a potential.

Stack of layers of various density

The rough interfacial region can be described as a transition layer in which the refractive index varies continuously with the depth. The interface can be then divided into elementary layers in which the refractive index depends on the roughness distribution.

Linear combination of layers of different thicknesses

If the correlation length of the height distribution is large enough, the resulting GEXRF profile can be approximated by the sum of GEXRF curves for layers of various thicknesses.

GO ray tracing

Providing the wavelength of the exciting radiation is much smaller than the size of the grains of the structure, similarly as for the previously described samples, a ray tracing method described in Sub-chapter III.C on page 79 can be applied to rough layers. In order to meet the requirement of only vertical and horizontal interfaces the layer morphology measured with the AFM was approximated by a composition of rectangular prisms.

The AFM imaging technique has been used to obtain all roughness parameters needed for the simulations. However, the AFM does not give all the information about the measured samples, thus several assumptions had to be made:

- the morphology measured with the AFM is representative for the whole surface,
- the AFM height profiles are exact,
- the optical density of the structure components is the same as the one of the bulk.

The Nevot-Croce and stack of layers of various density models fail to correctly reproduce the intensity profiles. This is not surprising as both methods can be used only for relatively small roughnesses.

In contrast to previously presented data the GO ray tracing model does not give even comparable results. Most probably this is due to the simplicity of the proposed model in which the layer morphology approximation by rectangular prisms does not take into account the curvature of the sample surface.

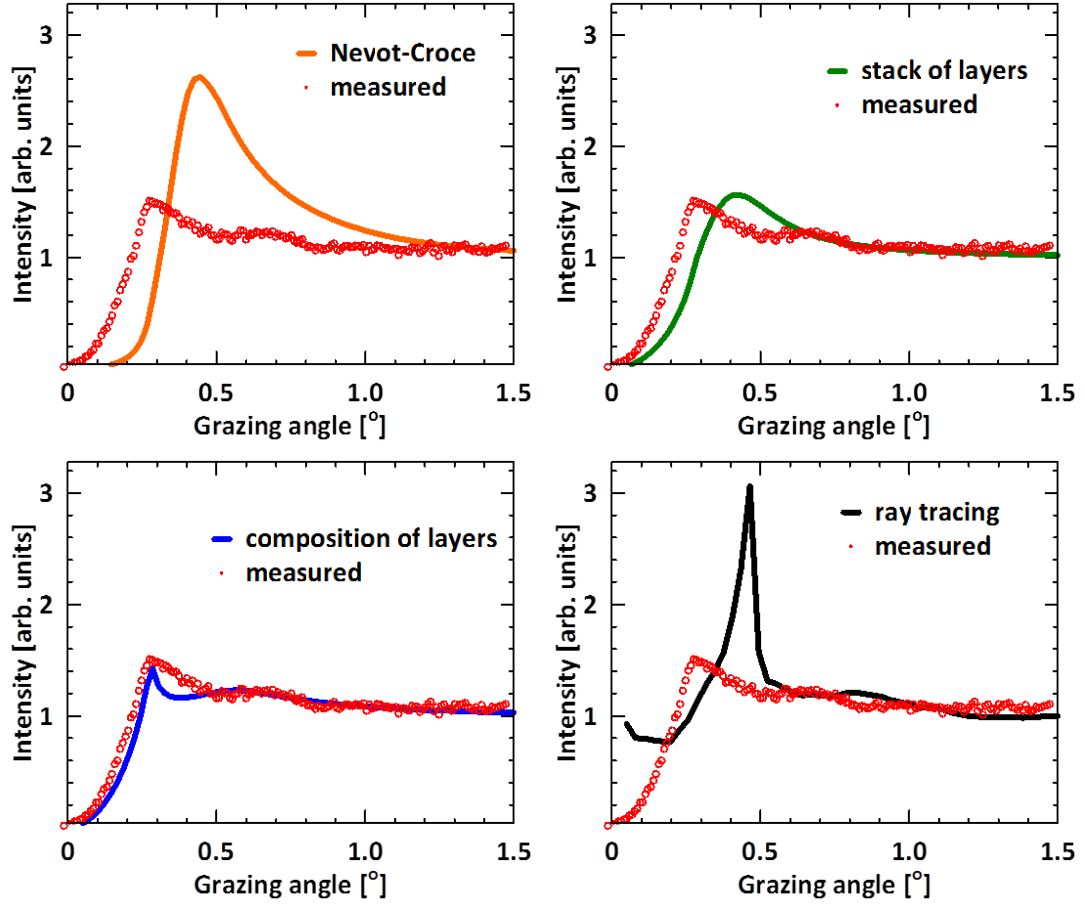


Figure IV.B.3: Different roughness models applied to GEXRF profiles of the 5 nm Fe layer with a 5.91 nm rms roughness.

From simulations presented in Figure IV.B.3 only a simulation employing a linear combination of layers of different thicknesses can be used to represent the intensity profile trends of the measured GEXRF data. The simulated profile exhibits both intensity bumps present in experimental data.

However, the simulated peak around φ_{Si} is too narrow. This difference could be attributed to the grainy character of the simulated layers since the model considers only layers of different density neglecting the particle-like contributions. In comparison with the data collected for Cr trapezoidal prisms (see Section IV.A-3 on page 101) one could expect an intensity increase in the region between the critical angles of the support and the deposited materials.

IV.B-3 Samples with Co and Ni discs

Unfortunately, due to limited experimental beamtime the Co and Ni discs structures could not be investigated. However, calibration samples with the Co/Ni bilayer and the Co and Ni monolayers have been measured. Because all the samples have been produced within a single process flow the Co and Ni layers were assumed to have the

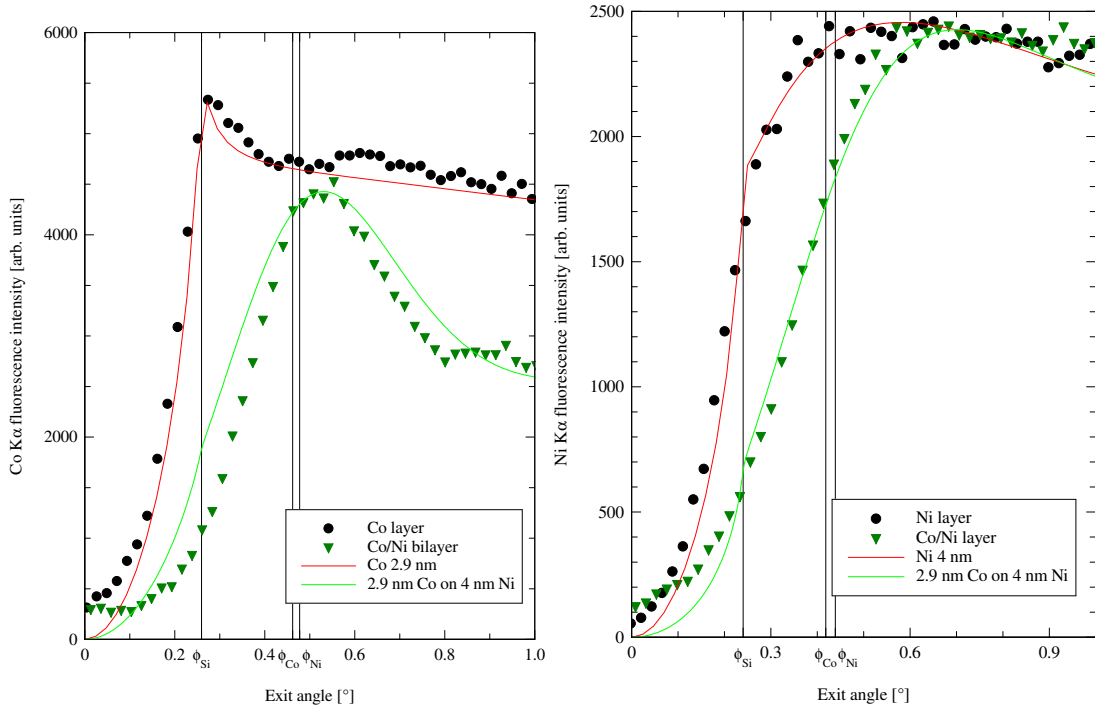


Figure IV.B.4: Co $K\alpha$ and Ni $K\alpha$ GEXRF profiles of the Co and Ni monolayers (black circles) and Co/Ni bilayer (green triangles) calibration samples fabricated together with the Co and Ni discs samples. Calculated profiles of the best fits with 2.9 nm Co and 4 nm Ni layers are plotted with solid lines.

same properties regardless the sample. Best fits of the [GEXRF](#) profiles were found for a Co layer of 2.9 nm and a Ni layer of 4 nm.

In [Figure IV.B.4](#) the Co and Ni $K\alpha$ [GEXRF](#) profiles and the corresponding calculations are presented. It can be seen that in the case of Ni fluorescence the experimental profiles are very well reproduced by the present calculations. For the Co fluorescence the calculated profiles are in satisfactory agreement; however, they do not match as well the experimental data. In principle, in the case of the Co layer an excess in the measured intensity with respect to the calculations can be seen beyond $\varphi_{Co}/\varphi_{Ni}$ for angles between 0.6° and 0.8° . A similar feature in the profile was observed for rough Cr layers presented in [Section IV.B-2](#) on page [108](#). As already mentioned in [Subsection II.C-2.5](#) on page [54](#) the Co layer was deteriorated during the lift-off process and thus most probably cannot be characterized as a pure layer-like structure.

IV.C Remarks on experimental difficulties

During data acquisition and subsequent data processing several issues needed to be solved. In the following the most significant ones that were encountered during the [GEXRF](#) measurements will be presented.

IV.C-1 Exit angle calibration

Correct calibration of the exit angle scale is an important aspect for the [GEXRF](#) data interpretation. In the simplest case when the structure geometry allows the numerical fitting of the [GEXRF](#) signal the exit angle calibration can be achieved by adding the exit angle shift to the fit parameters. Unfortunately, this is not feasible for more complex structures. For that purpose several different methods listed below can be used. However, they are hardly straightforward procedures. Practically, the final exit angle data can be vitiated by an error of up to $\sim 0.1^\circ$.

IV.C-1.1 Calibration from the spectrometer corrections

A very important aspect of the exit angle calibration is a proper correction of [CCD](#) images (see [Sub-chapter III.B](#) on page 71). The latter defines the shift of the exit angle across a single [CCD](#) image well-posing the problem of the definition of the detected exit angle (see [Appendix F](#) on page 169). Moreover, a proper correction for the von Hamos spectrometer parameters should also give a proper exit angle calibration.

Unfortunately, the spectrometer parameters correction procedure presented in [Appendix E](#) on page 161 is insensitive to displacements of a TAL motor which is responsible for the exit angle variation (see [Subsection II.A-1.2](#) on page 29). Knowing that the reproducibility of the exit angle between consecutive target holder mounts may amount up to $\sim 1^\circ$ an additional method to ensure absolute exit angle values appears necessary.

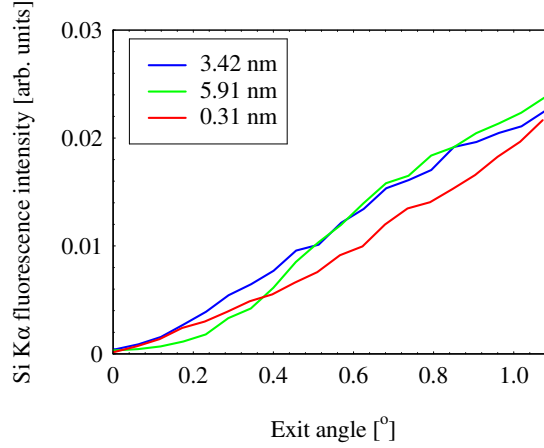


Figure IV.C.1: Si K α GEXRF profiles from Si supports of thermally evaporated 5 nm Fe structures of different rms roughnesses (see Subsection II.C-1.1 on page 49). Although the nominal structure thickness is the same for all the samples, the profiles are significantly different and cannot be used for exit angle calibration.

IV.C-1.2 Calibration to the support material

Even if the GEXRF profile of an investigated structure cannot be easily simulated chances are that this is not the case for the structure support. In such a situation the exit angle correction for the GEXRF signal can be found from the support material and then applied to the examined structure itself.

Such a operation is most reliable if both materials can be measured with the same Bragg crystal as the spectrometer parameters corrections may considerably differ in the opposite case hindering the procedure. Care should also be taken if the GEXRF signal is measured from the support material covered with the investigated structure – as well in such a situation the correct fit may be difficult to obtain (see Figure IV.C.1).

IV.C-1.3 Calibration to the reference structure

In certain cases the investigated samples structural organization permits inclusion of an additional calibration layer (this was the case for stencil made samples, see Subsection II.C-2.4 on page 53). This is the most comfortable situation as the calibration measurement can be performed in nearly the same conditions.

IV.C-1.4 Calibration with the spectral background

This is the less elegant, however, yielding good results method. The GEXRF does not vanish completely below the critical angle position. In fact, it usually grows exponentially from 0°. Thus, the principle of this method is to find where the GEXRF signal

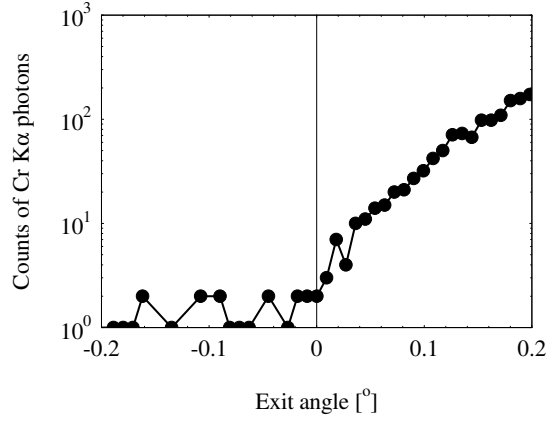


Figure IV.C.2: An example of a Cr K α GEXRF profile with exit angles calibrated with the spectral background.

rises from the background level (see Figure IV.C.2). Of course this procedure can be applied only if the background conditions are very good and the experiment statistics is high.

IV.C-2 Background extraction

As already stated in Sub-chapter III.A on page 61 the CCD energy discrimination is a very effective tool to decrease the spectral background. During the experiment we have encountered a situation when the scattered background radiation in the spectral

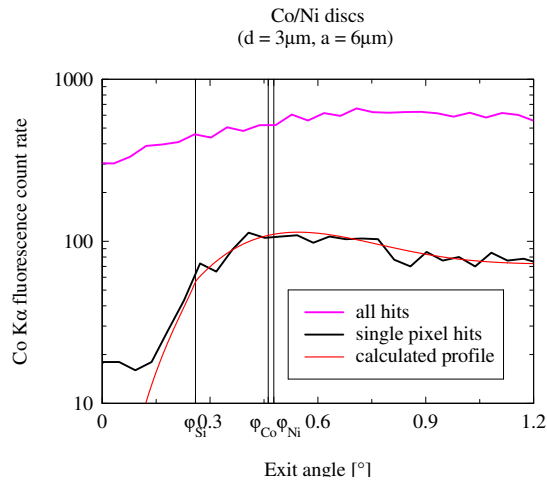


Figure IV.C.3: Scattered background discrimination with a proper background events definition. An example of the Co K α GEXRF profile of the Co/Ni discs sample (see Subsection II.C-2.4 on page 53).

range corresponding to the measured fluorescence line was reaching the CCD detector through an unsealed shielding and thus affected the measured GEXRF profile (see Figure IV.C.3). The actual profile was resolved by counting only the events within the single pixel event energy window.

IV.C-3 Synchrotron radiation beam instabilities

The GEXRF measurements rely on the stability of the exciting radiation. Most preferably the excitation should be constant during the whole scan of the GEXRF profile. Such conditions were ensured in SLS due to the top-up injection, and effective cooling and mechanical isolation from the vacuum chamber of the mirrors supports at the SuperXAS beamline (see Section II.A-4 on page 38).

At the ESRF the storage ring is refilled in average every 12 hours. This results in a saw-like characteristics of the storage ring current with an exponential decay between the refills. In principle, the synchrotron radiation intensity should follow the trend of the current evolution, but there are large deviations up to 20 % that cannot be explained by the current change (see Figure IV.C.4). The origin of these beam intensity variations is not clear but it can be attributed to some thermal drift of the beamline optics components.

In order to deal with such changes of the incident flux one could scale the acquired fluorescence lines intensities with the intensity of the synchrotron radiation beam. However, the ID21 beamline setup did not allow a constant primary beam intensity control. Thus, in order to get reliable data the intensity measurements were performed at the

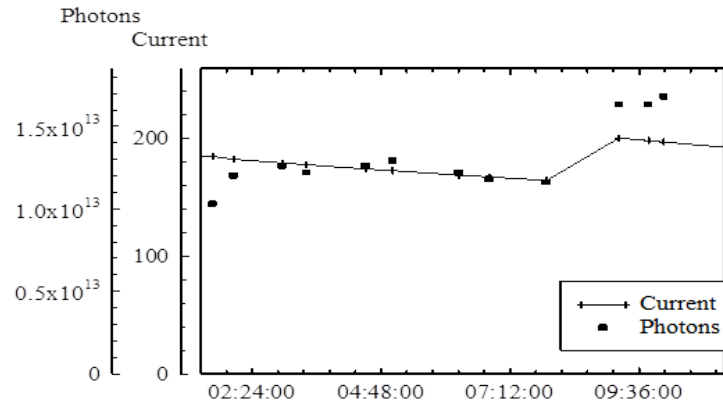


Figure IV.C.4: Beam intensity measured at the ESRF ID21 beamline superposed with the ring current. Beam intensity evolution was measured with exactly the same beam-line setup.

beginning and at the end of the [GEXRF](#) scans; the intensity during the scan was linearly interpolated.

IV.C-3.1 Beam spot position

The beam spot position on the sample is a very important factor in [GEXRF](#) measurements for two reasons. Firstly, in order to get the pure signal the beam spot should be centered on the investigated structure. Secondly, the displacement of the beam spot position changes the geometrical configuration of the [GEXRF](#) measurement (see [Sub-chapter III.B](#) on page 71) that can result in changes of the exit angle calibration.

During measurements the beam spot position changes were mainly caused by two factors: synchrotron radiation beam instability and slits/pinhole change.

Chapter V

Concluding remarks

V-1 Grazing angle x-ray fluorescence from surface nanostructures

In the following the overall characteristics of the surface nanostructures' XRF angular profiles based on experimental results and related GO simulations are presented.

Structures consisting of small elements that are scattered over the surface have clearly particle-like angular profiles. An increase in the lateral dimensions of the structure elements leads to attenuation of the particle-like signal in φ_c region and to appearance of a layer-like component as a result of x-ray propagation in individual elements of the structure. These features are well known and have been described formerly.

Additional effects appear for dense particles' distributions due to x-ray radiation propagation through several structures' elements. Two types of such effects can be distinguished. First, as a result of shadowing of consecutive structure elements for small grazing angles the detected XRF intensity is reduced (for instance see Section IV.A-1 on page 93 and Section IV.B-1 on page 107). This effect is more pronounced for high and dense structures. Another consequence of the compact elements' distribution is that x-ray radiation can be reflected multiple times in consecutive structures' elements. As a result, for certain grazing angles the number of ray paths reaching a given fluorescent atom is significantly higher (see Subsection I-3.3.2 on page 23) leading to an increased excitation (GIXRF) or detection (GEXRF) probability. For periodic structures this gives rise to characteristic intensity modulations appearing for grazing angles for which the number of ray paths is the most numerous. This effect is clearly visible for most of the results presented in Sub-chapter IV.A on page 93.

In case of dense evenly distributed structures the effect of multiple reflections is less systematic. Nevertheless, a significant intensity increase can be seen in the region between the critical angles for total reflection of the support and structure materials (see Section IV.B-2 on page 108 and Section IV.B-3 on page 112). As presented in Subsection IV.B-2.1 on page 109 such an effect cannot be explained with standard simulation methods; this is clearly a result of consecutive structure's element interactions. In fact, a very similar intensity growth in that region is observed for densely distributed periodic structures (see Section IV.A-3 on page 101). Above the critical angle of total reflection of the structure material the evenly distributed systems exhibit also a second region of intensity increase. Simulations show (see Subsection IV.B-2.1 on page 109) that this intensity growth can be attributed to the thickness variation of the elements of the structure.

V-2 GO ray tracing

For moderately dense structures the proposed GO ray tracing approach leads to very good results when compared to measurements and to the well-established models such

V CONCLUDING REMARKS

as [XSW](#). [GO](#) can handle the absorption and shadowing effects occurring on the nanostructured surfaces which are very difficult to simulate with other methods. Moreover, it is relatively easy to incorporate specific sample geometries into the [GO](#) calculations.

For very densely distributed structures the [GO](#) calculated spectra are rocketing around the critical angle of total reflection for the structure material (see [Figure IV.A.7](#) on page 103 and [Figure IV.B.3](#) on page 111). It can be presumed, however, that this is an effect of overrated optical ray paths coherence since the coherence length has not been implemented in the numerical calculations (see [Appendix D](#) on page 155) performed in this work.

It should be noted, that other methods such as [XSW](#) need no input about the sample geometry and with the available software [40, 64] simulations can be done very quickly. Thus, for standard situations where the surface morphology effects are not pronounced, the [GO](#) methodology would not compete with [XSW](#). Nevertheless, for the case of [GIXRF](#) measurements of particulate media (but also for buried implants *e.g.* in depth profiling) the correction for the effective photon flux, that also requires an initial input on the sample geometry, in general cannot be neglected.

[GO](#) is certainly a promising approach for samples with a known surface morphology for which the *a priori* knowledge of the structure can be thus verified. This approach can be also helpful in understanding uncommon [GEXRF](#)/[GIXRF](#) profiles of rough layers and grainy structures.

V-3 Perspectives

V-3.1 XRF quantification model

The existing grazing angle [XRF](#) quantification methods suffer from large uncertainties in the case of densely distributed nanoparticles. This is especially true for nanoparticles sampled directly from the aerosol phase and from dried liquid droplets – typical types of samples in environmental and medical researches. Densely packed nanodevices also pose similar problems. Thus new and more precise [XRF](#) quantification methods are of paramount importance.

Therefore, systematic [GO](#) simulations studies can significantly contribute to the development of more precise [XRF](#) quantification models for particulate media. Furthermore, for the [GIXRF](#) quantification, the effective photon flux corrections cannot be not neglected for neither the particulate media nor for buried implants *e.g.* in depth profiling.

V-3.2 Single shot GEXRF measurements

In high-resolution [GEXRF](#) technique the grazing emission conditions are achieved by turning the sample surface close to the emission direction defined by the Bragg angle of diffraction. Only x-rays hitting the crystal surface at the Bragg angle, defined by the energy of the x-rays and the lattice spacing of the crystal, can be diffracted towards the position-sensitive detector. Note that x-rays emitted from the source and fulfilling the Bragg condition span out on a cone and thus are emitted at slightly different exit angles (see [Section III.B-2](#) on page 72). This results in a deterioration of the grazing angle resolution when the position-sensitive detector is placed on the crystal focal plane. For proper [GEXRF](#) measurements a defocused setup with a [2D](#) detector should be used. In such a configuration an [2D](#)-image of a single fluorescence line on a position-sensitive detector corresponds to an intersection of a cone and has a characteristic “banana” shape where different sections of the “banana” correspond to different exit angles.

With an adequate spectrometer design, the spread of exit angles across the defocused image can be used for single shot measurements of [GEXRF](#) angular profiles. A proper operation of such a single shot [GEXRF](#) setup would significantly depend on the Bragg crystal quality and specifications. In particular, the crystal radius of curvature and reflectivity should be constant across the whole crystal.

V-3.3 Grazing emission x-ray absorption spectroscopy

[X-Ray Absorption Spectroscopy \(XAS\)](#) techniques are based on the measurement of the absorption coefficient by tuning the photon energy E across an absorption edge of an investigated element. The spectral features observed above the absorption edge – referred to as [X-ray Absorption Fine Structure \(XAFS\)](#) – reflect the molecular environment of a given absorbing atom and are related to the excitation cross-section of the core electrons into unoccupied electronic states or into the continuum. The chemical sensitivity of [XAS](#) spectra provides thus information about the different chemical states within systems having the same elemental composition.

Generally a [XAS](#) spectrum is divided into 4 energy regions, where E_0 is the absorption edge energy:

1. Pre-edge ($E < E_0$),
2. [X-ray Absorption Near Edge Structure \(XANES\)](#) , for incident x-ray beam energies $E = E_0 \pm 10$ eV,
3. [Near Edge X-ray Absorption Fine Structure \(NEXAFS\)](#) , for energies between 10 eV and 50 eV above the edge, and

V CONCLUDING REMARKS

4. [Extended X-ray Absorption Fine Structure \(EXAFS\)](#) , in the region from 50 eV up to 1000 eV above the edge.

In the pre-edge region there might be some minor features due to the electron transitions from the core level to high-lying orbitals (*e.g.* $s \rightarrow p$, or $p \rightarrow d$). In the [XANES](#) region, a sudden raise of absorption is observed. This is due to high probability transitions of core electrons to unbound levels with close energies. In [NEXAFS](#), the ejected photoelectrons have low kinetic energy ($E - E_0$ is small) and experience strong multiple scattering by the first and even higher coordination shells. In the [EXAFS](#) region, the photoelectrons have high kinetic energy ($E - E_0$ is large), and single scattering by the nearest neighboring atoms dominates.

X-ray absorption spectra can be measured in the fluorescent mode by recording the intensity of x-ray fluorescence transitions. In a Grazing Emission X-ray Absorption Spectroscopy (GE-XAS) measurement the incident photon energy is scanned across the absorption edge of interest and x-ray fluorescence detection is realized in the grazing emission geometry. Such an experimental configuration permits the use of [XAS](#) with all the [GEXRF](#) advantages, in particular: surface mapping, dose control and depth profiling.

Glossary

2D 2-dimensional. [31](#), [71](#), [73](#), [80](#), [88](#), [125](#)

3D 3-dimensional. [73](#)

ADXRF Angle Dependent X-Ray Fluorescence. [17](#)

AFM Atomic Force Microscopy. [50](#), [51](#), [54](#), [88](#), [110](#), [180](#)

AXP Atomic and X-ray Physics group at the University of Fribourg. [9](#), [11](#), [61](#), [179](#)

CAD Computer-Aided Design. [56](#)

CCD Charge-Coupled Device. [10](#), [12](#), [31](#), [61–63](#), [67–69](#), [71–75](#), [77](#), [115](#), [117](#), [118](#)

CMI Center of MicroNanoTechnology at [EPFL](#). [53](#), [54](#)

Darwin width – an angular range over which near unit reflectivity of the plane wave incident to the diffracting crystal is achieved. A Darwin width can be expressed as

$$\omega_D = \frac{r_e \lambda^2}{2\pi V_c} |F_n| \frac{K}{\sin 2\theta_B},$$

where r_e is the classical electron radius, λ is the x-ray wavelength, V_c is the unit cell volume of the lattice, F_n is the complex structure factor for the reflection order n and K is the polarization factor (1 for the perpendicular polarization and $\cos 2\theta_B$ for the parallel polarization). [75](#)

EPFL École Polytechnique Fédérale de Lausanne. [53](#), [54](#), [127](#), [128](#)

ESRF European Synchrotron Radiation Facility. [9](#), [11](#), [27](#), [35](#), [36](#), [104](#), [118](#)

EXAFS Extended X-ray Absorption Fine Structure. [126](#), [128](#)

FCM Four-Crystal Monochromator. [43–45](#)

FWHM Full Width at Half Maximum. [36](#), [39](#)

GEXRF Grazing Exit X-Ray Fluorescence / Grazing Emission X-Ray Fluorescence. [9–12](#), [18–20](#), [23](#), [27](#), [32](#), [34](#), [35](#), [37](#), [38](#), [40](#), [41](#), [49](#), [72](#), [73](#), [76](#), [79](#), [81](#), [85](#), [88](#), [95](#), [96](#), [100–106](#), [108–113](#), [115–119](#), [123–126](#)

GLOSSARY

GIXRF Grazing Incidence X-Ray Fluorescence. [9–12](#), [17–21](#), [23](#), [35](#), [43](#), [45](#), [46](#), [49](#), [79](#), [81](#), [85](#), [89](#), [93–101](#), [107](#), [108](#), [123](#), [124](#), [179](#), [180](#)

GO Geometrical Optics. [10](#), [12](#), [79](#), [94](#), [95](#), [98–103](#), [107](#), [108](#), [110](#), [123](#), [124](#), [179](#)

HERFD XAS High Energy Resolution Fluorescence Detected [XAS](#). [40](#)

HV High Vacuum – vacuum regime characterised by pressures between 10^{-5} mbar and 10^{-7} mbar. [34](#), [37](#)

HWHM Half Width at Half Maximum. [66](#)

ID Insertion Device. [36](#)

LMIS2 Laboratory of Microsystems 2 at [EPFL](#). [53](#)

MBE Molecular Beam Epitaxy. [49](#)

NEXAFS Near Edge X-ray Absorption Fine Structure. [125](#), [126](#)

Peltier element – an electronic device using a Peltier effect for cooling. It consists of two plates containing metal stripes. The stripes from each plate are connected by alternate stripes of n-type and p-type semiconductors. Passage of a current induces a Peltier effect and causes heat to be absorbed by one plate and emitted from the other. [31](#)

PGM Plane Grating Monochromator. [43](#), [47](#)

PSI Paul Scherrer Institute. [9](#)

PTB Physikalisch-Technische Bundesanstalt. [9](#), [11](#), [43](#), [45–47](#), [179](#)

QEXAFS quick [EXAFS](#). [39](#), [40](#)

RIXS Resonant Inelastic X-ray Scattering. [40](#)

rms root mean square. [21](#), [50](#), [54](#), [82](#), [95](#), [102](#), [103](#), [109](#), [111](#), [116](#)

ROI Region Of Interest. [71](#)

SDD Silicon Drift Detector. [46](#), [47](#)

SEM Scanning Electron Microscope. [51](#), [52](#), [88](#), [94](#), [107](#), [108](#)

SLS Swiss Light Source. [9](#), [11](#), [27](#), [38](#), [41](#), [104](#), [118](#)

SXM Scanning X-ray Microscope. [37](#)

TXRF Total-reflection X-Ray Fluorescence. [16–18](#), [22](#), [46](#)

UHV Ultra-High Vacuum – vacuum regime characterised by pressures lower than $\sim 10^{-7}$ mbar. [34](#), [37](#), [45](#), [46](#)

XAFS X-ray Absorption Fine Structure. [125](#)

XANES X-ray Absorption Near Edge Structure. [125](#), [126](#)

XAS X-Ray Absorption Spectroscopy. [125](#), [126](#), [128](#)

XRF X-Ray Fluorescence. [9–12](#), [16](#), [24](#), [46](#), [47](#), [123](#), [124](#)

XSW X-ray Standing Wave. [10](#), [12](#), [17](#), [20](#), [79](#), [80](#), [94](#), [95](#), [97–99](#), [107](#), [108](#), [124](#)

List of Figures

I.1	Calculated penetration depth and reflectivity for Mo $K\alpha$ x-ray radiation impinging on silicon.	17
I.2	Comparison of the GIXRF and GEXRF geometries.	18
I.3	Three types of GEXRF angular profiles for bulk-like, layer-like and particle-like structures.	19
I.4	Illustration of the stack of layers of various density model.	22
I.5	Multiple reflections in a periodic structure.	24
II.A.1	Schematic drawing of the von Hamos geometry.	27
II.A.2	Schematic view of the von Hamos spectrometer of Fribourg.	28
II.A.3	Target-slit system of the von Hamos spectrometer.	30
II.A.4	Spectrometer chamber with indication of the motion axes.	30
II.A.5	Schematic view of the carrousel target holder.	32
II.A.6	Schematic view of the piezo target holder.	33
II.A.7	Mosaic photograph of an Al plate employed to fix the samples on the rotor of the piezo motor.	35
II.A.8	Schematic representation of the ID21 beamline elements.	36
II.A.9	Top view on the SuperXAS beamline.	39
II.A.10	Schematic drawing of the von Hamos spectrometer as installed at the SLS SuperXAS beamline.	41
II.B.1	Schematic view of the plane-grating monochromator beamline.	44
II.B.2	Schematic view of the four-crystal monochromator beamline.	45
II.B.3	Schematic view of the four-crystal monochromator.	45
II.B.4	Sketch of the PTB's GIXRF experimental setup.	46
II.B.5	Sample layout in the 6-axis manipulator chamber.	47
II.B.6	Beam spot profile in the focal plane of the PGM beamline.	47
II.B.7	Illustration of the solid angle acceptance of the detector.	48
II.C.1	SEM image of NaCl structures.	51
II.C.2	SEM image of a Cr pads sample with an enlarged view of a single pad.	52
II.C.3	Schematic drawing of a Cr sample with periodic trapezoidal structures.	53
II.C.4	AFM images of Cr disc patterns prepared with the stencil method.	54
II.C.5	Different plane symmetries of the Ni/Co patterns.	56
III.A.1	Selected area of raw and corrected CCD image.	62
III.A.2	An example CCD region with a multiple hit domain consisting of two hit regions.	64

LIST OF FIGURES

III.A.3	Histogram of the charge distribution in hit regions for a measurement with densely distributed events.	66
III.A.4	Comparison between the two analysis algorithms for the case of a low CCD charge deposition rate.	68
III.A.5	Comparison between the two analysis algorithms for the case of a high CCD charge deposition rate.	68
III.C.1	Graphical representation of a ray path in a rectangular island structure.	81
III.C.2	Various wave vectors as described in text.	83
III.D.1	Illustration of the effective flux for an on-surface structure of evenly distributed squares and an incidence angle φ of the incoming radiation.	87
III.D.2	Boundary case of incident angles for which $\Phi_{eff} = \Phi$	88
IV.A.1	GIXRF profiles of Cr pads.	93
IV.A.2	Simulations of the GIXRF profiles of the 50 nm Cr pads.	94
IV.A.3	GEXRF and GIXRF angular profiles of the Cr stripes sample.	96
IV.A.4	GIXRF data for tilt angles ϑ from 0° to 8°	97
IV.A.5	Comparison between the experimental GIXRF fluorescence intensity measured at an incident beam energy of 7 keV and the calculated excitation intensities according to the XSW and GO approaches.	99
IV.A.6	GEXRF profiles of the sample with Cr stripes.	101
IV.A.7	GEXRF profiles of the sample with Cr trapezoidal prisms.	103
IV.A.8	GEXRF profiles of different p4m Cr disc patterns.	105
IV.A.9	Co $K\alpha$ and Ni $K\alpha$ GEXRF profiles of the Co/Ni discs and Co/Ni calibration bilayer.	106
IV.B.1	GIXRF profile of the NPRA0053 sample with NaCl nanostructures.	107
IV.B.2	GEXRF profiles of 5 nm Fe and Cr layers of different roughnesses.	109
IV.B.3	Different roughness models applied to GEXRF profiles of the 5 nm Fe layer with a 5.91 nm rms roughness.	111
IV.B.4	Co $K\alpha$ and Ni $K\alpha$ GEXRF profiles of the Co and Ni monolayers and Co/Ni bilayer calibration samples fabricated together with the Co and Ni discs samples.	112
IV.C.1	Si $K\alpha$ GEXRF profiles from Si supports of thermally evaporated 5 nm Fe structures of different rms roughnesses.	116
IV.C.2	An example of a Cr $K\alpha$ GEXRF profile with exit angles calibrated with the spectral background.	117
IV.C.3	Scattered background discrimination with a proper background events definition.	117
IV.C.4	Beam intensity measured at the ESRF ID21 beamline superposed with the ring current.	118

List of Tables

II.A.1	Step motors' characteristics.	30
II.A.2	Crystals' characteristics.	31
II.C.1	Samples fabricated by the Group of Magnetic Heterostructures at the Institute of Physics of the Polish Academy of Sciences.	50
II.C.2	Samples fabricated in the Surface Physics and Tunneling Spectroscopy Laboratory at the Institute of Molecular Physics of the Polish Academy of Sciences.	50
II.C.3	NaCl structures.	52
II.C.4	Process flow steps for the structuration of the plane symmetry samples. .	55
III.B.1	Darwin widths in first order of diffraction for the crystals employed in the present study.	75
IV.A.1	Comparison of n_{Co} and n_{Ni} refractive indexes for energies corresponding to Co $K\alpha$ (6.93 keV) and Ni $K\alpha$ (7.48 keV) fluorescence lines.	104

Bibliography

- [1] A. H. Compton. The total reflection of x-rays. *Philos. Mag.*, 45:1121, 1923. [15](#)
- [2] J. H. Hubbell. Review and history of photon cross section calculations. *Phys. Med. Biol.*, 51(13):R245–62, 2006. [15](#)
- [3] B. Henke, E. Gullikson, and J. Davis. X-ray interactions: Photoabsorption, scattering, transmission, and reflection at $e = 50\text{--}30,000$ eV, $z = 1\text{--}92$. *At. Data Nucl. Data Tables*, 54(2):181 – 342, 1993. [15](#), [100](#)
- [4] R. Klockenkämper. *Total-Reflection X-Ray Fluorescence Analysis (Chemical Analysis: A Series of Monographs on Analytical Chemistry and Its Applications)*. Wiley-Interscience, 1996. [16](#), [17](#), [19](#), [97](#)
- [5] R. Jenkins. *X-ray fluorescence spectrometry*. Wiley, New York, 2nd ed. edition, 1999. [16](#)
- [6] K. Stoev and K. Sakurai. Review on grazing incidence X-ray spectrometry and reflectometry. *Spectrochim. Acta, Part B*, 54(1):41–82, 1999. [16](#), [17](#), [19](#)
- [7] A. von Bohlen. Total reflection X-ray fluorescence and grazing incidence X-ray spectrometry – Tools for micro- and surface analysis. A review. *Spectrochim. Acta, Part B*, 64(9):821–832, 2009. [16](#), [19](#)
- [8] D. K. G. de Boer, A. J. G. Leenaers, and W. W. van den Hoogenhof. Glancing-incidence x-ray analysis of thin-layered materials: A review. *X-Ray Spectrom.*, 24(3):91–102, 1995. [17](#)
- [9] P. Hönicke, Y. Kayser, B. Beckhoff, M. Müller, J.-Cl. Dousse, J. Hoszowska, and S. H. Nowak. Characterization of ultra shallow aluminum implants in silicon by grazing incidence and grazing emission x-ray fluorescence spectroscopy. *J. Anal. At. Spectrom.*, 27:1432–1438, 2012. [17](#), [19](#)
- [10] R. S. Becker, J. A. Golovchenko, and J. R. Patel. X-ray evanescent-wave absorption and emission. *Phys. Rev. Lett.*, 50(3):153–156, 1983. [18](#)
- [11] D. K. G. de Boer. Glancing-incidence x-ray fluorescence of layered materials. *Phys. Rev. B*, 44(2):498–511, 1991. [19](#)
- [12] H. P. Urbach and P. K. de Bokx. Calculation of intensities in grazing-emission x-ray fluorescence. *Phys. Rev. B*, 53(7):3752–3763, 1996. [18](#), [19](#)

BIBLIOGRAPHY

- [13] P. K. de Bokx, Chr. Kok, A. Bailleul, G. Wiener, and H. P. Urbach. Grazing-emission x-ray fluorescence spectrometry; principles and applications. *Spectrochim. Acta, Part B*, 52(7):829–840, 1997. [18](#), [19](#)
- [14] R. Carminati, M. Nieto-Vesperinas, and J.-J. Greffet. Reciprocity of evanescent electromagnetic waves. *J. Opt. Soc. Am. A*, 15(3):706–712, 1998. [18](#)
- [15] T. Noma, A. Iida, and K. Sakurai. Fluorescent-x-ray-interference effect in layered materials. *Phys. Rev. B*, 48(23):17524, 1993. [18](#), [20](#)
- [16] A. Bekshaev and R. Van Grieken. Substrates with a periodic surface structure in grazing-exit X-ray microanalysis. *Spectrochim. Acta, Part B*, 57(5):865–882, 2002. [18](#), [19](#), [23](#)
- [17] A. Bekshaev and R. Van Grieken. Interference technique in grazing-emission electron probe microanalysis of submicrometer particles. *Spectrochim. Acta, Part B*, 56(5):503–515, 2001. [18](#), [19](#), [20](#)
- [18] P. De Bokx and H. Urbach. Laboratory grazing-emission x-ray fluorescence spectrometer. *Rev. Sci. Instrum.*, 66(1):15–19, 1995. [18](#)
- [19] A. Kubala-Kukuś, D. Banaś, W. Cao, J.-Cl. Dousse, J. Hoszowska, Y. Kayser, M. Pajek, M. Salomé, J. Susini, J. Szlachetko, and M. Szlachetko. Observation of ultralow-level Al impurities on a silicon surface by high-resolution grazing emission x-ray fluorescence excited by synchrotron radiation. *Phys. Rev. B*, 80(11):113305–4, 2009. [19](#), [22](#)
- [20] J. Szlachetko, D. Banaś, A. Kubala-Kukuś, M. Pajek, W. Cao, J.-Cl. Dousse, J. Hoszowska, Y. Kayser, M. Szlachetko, M. Kavčič, M. Salomé, and J. Susini. Application of the high-resolution grazing-emission x-ray fluorescence method for impurities control in semiconductor nanotechnology. *J. Appl. Phys.*, 105:086101, 2009. [18](#), [19](#), [34](#)
- [21] M. Claes, R. Van Grieken, and P. de Bokx. Comparison of Grazing Emission XRF with Total Reflection XRF and Other X-Ray Emission Techniques. *X-Ray Spectrom.*, 26(4):153–158, 1997. [19](#)
- [22] M. Claes, P. de Bokx, and R. Van Grieken. Progress in laboratory grazing emission x-ray fluorescence spectrometry. *X-Ray Spectrom.*, 28(4):224–229, 1999. [19](#)
- [23] U. Weisbrod, R. Gutschke, J. Knoth, and H. Schwenke. Total reflection X-ray fluorescence spectrometry for quantitative surface and layer analysis. *Appl. Phys. A*, 53(5):449–456, 1991. [19](#)
- [24] Y. Kayser, D. Banaś, W. Cao, J.-Cl. Dousse, J. Hoszowska, P. Jagodziński, M. Kavčič, A. Kubala-Kukuś, S. Nowak, M. Pajek, and J. Szlachetko. Depth profiles of Al impurities implanted in Si wafers determined by means of the high-resolution grazing emission X-ray fluorescence technique. *Spectrochim. Acta, Part B*, 65(6):445–449, 2010. [19](#)
- [25] J. Osán, F. Reinhardt, B. Beckhoff, A. E. Pap, and S. Török. Probing patterned wafer structures by means of grazing incidence x-ray fluorescence analysis. *ECS Trans.*, 25(3):441–451, 2009. [19](#), [20](#), [93](#)

- [26] M. K. Tiwari, G. M. Bhalerao, M. Babu, A. K. Sinha, and C. Mukherjee. Investigation of metal nanoparticles on a Si surface using an x-ray standing wave field. *J. Appl. Phys.*, 103(5):054311, 2008.
- [27] A. von Bohlen, M. Krämer, C. Sternemann, and M. Paulus. The influence of X-ray coherence length on TXRF and XSW and the characterization of nanoparticles observed under grazing incidence of X-rays. *J. Anal. At. Spectrom.*, 24(6):792, 2009. [20](#), [79](#)
- [28] H. Schwenke, P. A. Beaven, and J. Knoth. Total reflection and grazing emission x-ray fluorescence spectrometry: Assessment of the size of contaminant particles on silicon wafer surfaces. In K. L. Mittal, editor, *Particles on Surfaces 7: Detection, Adhesion and Removal.*, pages 11–26, 2002. [22](#)
- [29] H. Schwenke, J. Knoth, and U. Weisbrod. Analysis of particles on surfaces by total reflection xray. In *Particles on surfaces 3: detection, adhesion, and removal*, pages 131–141. Springer, 1991. [19](#)
- [30] C. Horntrich, F. Meirer, C. Streli, P. Kregsamer, G. Pepponi, N. Zoeger, and P. Wobrauschek. Influence of the sample morphology on total reflection x-ray fluorescence analysis. *Powder Diffr.*, 24(2):140–144, 2009. [20](#)
- [31] P. Croce and L. Nénot. Étude des couches minces et des surfaces par réflexion rasante, spéculaire ou diffuse, de rayons x. *Rev. Phys. Appl.*, 11(1):113–125, 1976. [21](#)
- [32] L. Nevot and P. Croce. Caractérisation des surfaces par réflexion rasante de rayons x. application à l’étude du polissage de quelques verres silicates. *Rev. Phys. Appl.*, 15(3):761–779, 1980.
- [33] L. Nevot, B. Pardo, and J. Corno. Characterization of X-UV multilayers by grazing incidence X-ray reflectometry. *Rev. Phys. Appl.*, 23(10):1675–1686, 1988. [21](#), [80](#), [81](#), [109](#)
- [34] S. K. Sinha, E. B. Sirota, S. Garoff, and H. B. Stanley. X-ray and neutron scattering from rough surfaces. *Phys. Rev. B*, 38(4):2297, 1988. [21](#)
- [35] D. K. G. de Boer. X-ray scattering and x-ray fluorescence from materials with rough interfaces. *Phys. Rev. B*, 53(10):6048–6064, 1996. [21](#), [81](#)
- [36] D. K. G. de Boer. X-ray reflection and transmission by rough surfaces. *Phys. Rev. B*, 51(8):5297–5305, 1995.
- [37] D. K. G. de Boer. Influence of the roughness profile on the specular reflectivity of x rays and neutrons. *Phys. Rev. B*, 49(9):5817–5820, 1994. [21](#), [22](#), [80](#), [81](#)
- [38] R. Lazzari, F. Leroy, and G. Renaud. Grazing-incidence small-angle x-ray scattering from dense packing of islands on surfaces: Development of distorted wave born approximation and correlation between particle sizes and spacing. *Phys. Rev. B*, 76(12):125411, 2007. [21](#)
- [39] R. Lazzari, G. Renaud, J. Jupille, and F. Leroy. Self-similarity during growth of the Au/TiO₂(110) model catalyst as seen by the scattering of x-rays at grazing-angle incidence. *Phys. Rev. B*, 76(12):125412, 2007. [21](#)

BIBLIOGRAPHY

- [40] M. K. Tiwari, G. S. Lodha, and K. J. S. Sawhney. Applications of the ‘CATGIXRF’ computer program to the grazing incidence X-ray fluorescence and X-ray reflectivity characterization of thin films and surfaces. *X-Ray Spectrom.*, 39(2):127–134, 2010. [21](#), [124](#)
- [41] H. Schwenke, R. Gutschke, J. Knoth, and M. Kock. Treatment of roughness and concentration gradients in total reflection X-ray fluorescence analysis of surfaces. *Appl. Phys. A*, 54(5):460–465, 1992. [21](#), [22](#), [80](#), [81](#)
- [42] K. Tsuji, S. Sato, and K. Hirokawa. Glancing-incidence and glancing-takeoff X-ray fluorescence analysis of a Mn ultrathin film on an Au layer. *Thin Solid Films*, 274(1-2):18–22, 1996. [22](#), [81](#)
- [43] H. Schwenke and J. Knoth. Depth Profiling in Surfaces Using Total Reflection X-Ray Fluorescence. *Anal. Sci.*, 11(3):533–537, 1995. [22](#)
- [44] K. Tsuji, T. Yamada, T. Utaka, and K. Hirokawa. The effects of surface roughness on the angle-dependent total-reflection x-ray fluorescence of ultrathin films. *J. Appl. Phys.*, 78(2):969–973, 1995. [22](#), [23](#), [80](#), [81](#)
- [45] J. Hozowska, J.-Cl. Dousse, J. Kern, and C. Rhême. High-resolution von Hamos crystal X-ray spectrometer. *Nucl. Instrum. Methods Phys. Res., Sect. A*, 376(1):129–138, 1996. [27](#), [30](#), [71](#), [73](#), [75](#)
- [46] J. Szlachetko, J.-Cl. Dousse, J. Hozowska, M. Berset, W. Cao, M. Szlachetko, and M. Kavčič. Relative detection efficiency of back-and front-illuminated charge-coupled device cameras for x-rays between 1 keV and 18 keV. *Rev. Sci. Instrum.*, 78:093102, 2007. [31](#), [61](#), [62](#)
- [47] R. Frahm, M. Nachtegaal, J. Stötzl, M. Harfouche, J. A. van Bokhoven, and J.-D. Grunwaldt. The dedicated qexafs facility at the sls: Performance and scientific opportunities. *AIP Conf. Proc.*, 1234(1):251–255, 2010. [39](#)
- [48] F. Senf, U. Flechsig, F. Eggenstein, W. Gudat, R. Klein, H. Rabus, and G. Ulm. A plane-grating monochromator beamline for the PTB undulators at BESSY II. *J. Synchrotron Radiat.*, 5(3):780–782, 1998. [43](#), [44](#)
- [49] M. Krumrey. Design of a four-crystal monochromator beamline for radiometry at bessy ii. *J. Synchrotron Radiat.*, 5(1):6–9, 1998. [43](#), [45](#)
- [50] M. Krumrey, C. Herrmann, P. Müller, and G. Ulm. Components for the X-ray radiometry beamline at BESSY II. *J. Synchrotron Radiat.*, 5(3):788–790, 1998. [43](#)
- [51] J. W. M. DuMond. Theory of the use of more than two successive x-ray crystal reflections to obtain increased resolving power. *Phys. Rev.*, 52:872–883, 1937. [44](#)
- [52] B. Beckhoff, R. Fliegauf, M. Kolbe, M. Müller, J. Weser, and G. Ulm. Reference-free total reflection x-ray fluorescence analysis of semiconductor surfaces with synchrotron radiation. *Anal. Chem.*, 79(20):7873–7882, 2007. [45](#), [47](#), [48](#)
- [53] B. Beckhoff. Reference-free x-ray spectrometry based on metrology using synchrotron radiation. *J. Anal. At. Spectrom.*, 23:845–853, 2008. [45](#), [46](#), [48](#)

- [54] F. Reinhardt, J. Osán, S. Török, A. E. Pap, M. Kolbe, and B. Beckhoff. Reference-free quantification of particle-like surface contaminations by grazing incidence x-ray fluorescence analysis. *J. Anal. At. Spectrom.*, 27:248–255, 2012. [46](#), [48](#), [52](#), [93](#), [94](#)
- [55] J. Lubeck, B. Beckhoff, R. Fliegauf, I. Holfelder, P. Hönicke, M. Müller, and J. Weser. Development of a new instrumentation for reference-free nanoanalytics by means of x-ray spectrometry. Unpublished. [46](#)
- [56] A. Wawro, S. Suto, R. Czajka, and A. Kasuya. The solid state reaction of fe with the si(111) vicinal surface: splitting of bunched steps. *Nanotechnology*, 19(20):205706, 2008. [50](#), [51](#)
- [57] A. Wawro, S. Suto, R. Czajka, and A. Kasuya. Thermal reaction of iron with a si(111) vicinal surface: Surface ordering and growth of cscl-type iron silicide. *Phys. Rev. B*, 67:195401, 2003. [50](#), [51](#)
- [58] G. Villanueva, O. Vazquez-Mena, M. van den Boogaart, K. Sidler, K. Pataky, V. Savu, and J. Brugger. Etching of sub-micrometer structures through stencil. *Microelectron. Eng.*, 85(5):1010–1014, 2008. [54](#)
- [59] H. Wondratschek. Classifications of space groups, point groups and lattices. In T. Hahn, editor, *International Tables for Crystallography*, volume A: Space-group symmetry, chapter 8.2, pages 726–731. International Union of Crystallography, Chester, England, 5 edition, 2006. [54](#), [56](#)
- [60] C. R. Vane, M. S. Smith, and S. Raman. A versatile, highly-efficient, high-resolution von hamos bragg crystal x-ray spectrometer. Technical report, Oak Ridge National Lab., TN (USA), 1988. [73](#), [74](#)
- [61] M. S. del Río and R. J. Dejus. Xop 2.1 — a new version of the x-ray optics software toolkit. *AIP Conf. Proc.*, 705(1):784–787, 2004. [75](#)
- [62] W. Wu and W. Wallace. Microroughness of polymer thin films studied by total-reflection x-ray fluorescence and atomic force microscopy. *J. Vac. Sci. Technol. B*, 16:1958, 1998. [81](#)
- [63] I. A. Vartanyants and A. Singer. Coherence properties of hard x-ray synchrotron sources and x-ray free-electron lasers. *New J. Phys.*, 12(3):035004, 2010. [85](#)
- [64] D. Windt. IMD—software for modeling the optical properties of multilayer films. *Comput. Phys.*, 12:360, 1998. [97](#), [124](#)

Appendices

MATLAB functions

Appendix A

vonHamosSpot function

This function calculates the form of the CCD image of an arbitrary flat source in von Hamos geometry.

The program requires `parse_pv_pairs` function available at

<http://www.mathworks.com/matlabcentral/fileexchange/9082-parsepvpairs>

Contents

A.1	Syntax	145
A.2	Syntax description	146
A.3	Optional parameters	146
A.3.1	Positioning motors parameters.	146
A.3.2	Reflecting crystal parameters	147
A.3.3	Beam spot parameters	147
A.3.4	CCD parameters	148
A.3.5	Algorithm parameters	148
A.4	Output arguments	148
A.4.1	out Structure	148
A.4.2	params structure	148
A.5	Notes on the computation methods used	149

A.1 Syntax

```
P = vonHamosSpot(Bragg)
P = vonHamosSpot(Bragg,'ParameterName',ParameterValue)
P = vonHamosSpot(Bragg,params)
P = vonHamosSpot(params)
P = vonHamosSpot(params,'ParameterName',ParameterValue)
[P,out] = vonHamosSpot(...)
[P,out,params] = vonHamosSpot(...)
```

A.2 Syntax description

`P = vonHamosSpot(Bragg)` returns `nx3` array with `x` (first column), `y` (second column) and `z` (third column) coordinates of an image (in mm) for a given Bragg angle in radians and default spectrometer parameters. As an origin of coordinates the slit position is taken.

`P = vonHamosSpot(Bragg, 'ParameterName', ParameterValue)` provides an opportunity to manipulate the spectrometer and algorithm parameters. Parameters are entered as one or more name and value pairs.

`P = vonHamosSpot(Bragg, params)` the same as above but parameters are provided in `params` structure with fields named correspondingly.

`P = vonHamosSpot(params)` similar as above, however the `params` structure must have an additional `Bragg` field containing Bragg angles in radians.

`P = vonHamosSpot(params, 'ParameterName', ParameterValue)` provides an opportunity to manipulate the spectrometer and algorithm parameters entered in `params` structure. Useful when adjusting parameters correction. Again `params` structure must have an additional `Bragg` field.

`P = vonHamosSpot(params, params2)` the same as above but additional parameters are provided in `params2` structure with fields named correspondingly.

`[P, out] = vonHamosSpot(...)` gives additional output parameters stored in `out` structure.

`[P, out, params] = vonHamosSpot(...)` returns `params` structure with the spectrometer and algorithm parameters used. (The `correction` parameter returned in `params` structure may be different, please see below for explanation.)

A.3 Optional parameters

Optional parameters defining the spectrometer and algorithm setup can be entered as one or more name and value pairs. Below possible parameters are listed together with their default values.

A.3.1 Positioning motors parameters

- Motor positions can be given in motor steps (`TAF`, `TAT`, `TAL`, `DET`, `CRY`, `CRF`) or in mm/rad (`sourceX`, `sourceY`, `sourceTilt`, `detector`, `crystal`, `R`).
- As the origin of the coordinate system O the central position of the slit is taken.

parameter	value	description

<code>sourceX</code>	0	<code> x </code> source position
<code>TAT</code>	0	by default source is located at slit
<code>dTAT</code>	0	correction to position given in motor steps

<code>sourceY</code>	0	<code> y </code> source position
<code>TAF</code>	0	by default source is source located at slit
<code>dTAF</code>	0	correction to position given in motor steps

<code>sourceTilt</code>	0	source tilt in respect to <code> x </code> axis
<code>TAL</code>	50000	by default source is not tilted
<code>dTAL</code>	0	correction to position given in motor steps
<code>phi</code>	~	optional parameter defining the maximum exit angle from sample given in radians. If the parameter is defined <code> TAL </code> and <code> sourceTilt </code> parameters are ignored.

<code>detector</code>	0	detector <code> x </code> position
<code>DET</code>	0	by default detector is positioned at slit
<code>dDET</code>	0	correction to position given in motor steps

<code>Y_CCD</code>	0	detector <code> y </code> position

<code>Z_CCD</code>	0	detector <code> z </code> position

<code>crystal</code>	~	crystal <code> x </code> position
<code>CRY</code>	~	if parameters are not given, the <code> crystal </code> position is taken as <code> detector /2</code> or, in case <code> detector = 0</code> , is calculated from the first element of <code> Bragg </code> parameter.
<code>dCRY</code>	0	correction to position given in motor steps

R	254	crystal y position
CRF	101600	by default equals to default curvature radius of 254 mm
dCRF	0	correction to position given in motor steps

Z_crystal	0	crystal z position

A single motor step corresponds to following distances:

- for CRF, TAF, TAT - 0.0025 mm,
- for CRY, DET - 0.005 mm,
- for TAL - $0.00225^\circ = 3.9270\text{e-}5$ rad.

If both positions in motor steps and in mm/rad are given, then motor positions used by the program depend on the `correction` parameter (see below):

- `correction==false` position in motor steps is overwritten; *e.g.* for crystal y position:

$$\text{CRF} = R/0.0025 + \text{dCRF}$$

- `correction==true` if no correction to position in motor steps is given as name and value pair then such a correction is calculated as a difference between position given in mm/rad and position given in motor steps; otherwise, if correction to position in motor steps is given as name and value pair, the position in mm/rad is overwritten; *e.g.* for crystal y position:

$$\begin{aligned} \text{dCRF} &= R/0.0025 - \text{CRF} && \text{if dCRF is not given as name and value pair} \\ R &= (\text{CRF} + \text{dCRF}) * 0.0025 && \text{if dCRF is given as name and value pair} \end{aligned}$$

A.3.2 Reflecting crystal parameters

parameter	value	description

rho	254	crystal radius of curvature in mm
Cristal_width	100	crystal width along the curvature in mm
rotX	0	crystal rotation around parallel to x -axis
rotY	0	crystal rotation around parallel to y -axis
rotZ	0	crystal rotation around parallel to z -axis
Psi_limits	~	optional parameter defining the arc section of the crystal. If not given, the arc section limits can be calculated from Cristal_width . Psi_limits should be given in radians.

A.3.3 Beam spot parameters

- Beam spot parameters define the geometry of the fluorescence source relatively to source location defined by motor positions.

parameter	value	description

X	0	array of beam spot x -coordinates in mm
Z	0	array of beam spot z -coordinates in mm
dX	0	x displacement of a beam spot from the source location defined by motor positions.
dZ	0	z displacement of a beam spot from the source location defined by motor positions.
parallel_beam	true	determines either a beam irradiates a whole sample (<code> false </code>) or a part of it (<code> true </code>).

A.3.4 CCD parameters

parameter	value	description
pixelsX	1340	number of pixels in x direction
pixelsZ	400	number of pixels in z direction
pixelXdim	0.02	pixel width in mm
pixelZdim	0.02	pixel height in mm
CCDrotX	0	CCD rotation around parallel to x -axis
CCDrotY	0	CCD rotation around parallel to y -axis
CCDrotZ	0	CCD rotation around parallel to z -axis

A.3.5 Algorithm parameters

parameter	value	description
Psi_points	50	number of crystal arc section partition
rand	true	parameter defining equal false or random true partition of crystal arc section
MAP	false	parameter providing additional matrices in the output
Bragg_span	20	used only if MAP = true ; determines density of Bragg angle sampling for parametric arrays creation.
Psi_span	20	used only if MAP = true ; determines density of crystal arc section partition for parametric arrays creation.
correction	false	parameter specifying the way the motor positions are calculated if given both in mm/rad and motor steps (see above)
Bragg	~	optional parameter needed if Bragg angle is not given as a first input argument of vonHamosSpot function. Parameter specifies Bragg angles in radians and overwrites the latest if already entered.

A.4 Output arguments

A.4.1 out Structure

As a second output argument the `vonHamosSpot` functions can return out structure with the following fields:

- `X_P`, `Z_P` – image positions on the CCD in pixels;
- `X_R`, `Y_R`, `Z_R` – coordinates of points of incidence on the crystal relative to the crystal center;
- `X_S`, `Y_S`, `Z_S` – source points coordinates;
- `phi` – exit angles corresponding to each point of calculated image;
- `theta` – radiation direction corresponding to each each point of calculated image;
- `Bragg_MAP`, `phi_MAP`, `theta_MAP` – only if MAP parameter set to `true` – additional parametric arrays of the CCD image dimensions corresponding to Bragg, exit, and radiation direction angles.

A.4.2 params structure

As a third output argument a `params` structure can be returned. The fields of a `params` structure correspond to all the parameters (custom and default) that have been used by the program.

The only exception to above rule is a `correction` parameter which value is returned depending on the way the `vonHamosSpot` function was invoked.

SYNTAX	params.correction
-----	-----
<code>vonHamosSpot(Bragg)</code>	<code>true</code>
<code>vonHamosSpot(Bragg, 'ParameterName', ParameterValue)</code>	<code>true</code>
<code>vonHamosSpot(Bragg, params)</code>	<code>true</code>
<code>vonHamosSpot(params)</code>	<code>true</code>
<code>vonHamosSpot(params, 'ParameterName', ParameterValue)</code>	<code>false</code>
<code>vonHamosSpot(params, params2)</code>	<code>false</code>

Such a behaviour of the `vonHamosSpot` function allows a following set of operation without a need of `correction` parameter specification:

- Initial definition of von Hamos spectrometer parameters, *e.g.*:

```
[P,out,params]= vonHamosSpot(Bragg, 'ParameterName', ParameterValue)
```

- Correction of initial parameters using the above `params` structure, *e.g.*:

```
[P,out,corr_params]= vonHamosSpot(params, 'ParameterName', ...
                                ParameterValue)
```

- The use of the corrected parameters `corr_params` for other problems with the same von Hamos spectrometer setup, *e.g.*

```
[P,out] = vonHamosSpot(corr_params, 'ParameterName', ParameterValue)
```

Of course if `correction` parameter is specified as a name and value pair or in `params2` structure the value from `params` structure is overwritten.

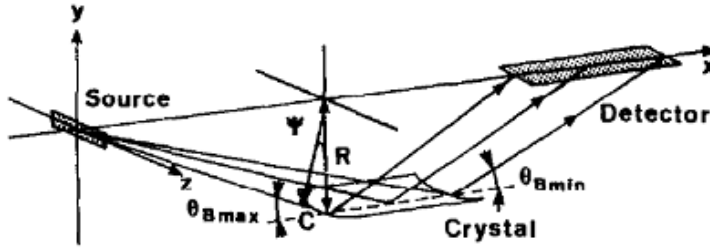
A.5 Notes on the computation methods used

The image calculations are being performed using geometrical optics.

For input motor positions as the origin of the coordinate system O the central position of the slit is taken an x , y and z directions are defined by the movement directions of the motors.

The optical path computations are performed in transformed coordinates O' for which the x axis is collinear with the curvature axis of the reflecting crystal and the origin of the x coordinate is in the middle of the Bragg crystal.

For the image computation another coordinates O'' are taken in which the CCD is centered on the $y = 0$ plane.



Appendix B

spe_read function

This function reads the WinView/WinSpec (WINX) `.spe` files.

Contents

B.1	Syntax	151
B.2	Syntax description	151
B.3	Copyright notice	151

B.1 Syntax

```
Frames = spe_read(files)
Frames = spe_read(files,folder)
Frames = spe_read(files,folder,range)
[Frames,File_paths] = spe_read(files,...)
```

B.2 Syntax description

`Frames = spe_read(files)` returns an `Nx1` cell array `Frames` containing `ydim x xdim x NumFrames` arrays of data corresponding to `N` files specified in `files` argument. The `files` argument can be given as a string with files separated by a new line character or as a cell array of strings. If only the file names are given the files should be given with the full path, or should be located in the current directory.

`Frames = spe_read(files,folder)` specifies a folder in which `.spe` files are located.

`Frames = spe_read(files,folder,range)` specifies a frames range that should be read from files.

`[Frames,File_paths] = spe_read(files,...)` returns file paths to `.spe` files.

B.3 Copyright notice

WinView/WinSpec (WINX) `.spe` files are proprietary Roper Scientific file formats. File format description is available at:

<ftp://ftp.piacton.com/Public/Software/Examples/datatypes/WINHEAD.TXT>

Appendix C

choose_files function

Finds and sorts files for given `filename` and `suffix`. Returned files have a following form:

```
filename[0-9]*suffix,
```

where `[0-9]*` is an arbitrary sequence of digits.

C.1 Syntax

`file_list = choose_files(filename,suffix)` returns sorted list of files of a form `filename[0-9]*suffix` in a cell array of string. The file name should be given with as a full path, or should be located in the current directory.

`file_list = choose_files(filename,suffix,folder)` specifies a folder in which files are located.

`[file_list] = choose_files(filename,suffix,folder,option)` specifies one of following additional option:

- `'path'` the `file_list` is returned as a list of full file paths;
- `'string'` the `file_list` is returned as a string with file names surrounded by quotation marks and separated by white spaces;
- `'clipboard'` copy to clipboard the `file_list` as a list of file names surrounded by quotation marks and separated by white spaces. This option does not change the output format.

Appendix D

GEXRF_island function

Compute GEXRF/GIXRF intensities for rectangular islands on a flat support.

Contents

D.1	Syntax	155
D.2	Syntax description	155
D.3	Input parameters	155
D.4	Optional input parameters	156
D.5	Algorithm	156

D.1 Syntax

```
I = GEXRF_island(n_island,n_support,Phi,E,h,l,d,kroky,kroxx)
I = GEXRF_island(...,'ParameterName',<ParameterValue>)
[I,I1,I2,N] = GEXRF_island(...)
```

D.2 Syntax description

`I = GEXRF_island(n_island,n_support,Phi,E,h,l,d,kroky,kroxx)` returns GEXRF intensities for each exit angle `Phi`.

`I = GEXRF_island(...,'ParameterName',<ParameterValue>)` manipulates algorithm by setting additional parameters.

`[I,I1,I2,N] = GEXRF_island(...)` additionally returns vectors of intensities emitted by the upper `I1` and lateral `I2` island planes an maximal number of islands `N` used in computation.

D.3 Input parameters

Following input parameters are required by the `GEXRF_island` function:

- `n_island` – complex refractive index of an island material,
- `n_support` – complex refractive index of a support material,
- `Phi` – vector of grazing angles in radians,
- `E` – x-ray energy in eV (of fluorescence for GEXRF, or of excitation for GIXRF),
- `h` – island height in nm,
- `l` – island widths in nm (as scalar or vector),
- `d` – distances between islands in nm (as scalar or vector),
- `kroky` – number of fluorescence points in vertical dimension,
- `kroxx` – number of fluorescence points in lateral dimension.

D.4 Optional input parameters

Following parameters can be optionally given in order to modify the algorithm operation:

ParameterName	ParameterValue	Description
'Degree' 'deg'	_no value_	Notify that exit angle vector is given in degrees.
'WaveNumber' 'k'	_no value_	Notify that a wave number instead of photon energy is given as an input argument.
'PrintInfo' 'info'	_no value_	Prints computation information to Command Window during the code evaluation.
'NumberOfIslands' 'nbisl'	inf	Changes the number of islands from inf to a given value.
'SurfaceRoughness' 'dh',	0	Sets the surface roughness.
'LengthVariation' 'dl'	0	Sets the dispersion of island width.
'DistanceVariation' 'dd'	0	Sets the dispersion of distance between islands.
'Precision' 'prec'	100	Calculates the ray path unless the intensity drops prec times.
'XPosition' 'xpos'	1/(2*krokk)... : 1/(krokk): 1	Defines explicitly fluorescence points x positions in nm.
'YPosition' 'ypos'	h/(2*kroky)... : h/(kroky): h	Defines explicitly fluorescence points y positions in nm.
'XInLine'	_no value_	Turn of random distribution of fluorescence points in x direction.
'YInLine'	_no value_	Turn of random distribution of fluorescence points in y direction.
'RadiationPower' 'rp'	'1'	Function of the position dependent fluorescence radiation power. Function should be enter as a string with a matlab code for evaluation. Following variables can be used: * Y - y position, * X - x position, * h - island height, * l - island width.

D.5 Algorithm

The optical path is traced starting at fluorescence points.

In general calculation of the interference effects requires taking into account all the possible reflections and refractions for all the possible ray paths between the detector (or source in case of GIXRF) and a given fluorescing atom. Consequently a proper calculation of a fluorescence radiation is a very complex problem with a behaviour $O(e^x)$.

Thus an assumption needs to be taken that the support material is flat and that all the considered interfaces are either parallel or perpendicular to the support. With such a geometric configuration the final ray reaching the detector (or source in case of GIXRF) can cross the island-vacuum interface only in two manner – form a top or side island interface. Furthermore the ray vector passing trough a vacuum between two islands does not change its direction in consecutive islands.

The reflections at the horizontal interfaces change only the y component of a wave vector not changing its length. The reflections at the vertical interfaces can be neglected by the algorithm as in the x-ray regime the reflectivity quickly goes to zero for small reflection angles.

Concluding, provided that we count only rays reaching the detector (or source in case of GIXRF) at a single direction, we can consider only four ray vectors at a starting point of an optical path:

1. two ray vectors (up and down) for radiation crossing the final island-vacuum interface at the top island interface,
2. two ray vectors (up and down) for radiation crossing the final island-vacuum interface at the side island interface.

MATLAB tutorials

Appendix E

Spectrometer parameters correction

In this script we will present the way to find corrections to von Hamos spectrometer parameters. We will use the `spe_read` function to read the CCD images stored in `.spe` files, and `vonHamosSpot` function for calculations of the theoretical form of a CCD image.

Contents

E.1	Loading <code>.spe</code> files	161
E.2	Calculated form of the image	162
E.3	Parameters correction	164
E.4	CCD image transformation	165

E.1 Loading `.spe` files

For the correction to be the best it is advised to simultaneously work on CCD images collected for several fluorescence lines. For this tutorial we will use data collected with SiO_2 (1-10) crystal ($2d = 8.5096 \text{ \AA}$) for Si $K\alpha$ and Cr $K\alpha$ fluorescence lines. The images were collected by means of synchrotron light source in slit-less geometry.

- fluorescence lines energy in eV:

```
1 SiKa = 1739.98;  
2 CrKa1 = 5414.72;  
3 CrKa2 = 5405.509;
```

- $3d$ – double spacing between the SiO_2 (1-10) crystal lattice planes:

```
4 x2d = 8.5096;
```

The Si $K\alpha$ line was registered in `Si05TALProfile` experiment and the Cr $K\alpha$ line in `Cr03TALProfile`.

```
5 Experiments = {'Si05TALProfile', 'Cr03TALProfile'};
```

The files reside in the following folder:

```
6 folder = ...  
7 ...     '~/MI-1108/MI-1108/' ; % Unix path  
8 ...     'Z:\MI-1108\MI-1108\' ; % Windows path
```

In order to select appropriate files (excluding `s.spe` and `p.spe` *etc.* files) we will use the `choose_files` function.

```
9 for i = 1: numel(Experiments)  
10     File_list{i} = choose_files(Experiments{i}, '.spe', folder, 'path');  
11 end
```

APPENDICES

We will load only last 12 files of each experiment. We will not store the files data however, but only the sum of overall intensity. To increase the contrast we will neglect the pixels with background intensity. We will read each file separately using a `spe_read` function. To speed up the code we will use the `parfor` loop that take advantage of parallel computing on multi CPU machines.

```

12 for i = 1: numel(Experiments)
13     file_list = File_list{i};
14     % Reading of the last file from the list
15     frames = spe_read(file_list{end});
16     % Preallocation of the /Images_sum/ variable (overall intensity
17     % neglecting the background):
18     Images_sum = sum(frames{1}.*(frames{1}>134),3);
19     % /parfor/ loop for parallel file reading:
20     parfor j = numel(file_list) - (11:-1:1)
21         frames = spe_read(file_list{j});
22         % Overall intensity neglecting the background:
23         Images_sum = Images_sum + sum(frames{1}.*(frames{1}>134),3);
24     end
25     Images{i} = Images_sum;
26 end

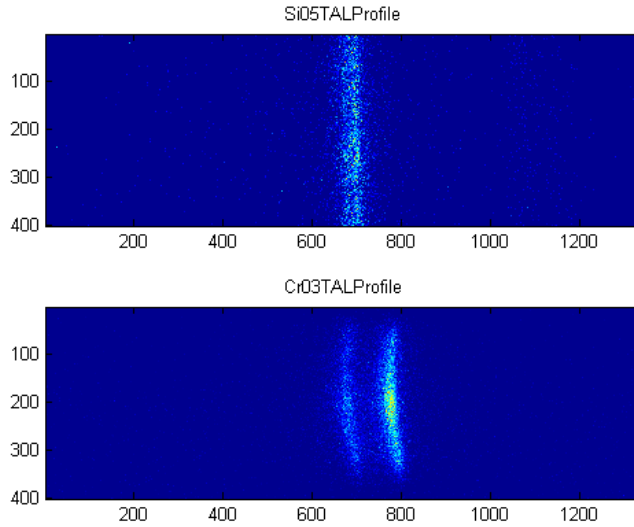
```

Now, lets plot the images:

```

27 figure_window = figure;
28 for i=1:numel(Images)
29     % We want two plots in one window:
30     subplot(ceil(numel(Images)),1,i)
31     % Plotting the images:
32     imagesc(Images{i})
33     % Lets adjust the color scale:
34     caxis([0,max(Images{i}(:))])
35     % and put the name:
36     title(Experiments(i))
37 end

```



E.2 Calculated form of the image

The Bragg angle can be calculated from the fluorescence energy using the Bragg law:

$$2d \sin \theta_B = n\lambda$$

,

where θ_B is a Bragg angle, n is an reflection order and λ is a wavelength. Knowing that $\lambda = hc/E$ we get:

$$\theta_B = \arcsin \frac{nhc}{2dE}$$

Lets calculate hc product with Plank constant in $eV \cdot s$ and speed of light in \AA :

```
38 hc = 4.135667516e-15 * 299792458e10;
```

The CCD images were acquired with the following setup:

Si05TALProfile:

- 1st order Bragg reflection at 56.86° ,
- motor positions: DET=66324, CRY=33162, TAF=15275, TAT=10012;
- synchrotron beam cross-section: 0.2x0.2 mm

```
39 SiBragg = asind(hc/x2d/SiKa)
```

```
40 [Si_beam_X,Si_beam_Z] = meshgrid([-1 0 .1],[-1 0 .1]);
```

```
SiBragg =  
56.8625
```

Cr03TALProfile50.spe:

- 2^{dn} order Bragg reflection at 32.56° ($K\alpha^1$) and 32.62° ($K\alpha^2$),
- motor positions: DET = 159129, CRY = 79565, TAF= 6341, TAT=10012.
- synchrotron beam cross-section: 1x1 mm

```
41 CrBragg = asind(2*hc/x2d./[CrKa1,CrKa2])
```

```
42 [Cr_spot_X,Cr_spot_Z] = meshgrid([-1.5 0 .5],[-1.5 0 .5]);
```

```
CrBragg =  
32.5584 32.6208
```

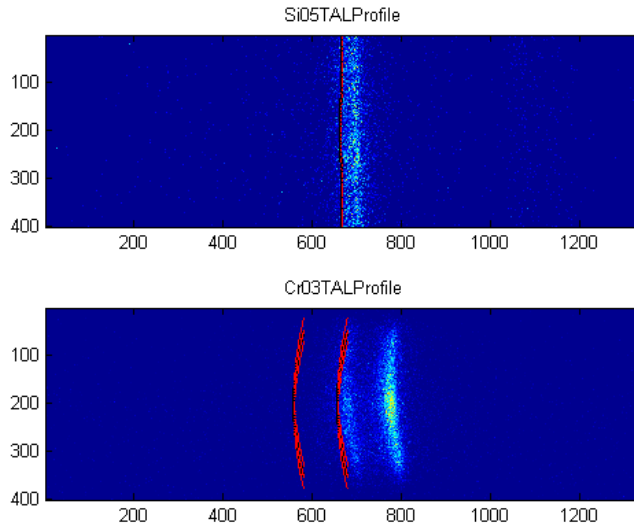
Lets calculate the form of an image for the above parameters (we will set the exit angle ϕ to 0).

```
43 % preallocation of variables:  
44 Out = cell(size(Experiments));  
45 Params = cell(size(Experiments));  
46 % Si image:  
47 [~,Out{1},Params{1}] = vonHamosSpot(asin(hc/x2d/SiKa)...  
48                                     , 'X', Si_beam_X ...  
49                                     , 'Z', Si_beam_Z ...  
50                                     , 'rand', false...  
51                                     , 'DET', 66324 ...  
52                                     , 'CRY', 33162 ...  
53                                     , 'TAF', 15275 ...  
54                                     , 'TAT', 10012 ...  
55                                     , 'phi', 0);  
56 % Cr image:  
57 [~,Out{2},Params{2}] = vonHamosSpot(asin(2*hc/x2d./[CrKa1,CrKa2])...  
58                                     , 'X', Cr_spot_X ...  
59                                     , 'Z', Cr_spot_Z ...  
60                                     , 'rand', false...  
61                                     , 'DET', 159129 ...  
62                                     , 'CRY', 79565 ...  
63                                     , 'TAF', 6341 ...  
64                                     , 'TAT', 10012 ...  
65                                     , 'phi', 0);
```

And lets plot it on the acquired CCD images:

```
63 figure(figure_window)  
64 for i=1:numel(Experiments)  
65     subplot(numel(Images),1,i)  
66     % We want to retain current graph in figure  
67     hold on  
68     calc_image(i)= plot( Out{i}.X_P(:) ,Out{i}.Z_P(:),'.r','MarkerSize',4);  
69 end
```

APPENDICES



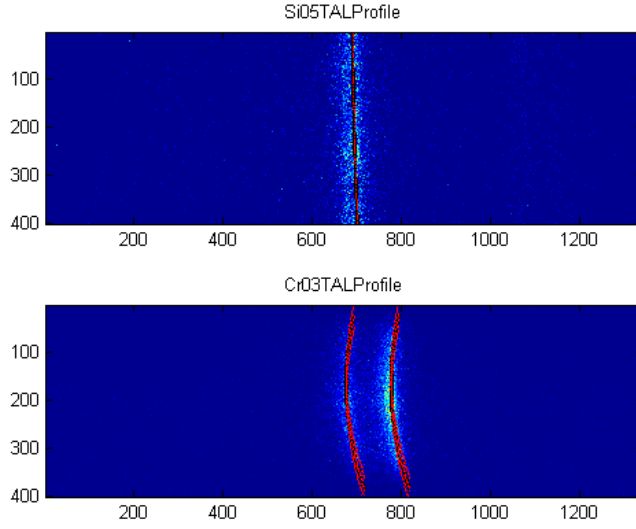
We can easily see that calculated and measured images are not aligned.

E.3 Parameters correction

If we play a bit with the parameters we find that a very good alignment can be found with the following corrections:

- vertical displacement of the beam spot $Z = 6$ mm,
- vertical displacement of the crystal $Z_{\text{crystal}} = -7.9$ mm,
- crystal rotation around parallel to x-axis $\text{rotX} = -2.35^\circ$,
- crystal rotation around parallel to y-axis $\text{rotY} = -0.8^\circ$,
- crystal rotation around parallel to z-axis $\text{rotZ} = 0.7^\circ$,
- crystal x position $\Delta R = 0.73$ mm.

```
70 delete(calc_image)
71 figure.figure_window)
72 for i=1:numel(Experiments)
73     [~,Out{i},Good_Params{i}] =vonHamosSpot(Params{i}...
74         , 'Z',Params{i}.Z + 6 ...
75         , 'Z_crystal',-7.9 ...
76         , 'rotX',-2.35/360*2*pi ...
77         , 'rotY',-0.8/360*2*pi...
78         , 'rotZ',0.7/360*2*pi...
79         , 'R',Params{i}.R + 0.73 ...
80     );
81     subplot(numel(Experiments),1,i)
82     hold on
83     calc_image(i)= plot( Out{i}.X_P(:) ,Out{i}.Z_P(:),'.r','MarkerSize',4);
84 end
```

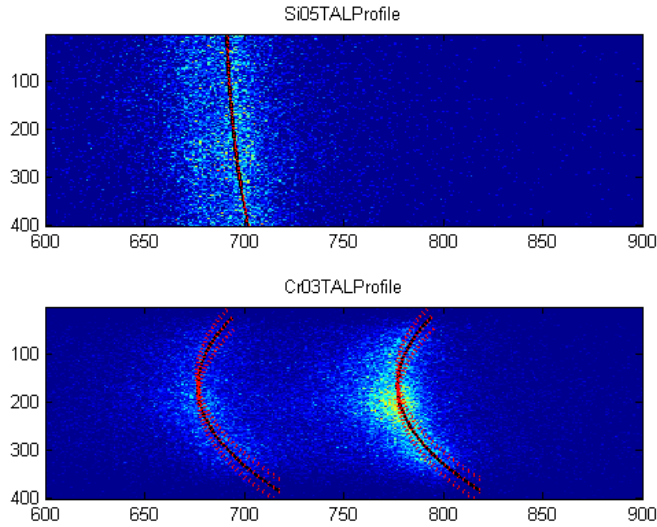



A closer look to the image spots:

```

85 figure.figure_window
86 for i=1:numel(Images)
87     subplot(numel(Images),1,i)
88     xlim([600,900])
89 end

```



It should be noted however that finding correct parameters is not an unambiguous problem and a similar alignment can be found for different parameters.

E.4 CCD image transformation

The images can be transformed by means of parametric arrays of a CCD image dimensions. Such arrays can be returned by `vonHamosSpot` function if the `MAP` parameter is set to `true`

`\ref{chap: vonHamosSpot_function}`

. Lets repeat the spectrometer parameters calculations once again and calculate the photon energies from `Bragg_MAP` parametric array using the Bragg law:

APPENDICES

```

90 E_Map=cell(2,1);
91 for i=1:numel(Experiments)
92     [~,Out{i}] =vonHamosSpot(Good_Params{i},'MAP',true);
93     % photon energy parametric array:
94     E_Map{i} = i * hc ./ x2d ./ sin(Out{i}.Bragg_MAP)/1000;
95 end

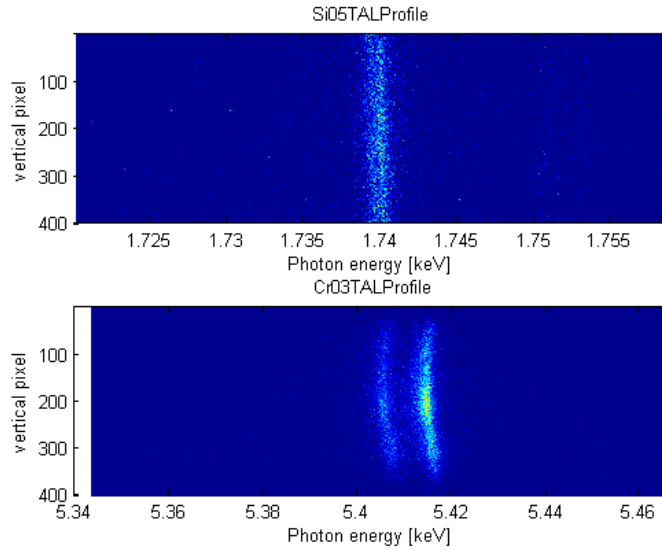
```

At first lets present the CCD images with the x axis transformed to photon energies corresponding to central pixels.

```

96 for i=1:numel(Experiments)
97     subplot(numel(Experiments),1,i)
98     cla
99     surf(E_Map{i}(200,:),1:400,Images{i}*0,Images{i},'LineStyle','none') ;
100     view([0,0,1])
101     xlabel('Photon energy [keV]')
102     ylabel('vertical pixel')
103     xlim([min(E_Map{i}(:)), max(E_Map{i}(:))])
104 end

```



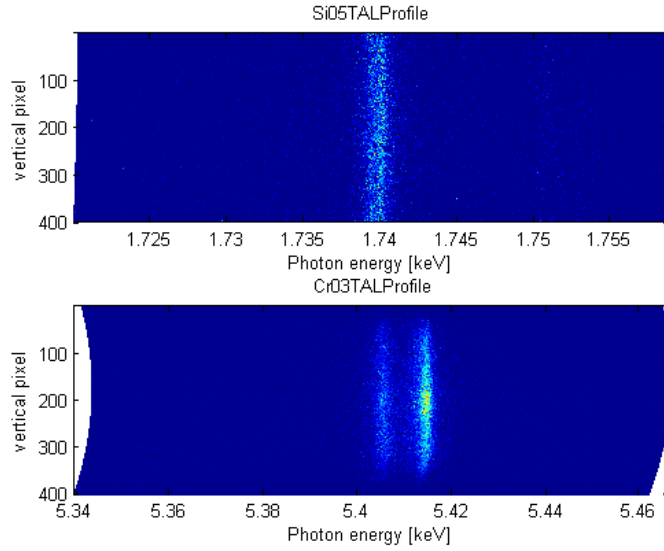
And now lets apply the full photon energy E_Map parametric array correction:

```

105 for i=1:numel(Experiments)
106     subplot(numel(Experiments),1,i)
107     cla
108     surf(E_Map{i},1:400*ones(1,1340),Images{i}*0,Images{i},...
109         'LineStyle','none');
110     view([0, 0,1])
111 end

```

E SPECTROMETER PARAMETERS CORRECTION

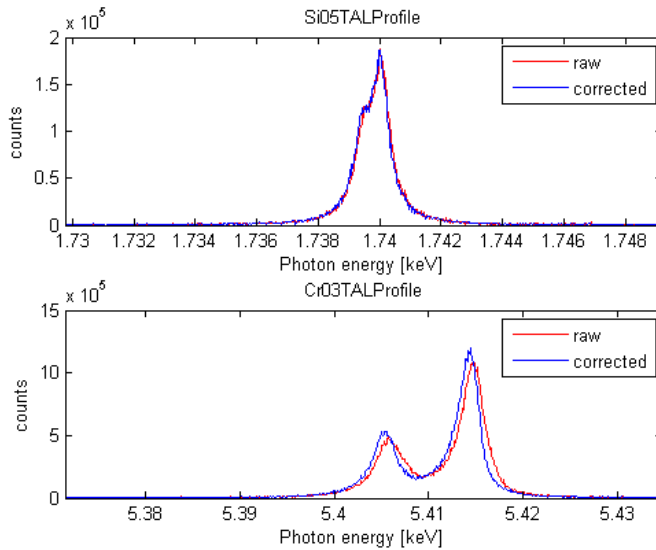


We can see that the spectral lines are now straight along the photon energy. Finally we can compare the histogram spectrum of measured fluorescence lines.

```

112 for i=1:numel(Experiments)
113     subplot(numel(Experiments),1,i)
114     cla
115     hold on
116     plot(E_Map{i}(200,:),sum(Images{i},1),'r','DisplayName','raw')
117     [~,bin] = histc(E_Map{i},E_Map{i}(200,:));
118     corrected_spectrum = arrayfun(@(a) sum(Images{i}(bin == a)),1:1340);
119     plot(E_Map{i}(200,:),corrected_spectrum,'Displayname','corrected')
120     ylabel('counts')
121     ylim('auto')
122     xlim([1/4,3/4] * diff(xlim) + min(xlim))
123     legend('show')
124     view([0, 0,-1])
125 end

```



Histogram of the corrected images is plotted with blue lines, the raw data histogram is presented with red lines. For the case of Cr the gain on energy resolution is evident.

Appendix F

GEXRF profile creation

In this tutorial we will present how to create a GEXRF profile out of `.spe` file series. We will use the spectrometer parameters that have been found in

Spectrometer parameters correction
tutorial.

Contents

F.1	File reading	169
F.2	Parametric arrays creation	170
F.3	Verification of the spectrometer parameters corrections	171
F.4	CCD height dependent GEXRF profile	172
F.5	Energy resolved GEXRF profile	173
F.5.1	CCD image transformations	173
F.5.2	Sum of CCD images	175

F.1 File reading

We will create a GEXRF profile out of files registered in `Cr03TALProfile` experiment:

```
1 Experiment = 'Cr03TALProfile' ;
```

The experiment files are located in the following folder:

```
2 % folder = '~/MI-1108/MI-1108/' ; % Unix path
3 folder = 'Z:\MI-1108\MI-1108\'; % Windows path
```

In order to select appropriate files (`.spe`) we will use the `choose_files` function.

```
3 file_list = choose_files(Experiment, '.spe', folder);
```

Now we can wrap the data into matlab workspace using the `spe_read` function. To speed up the code we will use the `parfor` loop that take advantage of parallel computing on multi CPU machines.

```
4 Profile = cell(numel(file_list),1);
5 parfor j = 1:numel(file_list)
6     frames = spe_read(file_list{j}, folder);
7     % overall intensity neglecting the background:
8     Profile{j} = sum(frames{1}.*(frames{1}>134),3);
9 end
```

The last thing is to read the TAL positions that are stored in a second column of a `Cr03Cr03TALProfile1p.spe.txt` file.

```
10 TAL = dir([folder, '*', Experiment, '*.txt']);
11 TAL = importdata([folder, TAL.name]);
12 if isstruct(TAL)
13     TAL = TAL.data;
14 end
15 TAL = TAL(1:numel(file_list),2);
```

F.2 Parametric arrays creation

In order to create parametric arrays we will use parameters from the `Good_Params{2}` structure adjusting them for the correct motors positions that have been used for `Cr03TALProfile` experiment:

- DET = 159129,
- CRY = 79565,
- TAF = 6341,
- TAT = 10012,
- TAL from `Cr03Cr03TALProfile1p.spe.txt` file.

The Bragg angles should be the same for all TAL positions, however exit angles `phi` and radiation direction `theta` can vary. In order to estimate the change of this parameters across GEXRF scan we will compare the parametric arrays for the first and the last file.

```

16 load('Good_Params')
17 [~,out(1)] = vonHamosSpot( Good_Params{2} ...
18     , 'MAP', true ...
19     , 'DET', 159129 ...
20     , 'CRY', 79565 ...
21     , 'TAF', 6341 ...
22     , 'TAT', 10012 ...
23     , 'TAL', TAL(1) );
24 [~,out(2)] = vonHamosSpot( Good_Params{2} ...
25     , 'MAP', true ...
26     , 'DET', 159129 ...
27     , 'CRY', 79565 ...
28     , 'TAF', 6341 ...
29     , 'TAT', 10012 ...
30     , 'TAL', TAL(end) );
31 phi1 = (out(1).phi_MAP-max(out(1).phi_MAP(:)))/2/pi*360;
32 phi2 = (out(2).phi_MAP-max(out(2).phi_MAP(:)))/2/pi*360;
33 exit_angle_delta = max(abs(phi1(:)-phi2(:)))

exit_angle_delta =
    0.0106

34 theta1 = (out(1).theta_MAP-max(out(1).theta_MAP(:)))/2/pi*360;
35 theta2 = (out(2).theta_MAP-max(out(2).theta_MAP(:)))/2/pi*360;
36 radiation_direction_delta = max(abs(theta1(:)-theta2(:)))

radiation_direction_delta =
    0.0027

```

The differences are not very pronounced. Thus we can use only one set of parametric arrays for all the files of the experiment. To optimize the resulting error the middle file parameters will be chosen for calculations.

```

37 [~,out(3)] = vonHamosSpot( Good_Params{2} ...
38     , 'MAP', true ...
39     , 'DET', 159129 ...
40     , 'CRY', 79565 ...
41     , 'TAF', 6341 ...
42     , 'TAT', 10012 ...
43     , 'TAL', TAL(floor(end/2)) );
44 phi3 = (out(3).phi_MAP-max(out(3).phi_MAP(:)))/2/pi*360;
45 theta3 = (out(3).theta_MAP-max(out(3).theta_MAP(:)))/2/pi*360;
46 exit_angle_delta = max([max(abs(phi1(:)-phi3(:)))...
47     ,max(abs(phi2(:)-phi3(:)))...
48     ])
49 radiation_direcion_delta = max([max(abs(theta1(:)-theta3(:)))...
50     ,max(abs(theta2(:)-theta3(:)))...
51     ])
52 out = out(3);

exit_angle_delta =
    0.0054
radiation_direcion_delta =
    0.0015

```

Now we will extract parametric arrays from out variable. We will define the exit angle and radiation direction parametric arrays (in degrees) and photon energy parametric array. The latter we will create out of out.Bragg_MAP using, as in

`\ref{chap:Spectrometer_parameters_correction}`

, the Bragg law:

$$E = \frac{nhc}{2d \sin \theta_B}$$

and knowing that Bragg reflection order $n = 2$ and that double spacing between the crystal lattice planes $2d = 8.5096$.

```

53 x2d = 8.5096;
54 hc = 4.135667516e-15 * 299792458e10;
55 % photon energy parametric array in keV:
56 E_MAP = 2*hc ./ x2d ./ sin(out.Bragg_MAP)/1000;
57 % radiation direction parametric array in degrees:
58 Theta = out.theta_MAP/2/pi*360;
59 % exit angle parametric array in degrees:
60 Phi = out.phi_MAP/2/pi*360;

```

The overall shift of the exit angle distribution with changing TAL motor position needs to be taken into consideration. This can be done by calculating the exit angle shift relative to the middle TAL position.

```

58 relative_angle = (TAL-TAL(floor(end/2)))*0.00225;

```

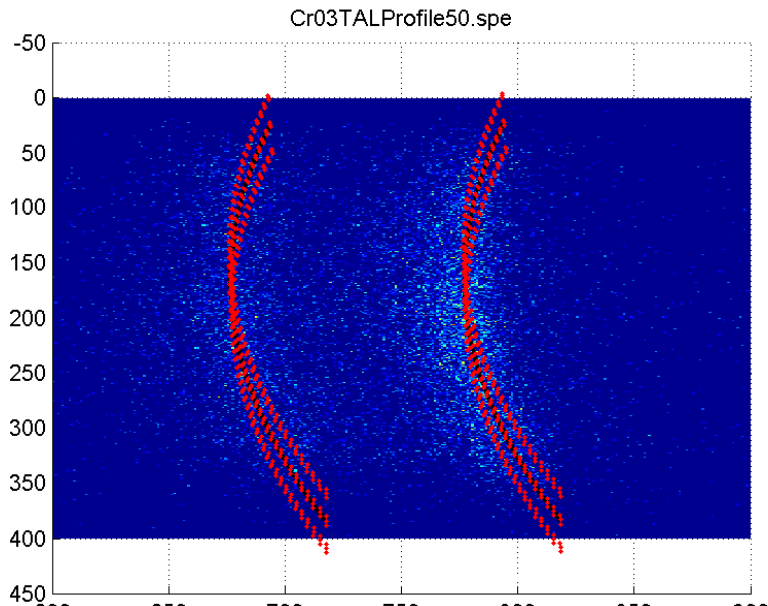
F.3 Verification of the spectrometer parameters corrections

Lets have a look at the last file from the file series and lets compare it with the calculated image form:

```

59 CCD_image_fig = figure;
60 surf(Profile{end},'LineStyle','none') ;
61 view([0, 0,-1])
62 hold on
63 plot(squeeze(out.X_P(:,5,:)),squeeze(out.Z_P(:,5,:)),'-k','LineWidth',2);
64 plot( out.X_P(:),out.Z_P(:),'r','MarkerSize',4);
65 xlim([600,900])
66 title(file_list(end))

```



We can see that the form of the image is very well reproduced.

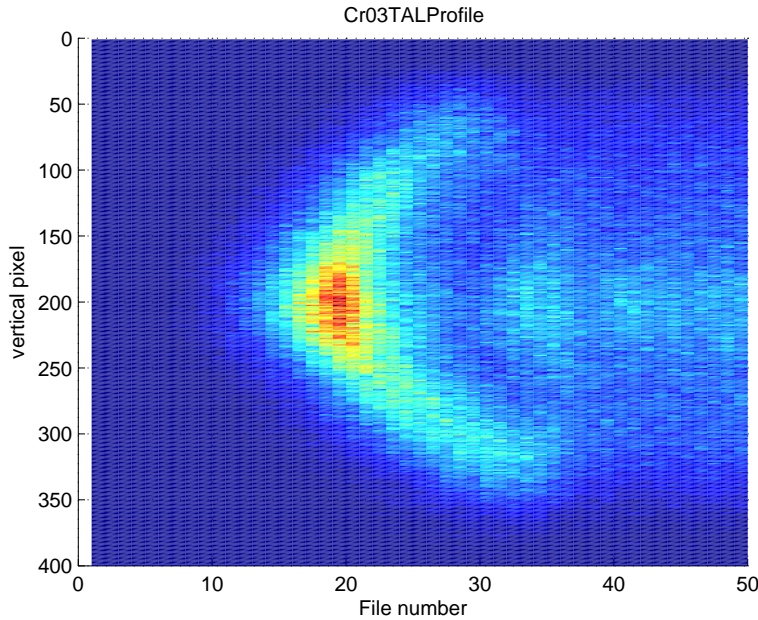
F.4 CCD height dependent GEXRF profile

We can try to plot the GEXRF profile summing the CCD pixels along x direction and drawing it for each file as a one pixel wide column of height dependent integral intensity. The GEXRF profile will be a picture of a CCD height and width corresponding to number of files. In order to increase the angular resolution we will sum the CCD only over the region of the $K\alpha^1$ line occurrence *i.e.* in the [740:840] x pixel range.

```

67 GEXRF_Profile_fig = figure;
68 GEXRF_Profile = cellfun(@(x) sum(x(:,740:840),2),Profile,...
69                               'UniformOutput',false);
70 GEXRF_Profile = [GEXRF_Profile{:}];
71 surf(GEXRF_Profile,'LineStyle','none')
72 view([0, 0,-1])
73 title(Experiment)
74 xlabel('File number')
75 ylabel('vertical pixel')
76 hold on

```



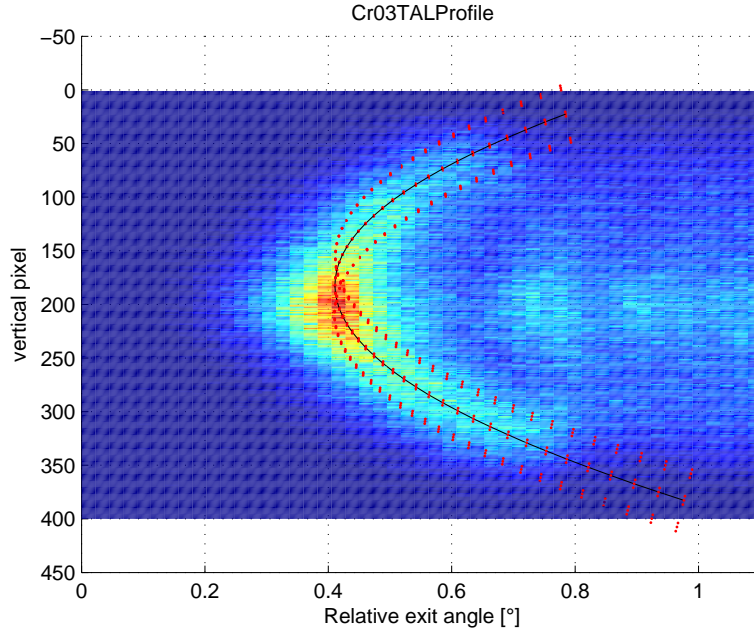
We can clearly see that exit angle evolution depends on the vertical position on the CCD. The intensity raises quickest for pixels around 200.

Now we can compare the GEXRF profile with calculated distribution of exit angles. This time the x axis will represent the fluorescence radiation exit angle relative to the first measurement position. The calculated distribution of exit angles will be shifted to cross over peak of maximal GEXR intensity. We will see that also in that case the calculated shape fits well the measured data.

```

77 figure(GEXRF_Profile_fig);cla;hold on
78 surf(relative_angle-min(relative_angle),1:400,...
79       GEXRF_Profile,'LineStyle','none')
80 plot( (max(max(out.phi(:,1))) - out.phi(:,5,1)) /2/pi*360 + 0.41,...
81       out.Z_P(:,5,1),'k');
82 plot( (max(max(out.phi(:,1))) - out.phi(:,1,1)) /2/pi*360 + 0.41,...
83       out.Z_P(:,1,1),'r','MarkerSize',4);
84 xlabel('Relative exit angle [$^\circ$]')
85 ylabel('vertical pixel')
86 xlim([relative_angle(1),relative_angle(end)]-min(relative_angle))

```

F.5 Energy resolved GEXRF profile

The standard way to extract angular dependent GEXRF data is to reduce the ROI of the CCD only to central pixels in y direction and, in x direction, only to pixels upon occurrence of considered fluorescence line. Such a procedure solves the problem of not uniform exit angle value across the y dimension of the CCD. However the count rate loss is significantly decreased. Moreover the exit angle resolution is not optimal due to the integration over the width of a spectral line (the exit angle change along x direction of a CCD is equal to the Bragg angle change). In case of a Cr $K\alpha^1$ line it is about:

```
87 range(Phi(200,760:788))
```

```
ans =  
0.0176
```

which is three times more than the error on the exit angle distribution `exit_angle_delta`.

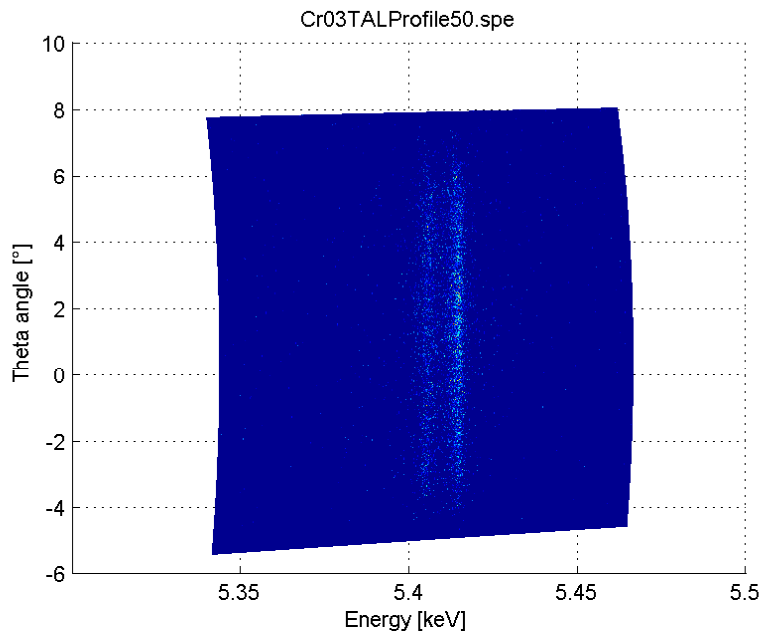
In order to increase both the count rate and the angular resolution we will transform the CCD images using the calculated parametric arrays.

F.5.1 CCD image transformations

Lets have a look at the last CCD image with the y axis transformed to radiation direction **Theta**:

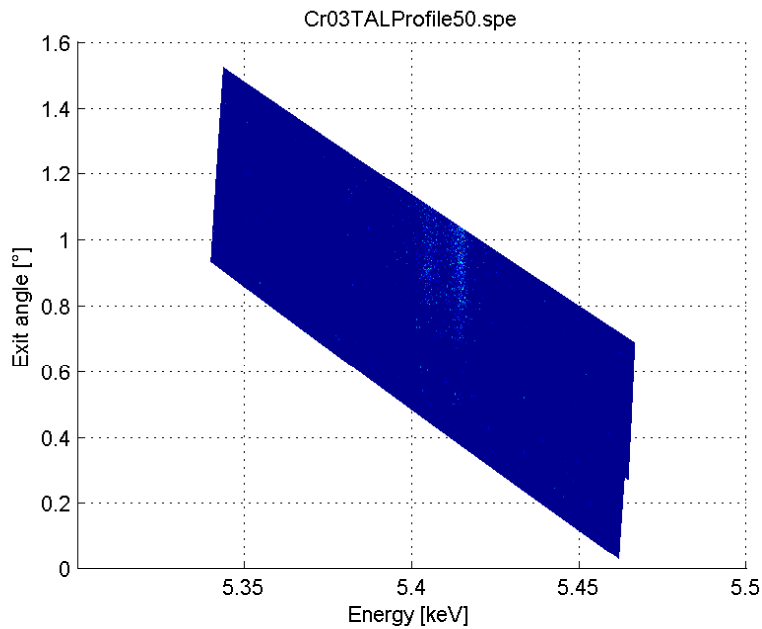
```
88 figure(CCD_image_fig);  
89 cla  
90 surf(E_MAP,Theta,Phi+relative_angle(end),Profile{end},'LineStyle','none');  
91 view([0, 0,1])  
92 xlabel('Energy [keV]')  
93 ylabel('Theta angle [^\circ]')  
94 zlabel('Exit angle [^\circ]')  
95 axis('auto')
```

APPENDICES



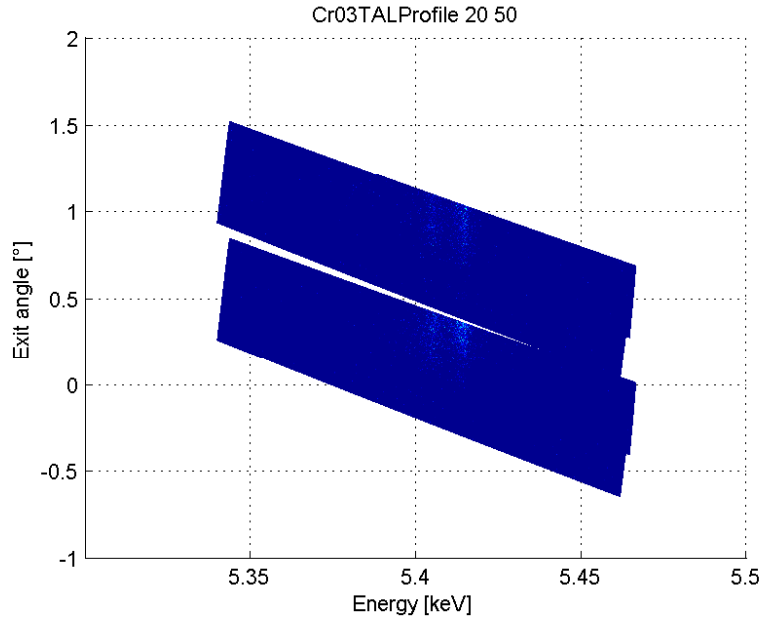
and now with the y axis transformed to exit angle Phi:

```
96 view([0,-1,0])
```



We can plot additional CCD images in the same figure, for instance Cr03TALProfile20:

```
97 hold on
98 surf(E_MAP,Theta,Phi+relative_angle(20),Profile{20},'LineStyle','none');
99 title( [Experiment , sprintf(' %d',20,numel(Profile))] )
```



We will get the energy resolved GEXRF profile by summing all the transformed CCD images along the exit angle axis.

F.5.2 Sum of CCD images

In order to sum the CCD images along the exit angle axis we need to define an image partition grid over which we will sum the pixels intensity. It is an arbitrary choice. For this tutorial we will choose:

- exit angle partition with the interval equating the exit angle error `exit_angle_delta`,
- radiation direction partition with a 1° interval,
- photon energy partition equating the energy corresponding to middle pixels `E_MAP(200,:)`.

```

100 Phi_all = min(Phi(:)+relative_angle(1)) ...
101       : exit_angle_delta ...
102       : max(Phi(:)+relative_angle(end));
103 Theta_range = ceil(min(Theta(:)))-.5:.3: floor(max(Theta(:)))+.5;
104 E_range = E_MAP(200,:);

```

Pixels need to be assign to appropriate cells of the partition grid. The row end column indexes of a pixel can be found using the `histc` function. The sum of pixels intensity over cells can be performed with `accumarray` function with partition grid indexes of all pixels given as a first argument and the CCD pixel intensities as a second one. Finally, in order to create an overall GEXRF profile, all the single CCD histograms should be summed up.

```

105 % pixel indexes in energy dimension:
106 [~,E_bin] = histc(E_MAP,E_range);
107 % pixel indexes in radiation direction dimension:
108 [~,T_bin] = histc(Theta,Theta_range);
109 % preallocation of the GEXRF_Profile2 array:
110 GEXRF_Profile2 = zeros( numel(Phi_all) , max(E_bin(:)) , max(T_bin(:)));
111 for i = 1:numel(Profile)
112     % pixel indexes in exit angle dimension:
113     [~,Phi_bin] = histc(Phi+relative_angle(i),Phi_all);
114     %Single image histogram:
115     CCD_histogram = accumarray({Phi_bin(:)+1 , E_bin(:)+1 , T_bin(:)+1},...
116                               Profile{i}(:));
117     % summed GEXRF profile:
118     GEXRF_Profile2(1:max(Phi_bin(:)),:,:) = ...
119         GEXRF_Profile2(1:max(Phi_bin(:)),:,:)...
120         + CCD_histogram(2:end,2:end,2:end);
121 end

```

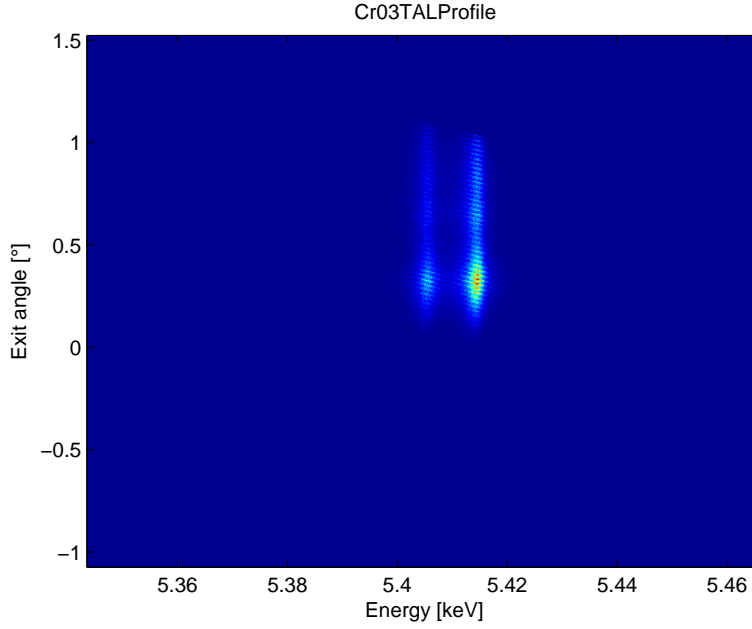
Lets image the result as an energy resolved GEXRF profile of a full CCD:

APPENDICES

```

119 GEXRF_Profile2_fig = figure;
120 imagesc(E_range,Phi_all,squeeze( sum( GEXRF_Profile2,3)));
121 title(Experiment)
122 xlabel('Energy [keV]')
123 ylabel('Exit angle [ $^\circ$ ]')
124 set(gca,'YDir','normal')

```

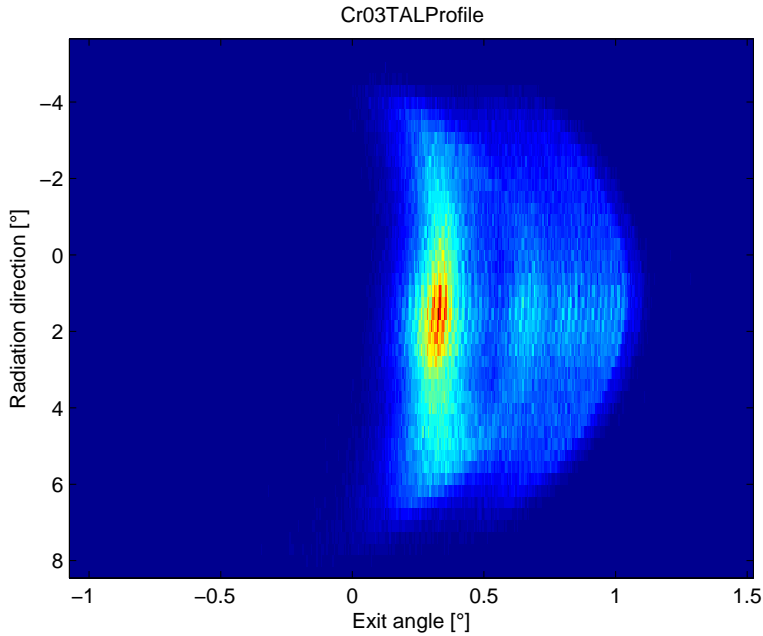


An now lets plot GEXRF profiles for different radiation directions:

```

125 imagesc(Phi_all,Theta_range,squeeze(sum(GEXRF_Profile2,2))');
126 title(Experiment)
127 xlabel('Exit angle [ $^\circ$ ]')
128 ylabel('Radiation direction [ $^\circ$ ]')

```



Acknowledgments

Here I would like to thank all the people who helped and supported me during my PhD project.

First of all, I would like to thank my PhD supervisor Prof. Dr. Jean-Claude Dousse. I highly appreciate his support and care during my study and his great help in the PhD thesis redaction.

I also thank all my colleagues from the [AXP](#) research group at the University of Fribourg. In particular I thank Dr. hab. Joanna Hoszowska for her help in experiments preparation and their realization, her advices on the von Hamos spectrometer setup and also for her agreement to be the referee of my thesis. I thank Dr. Wei Cao, Dr. Yves Kayser, and Wojciech Błachucki for their support and invaluable help during the experiments. I thank Yves-Patrick Maillard for his hospitality and serenity.

It is my pleasure to thank Prof. Dr. Marek Pajek for his priceless advices and fruitful discussions about results and interpretation and in particular for his agreement to be the referee of my thesis. I would also like to thank all the members of Prof. Pajek group at the Jan Kochanowski University – Dr. Aldona Kubala-Kukuś, Dr. Dariusz Banaś, Paweł Jagodziński, Łukasz Jabłoński, and Katarzyna Deja – that helped me a lot during the experiments and always supported my scientific progress.

I am obliged to express my gratitude to Dr. Jakub Szlachetko without whom the [GO](#) ray tracing model would never get functional.

I would like to thank members of the research group of Dr. Burkhard Beckhoff at [PTB](#) for their interest and help in research. In particular I would like to thank Falk Reinhardt and Philipp Hoenicke that have both solemnly participated in experiments and shared their great [GIXRF](#) experience. Special thanks should be addressed to Falk

ACKNOWLEDGMENTS

Reinhardt who has performed all the presented [GIXRF](#) measurements and who provided me with the following Figures: [I.2](#), [II.B.4](#), [II.B.5](#), [II.C.1](#), [II.C.2](#), [III.D.1](#), [III.D.2](#), [IV.A.3](#), and [IV.A.4](#).

I would also like to thank Prof. Dr. L. T. Baczewski, Institute of Physics of the Polish Academy of Sciences, Dr. Andreea Veronica Savu, and Prof. Dr. T. Luciński who have all provided me with samples.

Many thanks to the mechanical workshop headed by Oswald Raetzo. My PhD project couldn't be accomplished if it wasn't for their great and keen work. I thank Dr. Ivan Marozau, for the [AFM](#) measurements. I also thank Dr. Murielle Salomé and all the ID21 staff.

Finally I would like to give thanks to my wife and children without whom all this work would seem to me totally useless; and to my whole family: my parents, brothers, sister and grandmothers who have always supported and believed in me.

Curriculum Vitae

Stanisław Henryk NOWAK

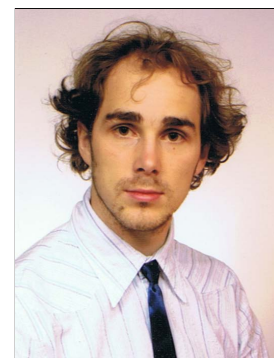
CONTACT

Professional:

address: University of Fribourg
Department of Physics
Ch. du Musée 3
CH-1700 Fribourg
Switzerland
tel.: +41 (0) 26 300 9027
fax: +41 (0) 26 300 9447
e-mail: stanislaw.nowak@unifr.ch

Private:

address: Route des Cliniques 37
CH-1700 Fribourg
Switzerland
mob.: +41 (0) 78 691 3053
e-mail: stasiulo@gmail.com



PERSONAL

nationality: Polish date of birth: May 13th 1983
marital status: married, two children place of birth: Kielce, Poland

EDUCATION

University of Fribourg, Fribourg, Switzerland

Oct 2008 – Dec 2012 Department of Physics

- **PhD** thesis in physics:
Investigation of surface nanostructures with grazing angle x-ray fluorescence techniques

University of Warsaw, Warsaw, Poland

Sep 2002 – Jul 2008 College of Inter-Faculty Individual Studies In Mathematics and Natural Sciences

- **MSc** thesis in solid state physics:
Studies of photoluminescence dynamics of quantum dots in semiconductor heterostructures of the type II-VI
- **BSc** thesis in mathematics:
A vortex around a square island

Scholarships and Courses:

- **Hercules Specialized Course HSC10**, ESRF, Grenoble, France
Synchrotron Radiation Techniques contribution to Nanoscience
- **Université Paris Nord (Paris XIII)**, Saint-Denis, France
Socrates-Erasmus scholarship

May 2009

Feb – Jun 2006

EMPLOYMENT

University of Fribourg, Fribourg, Switzerland

Oct 2008 – present assistant

RESEARCH EXPERIENCE

Oct 2008 – present **University of Fribourg**, Fribourg, Switzerland

- development of the high-resolution Grazing Emission X-ray Fluorescence (GEXRF) spectroscopy
- development of the geometrical optics based GEXRF/GIXRF numerical model
- development of the resolution enhancement algorithm for the GEXRF spectroscopy
- metallic nanostructures fabrication with a lift-off technique
- HV experimental setup

Sep 2002 – Jul 2008 **University of Warsaw**, Warsaw, Poland

- photoluminescence studies of quantum dots dynamics and photons correlation
- development of the quantum dots dynamics numerical model
- single photon spectroscopy
- use of a femtosecond laser probe and cryogenic experimental setup

user of:

- **Center of Micronanotechnology (CMI)**, EPFL, Lausanne, Switzerland
- **Swiss Light Source (SLS)**, PSI, Villigen, Switzerland
- **European Synchrotron Radiation Facility (ESRF)**, Grenoble, France

2012 – present
2011 – present
2008 – present

AWARDS

14th Conference on Total Reflection X-Ray Fluorescence and Related Methods (TXRF 2011), Dortmund, Germany.

June 2011 **best poster award** (second place)

LANGUAGES

fluent: **Polish** (native), **English**, **French**
basic: Italian, Greek

INTERESTS

- classical music, jazz (classical guitar college alumnus, University of Warsaw Choir former member)
- sailing (Inland Skipper), alpine skiing

EXTERNAL EXPERIMENTS

SLS, PSI, Villigen, Switzerland

- Nov 2011 • **S. H. Nowak**, J.-Cl. Dousse, J. Hoszowska, Y. Kayser, D. Banaś, and M. Pajek. *Investigation of surface nanostructures with plane symmetries by means of the SR based high-resolution GEXRF technique*, proposal no. 20110766.
- Oct 2011 • J. Hoszowska, J.-Cl. Dousse, Y. Kayser, and **S. H. Nowak**. *Multi-electron transitions following single-photon double K-shell ionization*, proposal no. 20110245.

ESRF, Grenoble, France

- Nov 2011 • **S. H. Nowak**, J.-Cl. Dousse, Y. Kayser, A. Kubala-Kukuś, M. Pajek, D. Banaś, P. Jagodziński, and J. Szlachetko. *Application of the synchrotron radiation based high-resolution GEXRF for studies of periodic surface nanostructures*, proposal no. MI-1108.
- Apr 2010 • Y. Kayser, J. Hoszowska, D. Banaś, P. Jagodziński, M. Pajek, W. Cao, J.-Cl. Dousse, **S. Nowak**, and A. Kubala-Kukuś. *Depth-profiling of relevant dopants implanted at low energies in Si and Ge by using synchrotron radiation based high-resolution micro-GEXRF*, proposal no. MI-1059.
- Apr 2010 • J. Szlachetko, A. Kubala-Kukuś, M. Pajek, J.-Cl. Dousse, Y. Kayser, and **S. H. Nowak**. *Single-photon double-and triple-ionization: energy dependence study of the KL and KLL excited states in low-Z elements*, proposal no. HE-3488.
- Apr 2009 • J. Hoszowska, J.-Cl. Dousse, Y. Kayser, W. Cao, **S. Nowak**, M. Pajek, A. Kubala-Kukuś, J. Szlachetko, D. Banaś, and P. Jagodziński. *Investigation of the morphology of surface nanostructures by high-resolution grazing emission x-ray fluorescence*, proposal no. MI-975.
- Feb 2009 • J. Hoszowska, Y. Kayser, P. Jagodziński, W. CAO, J.-Cl. Dousse, **S. Nowak**, M. Kavčič, and J. Szlachetko. *Two-electron one-photon x-ray transitions in Al and Si following double K-shell photoionization*, proposal no. HE-3194.
- Jan 2009 • S. Butorin, A. Modin, V. Ilakovac, J. Nordgren, J. Szlachetko, M. Kavčič, M. Simon, L. Journel, A. Mihelic, J. Vegelius, J. Hoszowska, Y. Kayser, M. ZITNIK, W. Cao, K. Bucar, J.-Cl. Dousse, **S. Nowak**, R. Guillemin, B. Kanngiesser, B. Beckhoff, and A. Karydas. *RIXS and XES studies of isolated atoms, molecules, and novel (nano)materials in the intermediate x-ray energy range*. proposal no. HE-3098.

PRESENTATIONS

Oral presentations:

- **S. Nowak**, M. Goryca, T. Kazimierzczuk, J. A. Gaj, A. Golnik, P. Kossacki, G. Karczewski, and P. Wojnar *Kropka kwantowa jako źródło pojedynczych fotonów*, (UJK, Kielce, Poand), 15 Apr 2009. (seminar)
- **S. Nowak**, M. Goryca, T. Kazimierzczuk, J. A. Gaj, A. Golnik, P. Kossacki, P. Wojnar, and G. Karczewski, *Single-photon emission from a highly excited CdTe quantum dot*, XXXVII International School on the Physics of Semiconducting Compounds Jaszowiec 2008, (Ustron-Jaszowiec, Poland), p. 35, June 7-13 2008.

Poster presentations:

- **S. H. Nowak** and W. K. Podleski, *Grazing incidence x-ray technique for assessment of immune system* European Academy of Allergy & Clinical Immunology, EAACI Congress 2012, Geneva, Switzerland, 16 - 20 June 2012.
- **S. H. Nowak**, Y. Kayser, D. Banaś, W. Cao, K. Deja, J.-Cl. Dousse, J. Hoszowska, M. Pajek, and J. Szlachetko *Effects of the sample surface roughness in grazing emission x-ray fluorescence measurements*, 43rd conference of the European Group for Atomic Systems (EGAS), Fribourg, Switzerland, 28 June - 2 July 2011.
- **S. H. Nowak**, F. Reinhardt, H. Bresch, Y. Kayser, J. Osán, and A. E. Pap, *Geometrical optics modelling of grazing incidence x-ray fluorescence of nanostructured objects*, 14th Conference on Total Reflection X-Ray Fluorescence Analysis and Related Methods (TXRF 2011), Dortmund, Germany, 06-09 June 2011.
- **S. Nowak**, Y. Kayser, L. Baczewski, D. Banaś, W. Cao, K. Deja, J.-Cl. Dousse, J. Hoszowska, M. Pajek, A. Petroutchik, J. Szlachetko, and A. Wawro *Analysis of surface nanostructures via the SR-based high-resolution GEXRF technique*, in 10th European Conference on Atoms, Molecules and Photons (ECAMP 10), Salamanca, Spain, 4-9 July 2010.
- **S. Nowak**, D. Banaś, W. Cao, J.-Cl. Dousse, J. Hoszowska, Y. Kayser, A. Kubala-Kukuś, M. Pajek and J. Szlachetko *Synchrotron radiation based high-resolution grazing-emission x-ray fluorescence: a multipurpose surface characterization method*, XXXIX International School and Conference on the Physics of Semiconductors Jaszowiec 2010, Krynica-Zdrój, Poland, 21-24 June 2010.
- **S. Nowak**, Y. Kayser, L. Baczewski, D. Banaś, W. Cao, J.-Cl. Dousse, J. Hoszowska, M. Pajek, A. Petroutchik, J. Szlachetko, and A. Wawro *The synchrotron radiation based high-resolution grazing emission x-ray fluorescence technique for surface morphology analysis*, HERCULES XX Workshop, Grenoble, France, 25-26 March 2010.
- **S. Nowak**, Y. Kayser, L. Baczewski, D. Banaś, W. Cao, K. Deja, J.-Cl. Dousse, J. Hoszowska, M. Pajek, and J. Szlachetko *SR-based high-resolution GEXRF investigation of the morphology of surface nanostructures*, Hercules Specialized Courses (HSC10), Synchrotron radiation techniques contribution to nanoscience, ESRF, Grenoble, France, 18-22 May 2009.
- **S. Nowak**, Y. Kayser, L. Baczewski, D. Banaś, W. Cao, K. Deja, J.-Cl. Dousse, J. Hoszowska, M. Pajek, A. Petroutchik, J. Szlachetko, and A. Wawro, *Investigation of the morphology of surface nanostructures by means of the synchrotron radiation based high-resolution GEXRF technique*, XXXVIII International School and Conference on the Physics of Semiconductors (Jaszowiec 2009), Krynica-Zdroj, Poland, 19-26 June 2009.
- **S. Nowak**, T. Jakubczyk, M. Goryca, A. Golnik, P. Kossacki, P. Wojnar, and J. A. Gaj *Emission of self-assembled CdTe/ZnTe quantum dot samples with different cap thickness*, XXXVIII International School and Conference on the Physics of Semiconductors Jaszowiec 2009, Krynica-Zdrój, Poland, 19-26 June 2009.
- **S. Nowak**, J. Suffczyński, M. Goryca, P. Kossacki, J. Gaj, S. Lee, and J. Furdyna, *Influence of growth break before capping on photoluminescence dynamics of CdSe/ZnSe self-assembled quantum dots*, XXXVII International School on the Physics of Semiconducting Compounds Jaszowiec 2008, Ustron-Jaszowiec, Poland, 7-13 June 2008.

OTHER CONFERENCE CONTRIBUTIONS:

- J. Hoszowska, Y. Kayser, **S. H. Nowak**, and J.-Cl. Dousse, *High resolution grazing emission x-ray fluorescence technique: A powerful tool for material characterization*, in Denver X-Ray Conference, (Denver, USA), 6–10 August 2012.
- Y. Kayser, W. Blachucki, J.-Cl. Dousse, J. Hoszowska, M. Neff, **S. Nowak**, and V. Romano, *High-resolution micro-XRF and GEXRF applied to the investigation of the distribution of dopants in optical fibres*, in European Conference on X-Ray Spectrometry (EXRS 2012), (Vienna, Austria), 18–22 June 2012.
- F. Reinhardt, B. Beckhoff, B. Pollakowski, M. Kolbe, J. Osán, S. Török, M. Schoengen, **S. Nowak**, J.-Cl. Dousse, H. Bresch, S. Seeger, and U. Waldschläger, *Qualification of quantitative grazing incidence x-ray fluorescence for the analysis of nano-particular surface contamination*, in European Conference on X-Ray Spectrometry (EXRS 2012), (Vienna, Austria), 18–22 June 2012.
- J. Hoszowska, J.-Cl. Dousse, J. Szlachetko, W. Cao, P. Jagodziński, Y. Kayser, **S. H. Nowak**, and M. Kavčič, *Two-electron one-photon transitions of Mg, Al and Si in K-shell double photoionization*, in 43rd European Group for Atomic Systems (EGAS) Conference, (Fribourg, Switzerland.), p. 48, June 28 - July 2 2011.
- P. Jagodziński, D. Banaś, W. Cao, J.-Cl. Dousse, J. Hoszowska, Y. Kayser, A. Kubala-Kukuś, **S. Nowak**, M. Pajek, M. Salomé, and J. Szlachetko, *Investigations of speleothems by x-ray fluorescence microscopy using synchrotron radiation*, in 14th Conference on Total Reflection X-Ray Fluorescence Analysis and Related Methods (TXRF 2011), (Dortmund, Germany), June 06–09 2011.
- P. Jagodziński, D. Banaś, A. Kubala-Kukuś, M. Pajek, J. Szlachetko, W. Cao, J.-Cl. Dousse, J. Hoszowska, Y. Kayser, and **S. Nowak**, *Simulations of x-ray transmission in polycapillaries*, in 14th Conference on Total Reflection X-Ray Fluorescence Analysis and Related Methods (TXRF 2011), (Dortmund, Germany), June 06–09 2011.
- Y. Kayser, D. Banaś, W. Cao, J.-Cl. Dousse, B. Fayard, P. Hönicke, J. Hoszowska, P. Jagodziński, A. Kubala-Kukuś, **S. H. Nowak**, M. Pajek, and R. Unterumsberger, *Micro-focused synchrotron radiation based high-resolution GEXRF applied to the depth profiling of low energy implants of P, in and Sb in Si and Ge*, in 14th Conference on Total Reflection X-Ray Fluorescence Analysis and Related Methods (TXRF 2011), (Dortmund, Germany), June 06–09 2011.
- Y. Kayser, D. Banaś, W. Cao, J.-Cl. Dousse, P. Hönicke, J. Hoszowska, P. Jagodziński, A. Kubala-Kukuś, **S. H. Nowak**, M. Pajek, and R. Unterumsberger, *Depth profiling of low energy P, In and Sb implants using synchrotron radiation based high-resolution micro-GEXRF*, in 43rd European Group for Atomic Systems (EGAS) Conference, (Fribourg, Switzerland.), p. 77, June 28–July 2 2011.
- J. Hoszowska, J.-Cl. Dousse, J. Szlachetko, W. Cao, P. Jagodziński, Y. Kayser, **S. Nowak**, and M. Kavčič, *First observation of two-electron one-photon transitions in single-photon impact*, in 37th International Conference on Vacuum UltraViolet and X-Ray Physics, (Vancouver, Canada), July 11–16 2010.
- J. Hoszowska, J.-Cl. Dousse, J. Szlachetko, W. Cao, P. Jagodziński, Y. Kayser, **S. Nowak**, and M. Kavčič, *Photon induced two-electron one-photon transitions*, in 7th International Conference on Inelastic X-Ray Scattering (IXS 2010), (Grenoble, France), Oct. 11–14 2010.
- Y. Kayser, D. Banaś, W. Cao, J.-Cl. Dousse, J. Hoszowska, P. Jagodziński, M. Kavčič, A. Kubala-Kukuś, **S. Nowak**, M. Pajek, and J. Szlachetko, *Depth profiling of dopants implanted in Si using the SR-based high-resolution grazing emission technique*, in 17th International Conference on Ion Beam Modification of Materials (IBMM 2010), (Montréal, Canada), August 21–27 2010.
- Y. Kayser, D. Banaś, W. Cao, J.-Cl. Dousse, J. Hoszowska, P. Jagodziński, M. Kavčič, A. Kubala-Kukuś, **S. Nowak**, M. Pajek, and J. Szlachetko, *SR-based high-resolution GEXRF, a new technique to determine the depth distribution of dopants implanted in semiconductors*, in European Conference on X-Ray Spectrometry (EXRS 2010), (Figueira da Foz, Coimbra, Portugal), p. 89, June 20–25 2010.
- Y. Kayser, W. Cao, J.-Cl. Dousse, J. Hoszowska, P. Jagodziński, M. Kavčič, A. Kubala-Kukuś, **S. Nowak**, M. Pajek, and J. Szlachetko, *Depth profiles of Al impurities implanted in Si wafers determined by means of the high resolution GEXRF technique*, in 13th Conference on Total Reflection X-Ray Fluorescence Analysis and Related Methods (TXRF 2009), (Gothenburg, Sweden), June 15–19 2009.
- M. Pajek, D. Banaś, W. Cao, J.-Cl. Dousse, J. Hoszowska, Y. Kayser, A. Kubala-Kukuś, **S. Nowak**, J. Szlachetko, M. Salomé, and J. Susini, *Synchrotron radiation based grazing emission x-ray fluorescence*, in 11th International Symposium on Radiation Physics (ISRP-11), (Melbourne, Australia.), September 21–27 2009.
- M. Pajek, D. Banaś, W. Cao, J.-Cl. Dousse, J. Hoszowska, Y. Kayser, A. Kubala-Kukuś, **S. Nowak**, J. Szlachetko, M. Salomé, and J. Susini, *Synchrotron-radiation based high-resolution grazing emission x-ray fluorescence – applications in nanoscience*, in 11th International Symposium on Radiation Physics (ISRP-11), (Melbourne, Australia.), September 21–27 2009.
- M. Pajek, D. Banaś, W. Cao, J.-Cl. Dousse, J. Hoszowska, Y. Kayser, A. Kubala-Kukuś, **S. Nowak**, J. Szlachetko, M. Salomé, and J. Susini, *Synchrotron radiation based grazing emission x-ray fluorescence*, in 11th International Symposium on Radiation Physics (ISRP-11), (Melbourne, Australia.), 15–19 June 2009.

PUBLICATIONS

- P. Hönicke, Y. Kayser, B. Beckhoff, M. Muller, J.-Cl. Dousse, J. Hoszowska, and **S. H. Nowak**. *Characterization of ultra shallow aluminum implants in silicon by grazing incidence and grazing emission x-ray fluorescence spectroscopy*, J. Anal. At. Spectrom. **27**:1432–1438, 2012.
- Y. Kayser, D. Banaś, W. Cao, J.-Cl. Dousse, J. Hoszowska, P. Jagodziński, M. Kavčič, A. Kubala-Kukuś, **S. Nowak**, M. Pajek, and J. Szlachetko. *Depth profiling of dopants implanted in si using the synchrotron radiation based high-resolution grazing emission technique*, X-Ray Spectrom. **41**(2):98–104, 2012.
- J. Hoszowska, J.-Cl. Dousse, J. Szlachetko, Y. Kayser, W. Cao, P. Jagodziński, M. Kavčič, and **S. H. Nowak**. *First observation of two-electron one-photon transitions in single-photon K-shell double ionization*, Phys. Rev. Lett. **107**(5) p. 053001, 2011.
- Y. Kayser, D. Banaś, W. Cao, J.-Cl. Dousse, J. Hoszowska, P. Jagodziński, M. Kavčič, A. Kubala-Kukuś, **S. Nowak**, M. Pajek, and J. Szlachetko. *Depth profiles of Al impurities implanted in Si wafers determined by means of the high-resolution grazing emission X-ray fluorescence technique*, Spectrochim. Acta, Part B **65**(6) :445–449, 2010.
- T. Kazimierzczuk, M. Goryca, M. Koperski, **S. Nowak**, P. Wojnar, A. Golnik, J. A. Gaj, and P. Kossacki. *Excitation dynamics of CdTe/ZnTe quantum dots studied in picosecond timescale*, AIP Conference Proceedings, **1199**(1):305–306, 2010.
- **S. Nowak**, T. Jakubczyk, M. Goryca, A. Golnik, P. Kossacki, P. Wojnar, and J. A. Gaj. *Emission of self-assembled CdTe/ZnTe quantum dot samples with different cap thickness*, Acta Phys. Pol., A **116**(5) 2009.
- **S. Nowak**, M. Goryca, T. Kazimierzczuk, J. A. Gaj, A. Golnik, P. Kossacki, P. Wojnar, and G. Karczewski. *Single-photon emission from a highly excited CdTe quantum dot*, Acta Phys. Pol., A **114**(5) p. 1273, 2008.
- **S. Nowak**, J. Suffczyński, M. Goryca, P. Kossacki, J. A. Gaj, S. Lee, and J. Furdyna. *Influence of growth break before capping on photoluminescence dynamics of CdSe/ZnSe self-assembled quantum dots*, Acta Phys. Pol., A **114**(5):1267–1271, 2008.
- T. Kazimierzczuk, **S. Nowak**, J. Suffczyński, P. Wojnar, A. Golnik, J. A. Gaj, and P. Kossacki. *Inter-dot coupling in a self-assembled quantum dot system*, Acta Phys. Pol., A **112**(2):321–324, 2007.

SUBMITTED PAPERS

- **S. H. Nowak**, F. Reinhardt, B. Beckhoff, J.-Cl. Dousse, and J. Szlachetko. *Geometrical optics modelling of grazing incidence x-ray fluorescence of nanoscaled objects*, J. Anal. At. Spectrom. Forthcoming 2012.
X-ray Standing Wave (XSW) is a well established formalism for modeling Grazing Incidence X-ray Fluorescence (GIXRF) experiments. However, when probing nanostructured surfaces with complex morphology the effects of the interaction of the XSW with structure elements need to be investigated. This is not always easy and sometimes even not possible. In the present work a novel approach employing Geometrical Optics (GO) calculations is proposed. The model is employed for simulations of two different types of nano-particle distributed on a flat surface. It is shown that GO optics simulation yields results with good agreement when compared to absolute measurements even when XSW deteriorates.

PAPERS IN PREPARATION

- F. Reinhardt, **S. H. Nowak**, B. Beckhoff, and J.-Cl. Dousse. *GIXRF vs. XSW vs. GO*.
Grazing incidence X-ray fluorescence spectra on periodic line structures were recorded for different tilt angles between the lines and the plane of incidence of the monochromatic synchrotron radiation. The results show features that can be easily understood and explained with calculations of the emerging X-ray standing wave field. On the other hand there are structures, i.e. pronounced modulations above the substrates critical angle of external total reflection, which are not included in the XSW concept. Novel geometrical optics calculations can reproduce these structures taking the samples specific geometric conditions into account.

